2003

Miniaturized analytical platforms from nanoparticle components: studies in the construction, characterization, and high-throughput usage of these novel architectures

Andrew David Pris
Iowa State University

NOTE TO USERS

Miniaturized analytical platforms from nanoparticle components: Studies in the construction, characterization, and high-throughput usage of these novel architectures

by

Andrew David Pris

A dissertation submitted to the graduate faculty

in partial fulfillment of the requirements for the degree of

DOCTOR OF PHILOSOPHY

Major: Analytical Chemistry (Chemical Instrumentation)

Program of Study Committee:
Marc D. Porter, Major Professor
R. S. Houk
Victor Shang-Yi Lin
L. Keith Woo
Scott Chumbley

Iowa State University

Ames, Iowa

2003

Graduate College
Iowa State University

This is to certify that the doctoral dissertation of

Andrew David Pris

has met the dissertation requirements of Iowa State University

Signature was redacted for privacy.

Major Professor

Signature was redacted for privacy.

For the Major Program

TABLE OF CONTENTS

ACKNOWLEDGEMENTS

"The most exciting phrase to hear in science, the one that heralds the most discoveries, is not "Eureka!", but "That's funny..."“
Isaac Asimov

"I have not failed. I've just found 10,000 ways that won't work."
Thomas Alva Edison

This thesis consists of four research chapters, in which the contributing individuals were recognized for their efforts. The purpose of this section is to acknowledge and thank those whose advice, encouragement, and support was given among the other 40,000 projects during my tenure in the Porter Research Group that did not result in an exclamation of either "Eureka!" or "That's funny...". First and foremost I would like to thank Dr. Marc Porter for his vast efforts to pursue, ensure, and understand interesting and meaningful research with the best-possible assemblage of facilities and people. I would like to think that I have acquired some of these positive attributes throughout this quest to becoming a quality research scientist.

I would also like to thank the numerous past and present members of the Porter Research Group with whom I have had the privilege to interact with. In particular, I would like to thank the following individuals for thier scientific insights, criticisms, and personalities: Janese O'Brien, Jeremy Kenseth, Hajime Takano, Michael Granger, Rachel Millen, (and in particular) Becky Staedtler, Daniel Gazda, and Jennifer Harnisch Granger.

Outside the laboratory, I have several people to thank for allowing me to become what I am today. I would like to thank my parents, Wayne and Georgia, for not only providing me with infinite opportunities, but also with a strange sense of humor that allows

one to enjoy the small things in life. I would also like to thank my extended family on both the Pris and the Olsen sides for always providing support in both tangible and intangible means.

In reverence to "saving the best till last", I must thank my best friend and wife, Suzy. Without her boundless good graces and support of listening to me when things were not exactly working, celebrating with me when they did work, keeping the shelves stocked, and patiently completing countless numbers of cross-stitches and books while waiting for me to arrive home, this excursion would have been far more difficult. Thank you Love.

This work was performed at the Microanalytical Instrumentation Center and Ames Laboratory under Contract No. W-7405-Eng-82 with the U.S. Department of Energy. Support was also provided through a Phillips Petroleum Corporation graduate research fellowship and the Mary K. and Velmer A. Fassel fellowship. The United States government has assigned the DOE Report number IS-T-1945 to this thesis.

GENERAL INTRODUCTION

Dissertation Organization

The scientific community has recently experienced an overall effort to reduce the physical size of many experimental components to the nanometer size range. This size is unique as the characteristics of this regime involve aspects of pure physics, biology, and chemistry. One extensively studied example of a nanometer sized experimental component, which acts as a junction between these three principle scientific theologies, is deoxyribonucleic acid (DNA) or ribonucleic acid (RNA). These biopolymers not only contain the biological genetic guide to code for the production of life-sustaining materials, but are also being probed by physicists as a means to create electrical circuits and furthermore as controllable architectural and sensor motifs in the chemical disciplines. Possibly the most common nano-sized component between these sciences are nanoparticles composed of a variety of materials. The cross discipline employment of nanoparticles is evident from the vast amount of literature that has been produced from each of the individual communities within the last decade. Along these cross-discipline lines, this dissertation examines the use of several different types of nanoparticles with a wide array of surface chemistries to understand their adsorption properties and to construct unique miniaturized analytical and immunoassay platforms.

This introduction will act as a literature review to provide key information regarding the synthesis and surface chemistries of several types of nanoparticles. This material will set the stage for a discussion of assembling ordered arrays of nanoparticles into functional platforms, architectures, and sensors. The introduction will also include a short explanation

of the atomic force microscope that is used throughout the thesis to characterize the nanoparticle-based structures. Following the Introduction, four research chapters are presented as separate manuscripts. Chapter 1 examines the self-assembly of polymeric nanoparticles exhibiting a variety of surface chemistries and attempts to deconvolute general adsorption rules for their assembly on various substrates. Chapter 2 extends the usage of self-assembly of polymeric nanoparticles through a layer-by-layer deposition concept and photolithography methodologies to create analytical platforms with a vertical height controlled within the nanometer regime. This platform is then furthered in Chapter 3 by employing this integrated concept as a bio-recognition platform, with the extension of the method to a high-throughput screening system explored. Chapter 4 exploits two different types of nanoparticles, silica and gold, as multiplexed, self-assembled immunoassay sensors. This final research chapter is followed by a general summation and future prospectus section that concludes the dissertation.

Literature Review

A wide range of fundamental concepts underlies the interplay between the stability of a nanoparticle dispersion and the composition/properties of the nanoparticles. This interplay must be understood in order to fully comprehend both the reasoning behind procedural protocols as well as the experimental results. To prepare the reader for these eventualities, this literature review examines the theoretical background for colloidal stability and then discusses the formation of three types of nanoparticles that find major usage within the scientific community: gold, silica, and organic polymers. With this knowledge, a brief discussion of nanoparticle assembly protocols in the scientific literature will commence. A

final portion of this review will describe the basics of the scanning probe microscope instrumentation that is utilized as a diagnostic tool in many of these studies.

Theorized stability mechanism for nanoparticle dispersions

The analytical utility of these unique materials, from diagnostics to "building block" motifs, is dependent upon the ability to maintain a fully suspended dispersion of nanoparticles that undergo Brownian motion until application of a stimulus. This stimulus is applied at a controlled point in time and will result in particle aggregation or flocculation. With this basic premise, guidelines must be established that predict the stability of the dispersion based upon the physical characteristics of the system, such as chemical groups on the particle surface and attributes of the dispersing solvent (e.g., ionic strength). These guidelines will assist in determining the type of chemical modifications that can be made to both the particle surfaces and the dispersing medium in order to exploit nanoparticles as an analytical tool. The seminal works and theories formed in predicting and describing colloidal stability based on the system characteristics were independently proposed primarily by two laboratories. Derjaguin and Landau first published this theory[1], which was then re-iterated by Verwey and Overbeek[2] due to lack of communication and journal accessibility during WWII. This theory, collectively known as the Derjaguin-Landau-Verwey-Overbeek or DLVO theory, has proven to be a relatively general, yet surprisingly accurate means of describing and predicting the factors dictating the attractive and repulsive interactions leading to colloidal stability. The success of this theory is based upon the combination of two established predictions of distance dependent forces: repulsive double-layer interactions and attractive van der Waals forces. It therefore is instructive to examine these interaction

theories in detail to form a solid foundation in which the observed results of stable particle formation mechanisms, particle surface chemistry manipulation, and solvent requirements can be understood to create dispersed, functional nanoparticles. As previously indicated, one of the primary interaction forces between individual colloidal particles is the electric double layer. However, it is beneficial to first provide a description of a double layer for an individual particle prior to discussing the interaction between the double layers of two particles.

Colloidal electrical double layer

It is well documented that the majority of stable colloidal dispersions are influenced by electric fields and the ionic strength of the dispersing medium, as dictated by the presence of charged groups on the colloid surface.[2] These charged groups can originate from functional groups being covalently grafted to the particle surface or through adsorption of charged inorganic or organic ions. The charge on the particle surface results in the local ordering of the electrolyte species near the particle surface. This ordered layer is referred to as the diffuse electric double layer.[3] A full examination of double layers within various media (no electrolyte, counter-ion only) will be left to the reader. The much more commonly encountered experimental condition in which charged particles interact in media containing electrolyte ions will be considered here. As a starting point, the Grahme equation is presented (1). The Grahme equation relates the surface charge density on the colloidal surface (σ) to the colloid surface potential (ψ_o) and the electrolyte concentration[4]

$$\sigma^2 = 2\varepsilon\varepsilon_o kT\left(\sum_i \rho_{oi} - \sum_i \rho_{\infty i}\right) \tag{1}$$

where ε is the dielectric constant of the dispersion medium, ε_o is the permittivity of free space, k is Boltzmann's constant, T is absolute temperature, $\rho_{\infty i}$ is the bulk concentration of ion i of valency z, and ρ_{oi} is the surface concentration of ion i of valency z. The latter parameter can also be recast as (2):

$$\rho_{oi} = \rho_{\infty i} \exp^{(-z_i e\psi_o)/kT} \tag{2}$$

where e is the charge of an electron and the colloid surface potential (ψ_o). It is important to note that ψ_o, and therefore ρ_{oi}, are dependent upon other solution variables, such as pH, that could result in the loss or formation of charged surface functional groups. At low potentials (i.e. ψ_o less than 25 mV), the Grahme equation (1) simplifies to (3)[4]

$$\sigma = \varepsilon\varepsilon_o \kappa\psi_o \tag{3}$$

where ψ_o becomes directly proportional to σ and κ is defined as (4).[4]

$$\kappa = \left(\sum_i \rho_{\infty i} e^2 z_i^2 / \varepsilon\varepsilon_o kT\right)^{\frac{1}{2}} \tag{4}$$

The inverse of κ is more commonly referred to as the Debye length and is a measure of the thickness of the double layer. In this instance, however, κ^{-1} represents the distance at which the order of the solvent is affected by the presence of the colloid. Importantly, this thickness is independent from any surface properties of the colloid and therefore is entirely determined

by the solution composition/characteristics, such as the dielectric constant of the solvent and the electrolyte concentration and charge.

The effect of this charged body on the electrolyte is not constant over the entire Debye length. Since these interactions are electrostatic in nature, it is inherent that a higher electrolyte concentration would reside closer to the surface of the charged body. With increasing distance from the charged body, the influence of electrostatics would decrease, as thermal motion becomes an increasingly important factor. Thus, a gradient of electrolyte concentration within the double layer extending from the charged body must be considered in addition to the maximum separation distance in which two neighboring charged bodies would experience interactions.

The mathematical description of this gradient was proposed independently by Gouy and Chapman, and is known as the Gouy-Chapman theorem.[3] The approach taken begins with the observation that the total electrostatic charge on the colloid surface is a function of $\rho_{\infty i}$, ψ_o, and the thermal movement of electrolyte, and is rooted in the established variation of ρ_x as a function of ψ_o and distance from the surface (x) as described in the Poisson-Boltzmann equation. Upon further mathematical manipulation (see Bard et al. [3]), the potential as a function of distance (ψ_x) can be written as (5):[4]

$$\psi_x \cong \frac{4kT}{e}\gamma \exp^{-\kappa x} \tag{5}$$

where the non-descript variable γ, as introduced for simplification, is defined as (6).

$$\gamma = \tanh\left(ze\psi_o / 4kT\right) \tag{6}$$

With the establishment of the length and gradient over which the double layer of a charged surface affects the surrounding environment, it is now possible to discuss the interaction of the double layers of two identically charged planar bodies as a function of separation distance.

As these two planar bodies and their associated double layers being to interact, an excess osmotic pressure (P) for the ions in the two double layers begins to form at the mid-point between the two planes. With the ability to determine the concentration of ions as a function of distance from the charged surface via the Gouy-Chapman theorem, the excess osmotic pressure of the interacting ions over those in the bulk can be written as (7).[4]

$$P = 64kT\rho_{\infty}\gamma^{2}\exp^{\kappa\alpha} \tag{7}$$

This increased pressure between the interacting charged planes can be extended to describe the interfacial pressure of two interacting sphere through the Derjaguin approximation[5] with the assumption that the range of interaction and separation is less than the sum of radii of the two spheres. This pressure can be further converted into a repulsive force between two spheres of radius R and charge σ and is depicted as (8).[4]

$$F = \frac{2\pi R\sigma^{2}\exp^{-\kappa\alpha}}{\kappa\varepsilon\varepsilon_{o}} \tag{8}$$

As these surfaces are identical in charge, the force will always be positive indicating a repulsion between the two bodies. The magnitude of this repulsive force between identical nanoparticles within a colloidal dispersion represents one factor in determining the stability of the dispersion and the ability of the nanoparticles to be maintained as individual entities.

van der Waals interactions

With the formation of a repulsive force between interacting charged colloids, the second part of the DLVO theory describes the attractive interactions between dispersed particles. There are several intermolecular forces (e.g., coulombic, electromagnetic, van der Waals interactions) that could contribute to the attractive forces between colloidal particles. However, based upon the experimentally observed stability of dispersions upon altering the coulombic and electromagnetic interactions, the universally attractive force in colloidal dispersions is usually attributed to van der Waals interactions. This accounts for the independence of the attractive forces from characteristic properties of the molecule as well as the insensitivity toward solution composition (i.e., pH, electrolyte).

van der Waals forces are composed of three collective intermolecular factors: polarization (permanent dipole- permanent dipole); induction (permanent dipole-induced dipole), and dispersion (London forces).[6] It is this third quantum mechanical contribution that has been experimentally shown to dominate in most circumstances. Dispersion forces are, on the simplest level, analogous to an instantaneous and cooperative dipole-induced dipole interaction between atoms. Its origins, however, lie within the associated movements of electrons around an atom producing an instantaneous dipole moment. This temporary dipole moment creates an electromagnetic field that induces a dipole within neighboring atoms. Likewise the fluctuating dipole within the second atom induces an instantaneous dipole within the first atom. This combined instantaneous induced dipole produces a finite, yet short-lived, attractive force between the atoms.[4,6]

To extend the analysis of the attractive van der Waals interaction between atoms to that between macroscopic bodies, the following assumptions are made:[7,8] the interactions are non-retarded; the interactions are additive across a vacuum; and the interactions can be modeled as an attractive pair potential ($U(r)$) between two atoms according to London's theory[6] as represented by (9)

$$U(r) = -C/r^6 \tag{9}$$

where C is the London co-efficient for atom-atom pair potential and r is the distance between the two bodies. These assumptions greatly simplify the treatment of the system, however, a detailed examination of the validity of the assumptions should be explored.

The non-retarded assumption addresses the distance dependent decay of these interactions and is of consequence when the time for the electromagnetic field to traverse from one atom to another atom and then return is larger than the oscillation period of the electrons movement around the first atom. That is, the greater the travel time, the more likely the electromagnetic field returning to the first atom will have changed with respect to when the electromagnetic wave was created. As a consequence, the new dipole orientation leads to a decrease in the strength of the interaction between the two atoms.[2,4]

The next assumption, additivity, permits for the extension of this atom:atom interaction to multi-atom bodies by summing the van der Waals interaction energies of all the atoms in one solid with all of the atoms in a second solid. This additivity assumption more specifically allows for the integration of the van der Waals interactions over the volumes of the objects. van der Waals interaction energies are therefore geometry dependent. To account for this geometric dependence, mathematical expressions of the interaction energy

include a variable known as the Hamaker constant. The Hamaker constant is proportional to the energetic van der Waals interactions between two bodies, while the rest of the equation represents the correction for the system geometry. An example of these geometric dependent van der Waals interactions between two spheres of radius R_1 and R_2, separated by distance D is shown in (10), where again the van der Waals interaction potential is represented by the Hamaker constant (A, in Joules) and the rest of the expression corrects for the geometry of the system:

$$U_{sphere:sphere} = \frac{-AR_1R_2}{6D(R_1 + R_2)} \tag{10}$$

The Hamaker constant itself is then derived, with the above assumptions, from the Hamaker summation method[7,8] and can be represented as (11):

$$A = \pi^2 C \rho_1 \rho_2 \tag{11}$$

where ρ is the number density of the atoms in each solid and the London coefficient (C) for atom-atom pair potential is given as[9] (12):

$$C = \frac{3\alpha^2 \hbar\omega}{4(4\pi\varepsilon_o)^2} \tag{12}$$

where α is the static polarizability of the atoms, and $\hbar\omega$ is the ground state oscillation energy of electrons.

Although the Hamaker summation method provides a relatively effective means to calculate A and the associated attractive pair potential energy between two bodies of various geometries, it does have its limitations. The primary constraint results from the failure of the

additivity assumption due to ignoring the effects of neighboring atoms and their instantaneous dipoles when calculating the dispersion pair potential between two atoms in different bodies.[4] Furthermore, the additivity assumption does not account for effects of the intervening medium that is separating the two bodies.[4] To address these weaknesses, the Lifshitz theory for predicting the Hamaker constant was developed.[10,11]

The Lifshitz theory avoids the assumption of additivity, and its fore mentioned flaws, by utilizing quantum field theory and treating the interacting bodies as continuous media.[4] This results in the ability to calculate the Hamaker constant in Joules through measurable bulk properties of the interacting bodies 1 and 2 separated by medium 3 (13).

$$A=\left(\frac{3kT}{4}\right)\left(\frac{\varepsilon_1-\varepsilon_3}{\varepsilon_1+\varepsilon_3}\right)\left(\frac{\varepsilon_2-\varepsilon_3}{\varepsilon_2+\varepsilon_3}\right)+\left(\frac{3\hbar\omega}{8\sqrt{2}}\right)\left(\frac{\left(\eta_1^2-\eta_3^2\right)\left(\eta_2^2-\eta_3^2\right)}{\left(\eta_1^2+\eta_3^2\right)^{1/2}\left(\eta_2^2+\eta_3^2\right)^{1/2}\left[\left(\eta_1^2+\eta_3^2\right)^{1/2}+\left(\eta_2^2+\eta_3^2\right)^{1/2}\right]}\right) \quad (13)$$

Here ε is the dielectric constant and η is the refractive index of the denoted bodies and medium. Since the Lifshitz theory provides a more accurate means of determining the Hamaker constant (A), the geometry corrections present within the pair potential equations (10) can then be applied to determine the interaction energies.

DLVO theory

With the establishment of both the repulsive double layer and the attractive van der Waals interactions, these concepts are then combined in order to define the pair potential between two interacting charged bodies, thus forming the DLVO theory. The DLVO theory is not a simple summation of these two forces, but rather a prediction of the degree to which one force will dominate over the other as a function of sample conditions (i.e., ionic strength, identity of dispersing medium, dielectric constant of the bodies, ect.) and separation

distances. In determining the magnitude and direction (i.e., repulsive or attractive) of the interaction potential, general conclusions should be drawn from the above discussion.[4] One such conclusion is that the above equations depict the independence of the distance dependent attractive van der Waals interaction potentials from the surface chemistry of the colloid and the characteristics of the solvation medium (e.g., pH, electrolyte concentration). On the other hand, the repulsive double layer interaction potentials vary strongly as a function of colloidal surface chemistry and electrolyte concentration in the dispersion medium. Furthermore, at short separation distances, the gradient of the attractive van der Waals interactions as a function of distance is greater than that for the repulsive double layer due to the power-law dependence of van der Waals interactions. The culmination of these factors argues that colloids will aggregate due to van der Waals interactions if the repulsive double layer interactions allow the separation of the colloids to become too small. This general statement is consistent with several colloidal stability observations[4] such as the correlation that colloids with high surface charge, and a corresponding thick repulsive double layer, will remain as a stable dispersion. This is closely related to the experimentally noted nanoparticle aggregation upon reduction of colloidal surface charge either through depletion of surface functionalities or charged-body screening. One other observation is the existence of a secondary interaction energy minimum at larger separation distances in more concentrated electrolyte suspensions. The depth of this energy well decreases as colloidal diameter increases, leading to the ability of larger colloids to undergo reversible aggregation, whereas smaller colloids, with a larger secondary energy minimum, cannot be re-suspended.

The accuracy of this theory in describing the effects of electrolytes, material constants, surface charge densities, and size of colloid upon colloidal stability is remarkable.

When this theory does fail to predict stability, it is usually attributed to the existence of other forces not considered within the DLVO theory such as hydration, steric, or osmotic forces.[4] The hydration, or solvation, force refers to how water layers must be ejected from the surface as two solvated bodies move toward each other. This results in an additional repulsive force that prevents aggregation at distances where DLVO predict aggregation. Another repulsive force leading to stability is the steric force present from the unfavorable energetics of the compression of bulky, segmented surface groups upon colloidal interaction.[12] A third additional force is present when either of the two interacting bodies is permeable to water. This results in an attractive deviation to DLVO as water flows into the body from the space between the two bodies. Lastly, perhaps the largest repulsive deviation from DLVO is as a result of the adsorption of ionic species on the charged body, creating a Stern layer within the electrical double layer which modulates the interaction distances between two bodies. With the completion of this overview, it is now possible to discuss the formation mechanisms and procedures to create and modify stable colloidal particles.

Nanoparticle preparation pathways

A critical property of synthesized nanoparticles, which is of absolute necessity for many analytical applications, is particle monodispersity. Monodispersity refers to extremely small, or ideally no, variations of size, shape, and morphology in the particle population (i.e., particle diameter of 15 ± 1 nm). Monodispersity is required as many of the chemical and physical properties, such as reactive surface area, plasmon resonance, and stability of the particles, are dependent upon their size and shape. In reference to this dissertation, monodispersity is vital. In Chapter 1, the size of the particles does have a significant effect

on the adsorption properties through the magnitude and type of charge on the particle surface or the modification thereof by sorbed surfactants. The work in Chapters 2 and 3 requires intimate knowledge of the "building block" dimensions in order to calculate the number of layers of nanoparticles in the fabricated structure, whereas the identification of a target analyte is entirely dependent upon the size of a particle in the research detailed in Chapter 4. All of these experiments are heavily dependent upon the physical (i.e., size, shape, and density) and chemical homogeneity of the particles. Therefore prior to studying the synthetic and mechanistic specifics for the production of gold, silica and polymeric nanoparticles, it is valuable to examine possible growth mechanisms that will result in the formation of monodisperse colloidal particles. There have been two general mechanisms proposed from within the colloidal sciences that would possibly lead to the formation of monodisperse particles. The first is known as LaMer or monomer-addition growth mechanism, and the second is referred to as aggregative growth mechanism.

Monomer-addition, or LaMer, growth model

The LaMer theory of monodisperse particle growth,[13] and those based upon it, begins with the assumption that the process is initiated with an induction period. During this time, the nanoparticle molecular or atomic building components (referred to hereafter as monomers) are produced and reach a critical concentration. Once this critical concentration is reached in the reaction medium, it is statistically possible for two "monomers" to come into contact with one another and undergo a system dependent reaction. This reaction binds the monomers into an embryonic core, or nucleus, that will grow into a particle. This nucleation event, referred to as a nucleation burst, is assumed to occur very quickly, forming

nuclei at a very high rate. The nucleation burst results in the rapid drop in the monomer concentration to below the critical level, and the cessation of nuclei formation. The final particle number is therefore dependent upon the number of nuclei formed during this short, one time nucleation period. The growth of these nuclei into particles continues through the diffusion of the monomers through the reaction matrix to the nucleus/particle surface where they are incorporated into the growing body. This diffusion-limited, growth process is required to occur at a rate that is greater than that of monomer formation and continues throughout the reaction until the monomer is completely consumed. This continued consumption of the monomer species prevents the monomer concentration from reaching the nucleation critical concentration, limiting the formation of more nuclei. This one time nucleation event coupled with the steady rate of particle growth and the homogeneity of the reactants in the system, results in each particle completing growth at the same time, thus forming a monodisperse dispersion. This monodisperse growth mechanism, although effective in some cases in predicting particle size, has been found both experimentally and theoretically to be unrealistic for all particle synthetic protocols.

In many other nanoparticle synthetic routes, it was found that although growth of the nuclei proceeded at a steady rate, several other factors needed for LaMer growth were not achieved.[14-16] Some examples of these deviations include: diffusion of the monomers calculated to be lower than the observed particle growth rate; continuous nucleation throughout the growth process; inability of the DLVO theory to predict colloidal stability of the small, relatively weakly charged nuclei. To account for these shortcomings, a second general growth mechanism was formulated and is referred to as the aggregative growth mechanism.

Aggregative growth model

Although more complex, this model accounts for many more physical variables and experimental observations then the LaMer model. As originally proposed by Bogush and Zukoski,[14-16] the aggregative growth mechanism also initiates through the formation of monomer groups. The monomers then cross-react, producing a growing oligomer species. Unlike the LaMer model, however, there is no induction period for nuclei formation, but rather nucleation proceeds continuously throughout the process. Following the work of Klemperer et al.,[17] a Flory–Stockmayer type growth is mimicked in which once the oligomer reaches a certain size, it can no longer be solvated by the reaction medium, and thus the oligomer collapses and undergoes phase separation to form a "primary" particle.[18,19] The ability of small primary particles to remain dispersed in the solution, which is not considered in the monomer growth model, is then dictated by particle interaction potentials as described by DLVO theory.

The DLVO theory predicts, through numerical calculations, that the interaction potential for particles encountering one another due to Brownian motion is greater between a small particle and a large particle than the interaction potential between either two large particles or two small particles. This calculated situation holds true until the larger particle reaches a system dependent upper size limit, in which the interaction potential of the larger particle with particles of any size is severely diminished.[15,20] Accordingly, this theoretically assessed situation envisions that the small, as produced, primary particles are not stable as singular entities. The aggregative model therefore predicts growth through the scavenging of smaller particles by larger particles. Thus, the larger particles grow through the aggregation

of smaller particles on their surfaces. As the particle reaches the system imposed upper size limit, the aggregation is drastically curtailed and particle growth through aggregation slows dramatically.[16] This DLVO predicted upper size limit for aggregation also contributes an explanation for monodispersity within the aggregative growth mechanism.[16] It should be noted that the aggregative growth model does not prohibit monomer growth on formed particles; however, aggregation of particles is the major growth route.

Hybrid-growth models

Although providing for a growth model with fewer aspects, the majority of theorized growth mechanisms are not constructed from either a pure monomer-addition or aggregative growth model. Rather, the mechanisms are formulated by combining differing features of the two general mechanisms. The ability to construct an individual growth mechanism from varying portions of the two general mechanisms provides the needed flexibility to describe observations made during nanoparticle synthesis. Due to this enhanced freedom, several different growth mechanisms for the same nanoparticle production process can be postulated. Therefore, following are the descriptions of postulated nanoparticle growth mechanisms in which multiple mechanisms are proposed for each material of interest (i.e., gold, silica, and organic polymer).

Formation of gold nanoparticle dispersions

The sanguine dispersions of gold nanoparticles have historically been used, unwittingly in many cases, for a wide array of purposes ranging from medicinal (e.g., arthritis therapy) to decorative (e.g., ruby glass). Only relatively recently have gold

nanoparticles been specifically sought and used within the scientific laboratory.[21] Faraday's work with gold nanoparticle dispersions in 1857 marks the first scientifically documented investigation into the formation and properties of gold nanoparticle dispersions.[22] Since that time, gold nanoparticles have found use in a variety of applications, including biological staining/labels,[21] nanoelectronic components,[23] and electrochemistry.[24] This situation again emphasizes the union of several classically differentiated scientific fields (i.e., biology, physics, and chemistry) by the nanometer regime. Due to this long history, a multitude of gold nanoparticle synthetic procedures have been published. Examples include those involving laser ablation,[25,26] ultraviolet irradiation,[27,28] electrochemical deposition,[29] ultrasonic irradiation,[30] lithography and etching,[31] and gas phase synthesis.[32,33] By far the most common means to produce gold nanoparticles, as well as other noble metal nanoparticles such as Ag, Pt, and Pd, is through the solution phase reduction of metal salts, particularly tetrachloroauric acid.[21,34] Although the majority of gold nanoparticle synthetic techniques utilize scrupulously clean glassware and tetrachloroaurate, there exists a plethora of different reducing agents and other stabilization components employed within these available techniques. All of these differing procedures create varied sizes of gold nanoparticles with an array of dispersities, morphologies, and stabilities. These results indicate that although the chemical reaction of the systems are similar (reduction of Au(III) to Au(0) by the reducing agent), the differing reducing agents and solution additives reach their synthetic goal through different nucleation and growth mechanisms.[35]

A general trend has been established with the production of smaller particles through the usage of stronger reducing agents.[21] Examples of reducing agents for the reduction of tetrachloroauric acid in the production of gold nanoparticles include alkaline

tetrakis(hydroxymethyl)phosphonium chloride, white phosphorous, thioisocyanate, sodium borohydride, ethyl alcohol, thiols, aminoboranes, hydrazine, formaldehyde, hydroxylamine, oxalic acid, sugars, hydrogen peroxide, sulfites, carbon monoxide, hydrogen, acetylene and ascorbic acid.[36,37,34] As a consequence, a surprisingly limited amount of research into the elucidation of the gold nanoparticle growth mechanism has been performed.[38] However, with many options available for reducing agents, sodium citrate has by far been the most utilized of the reducing agents.[34]

Sodium citrate as the reducing agent. The dominance in the use of sodium citrate can be attributed to early studies by Turkevich and co-workers on the effects of reducing agent composition and concentration on the nanoparticle size and dispersity.[39] In this study, citrate was shown to be the most versatile in creating stable, monodisperse gold nanoparticles. The dominance of citrate as a reducing agent was further advanced by Frens,[40] who applied Turkevich's work in studies that examined the effect of citrate concentration on the final size of the gold nanoparticle, with the hypothesis that the lower concentrations of citrate would lead to a lowered amount of nucleation and the larger particles would be produced as predicted by the LaMer growth model. This work furthered the employment of citrate as a means to obtain stable, monodisperse solutions of gold nanoparticles with controllable sizes. Due to the extreme extent of usage, a growth mechanism for gold nanoparticles produced with citrate has been proposed. Prior to examining this proposed growth mechanism, it is valuable to consider the general synthetic protocol as well as some of the experimental observations from which the growth mechanism is based.

In the Frens method, an aqueous solution of approximately 0.1% (w/w) tetrachloroauric acid is stirred vigorously and heated to the desired temperature. Another aqueous solution, which is about 1/10 the volume of the first solution and composed of about 1% (w/w) sodium citrate, is then added. The resulting solution is allowed to react for the desired amount of time, which can vary from 5 seconds to 15 minutes.[34,38,40] Upon mixing, the solution turns faint blue and then a sanguine red. Again, by altering the constituent amounts as well as the reaction temperature, the final particle size can be manipulated.

The mechanism involved in the Frens-type citrate reduction has been investigated by Zukoski and co-workers.[38] The proposed mechanism is based upon the observation (i.e., transmission electron microscopy (TEM), dynamic light scattering, and absorption spectroscopies) that the particles at the beginning of the reaction, as marked by the faint blue colored solution, were of two sizes and morphologies: smaller, dense, spherical particles and larger, "fluffier" particles with random morphologies and heterogeneous densities (i.e., dense cores surrounded by a less dense matrix).[38] As the reaction continues, the smaller dense particles were found to grow in size and increase in numbers, while the larger, less dense particles are reduced in size and number. To describe this, Zukoski and workers utilized a combination of the LaMer and aggregative growth models.

The mechanism presented by Zukoski,[38] begins with a LaMer type nucleation (i.e., induction and burst nucleation) producing the gold nuclei. These nuclei then form intermediary, primary particles (as described above as dual-sized, inhomogeneous particles) through a proposed reversible aggregative process. The formation of either the intermediary particles or the final gold nanoparticle is dependent upon the source of the electrostatic charge on the gold nuclei (i.e., the adsorbed anion of tetrachloroaurate or citrate). In support

of this perspective, they found that the tetrachloroaurate and citrate compete for adsorption sites on the gold nuclei.[41] However, tetrachloroaurate exhibits a greater adsorption affinity for the gold surface, thus represents the source of stabilizing charge at the early stages of gold nanoparticle growth.[41] Zukoski and workers argue that the tetrachloroaurate anion does not supply enough charge to ensure a stable dispersion of individual nuclei resulting in the loose aggregation of the nanoparticles and presence of larger, inhomogeneous intermediary particles and corresponding blue color of the initial dispersion.[38] With the continued progression of the reaction, the concentration of tetrachloroaurate anions is lowered through the sustained reduction by citrate. Citrate, with its charge of -3 as opposed to the -1 charge of tetrachloroaurate, then begins to dominate the occupancy of the adsorption sites on the particle surface. The gold nanoparticles now posses a higher surface charge and are stable as individual entities, thus the intermediary particles de-aggregate into individual, dense spherical particles. They summarize this mechanism as a LaMer growth model that allows the particles to reversibly aggregate upon the desorption/consumption of tetrachloroaurate and adsorption of the higher charged citrate.[38]

Iso-ascorbic acid as the reducing agent. As mentioned above, the mechanism put forth by Zukoski and co-workers is not universally applicable to all gold nanoparticle synthetic techniques. Matijevic and co-workers have predicted that nanoparticles produced through the reduction of tetrachloroauric acid by iso-ascorbic acid follows a different mechanistic route.[35,36] With iso-ascorbic acid, Matijevic and co-workers propose a LaMer type induction and burst nucleation coupled to a growth stage whose mechanism is dependent upon the other experimental conditions such as pH. The importance of these

system conditions upon determining the type of growth stage are linked to the earlier discussion of DLVO particle interaction potentials and the relationship between system conditions (i.e., pH , ionic strength) particle stability. Therefore, the primary particles in this proposed theory grow via an irreversible aggregation if particle stability is low or form larger particles though monomeric reaction pathway if the particle interaction potential is sufficiently repulsive. The important point, however, is that the resulting distribution in particle size and morphology is dependent upon the type of growth mechanism that is allowed to proceed in the system as dictated by both the solution conditions as well as the reducing agent.

Sodium borohydride as the reducing agent. One reason for the extensive versatility of citrate as the reducing agent is its ability to act as a source of electrostatic charge for particle stabilization. That is, stable dispersions can be prepared without the addition of other stabilizers (i.e., charged molecules, polymer chains) to the reaction mixture. However, to prepare smaller particles, stronger reducing agents must be used that may not play the dual role of reducing agent and stabilizer. An example of this is the usage of sodium borohydride, which could adsorb to the particle surface and provide charge stabilization. However, its gradual consumption by water would diminish this capability.[42,43] Although there exist several protocols that employ stronger reducing agents with a variety of stabilizers (i.e., poly(vinypyrolidone)[44]), one of the more utilized means in analytical chemistry to form very small gold particles (so small that they have been referred to as atomic clusters[45]) is based upon the reports of Brust and co-workers. In this work, the strong reducing agent sodium borohydride is used along with thiol stabilizers.[23,46,47]

Although the product also depends upon the reaction conditions and components,[45] the Brust procedure generally involves a two-phase system with a phase transfer reagent. This synthesis begins with a stirred solution of toluene and water in which the transfer reagent (e.g., tetraoctylammonium bromide) and tetrachloroauric acid have been added in amounts to form the desired particle size. Upon transfer of the tetrachloroauric acid to the organic phase, as marked by decoloration of the aqueous phase and subsequent development of color in the organic phase, the organic phase is isolated and the appropriate amount of stabilizing thiol is added (e.g., dodecane thiol). The solution is brought to the desired reaction temperature and an aqueous sodium borohydride solution is titrated into the vigorously stirred solution at a controlled rate that again is chosen to yield a target particle size. This solution is stirred for about 3 h, and the product is then isolated through rotary evaporation and suspended in ethanol. Depending upon reaction conditions, particles ranging from 1 to 5 nm can be readily prepared.[23,45] Furthermore, it is speculated that heating the particles in an organic solution that contains the thiol stabilizer, or even in neat solutions of the thiol, controllably etches the outer surface of the gold nanoparticle.[48,49] This step provides an additional pathway that can be used to create smaller, more monodisperse particles when necessary.[48,49]

Formation of silica nanoparticle dispersions

The multitude of procedures and mechanisms for the formation of silica nanoparticles, as well as their breadth of uses, represents another intersection of several scientific fields. Silica nanoparticles of various sizes, conformations, and surface functionalities have been fabricated through careful manipulation of the chosen preparative

method (i.e., flame hydrolysis, reverse oil-in-water microemulsions, and acid-catalysis).[50] The most employed means to produce uniform silica nanoparticles, however, is the Stöber method, which is based upon earlier observations by Kolbe.[51,52]

Stöber synthesis. This classic process involves the base-catalyzed hydrolysis and condensation of silicon alkoxides in solvents consisting of low molecular weight alcohols and small quantities of water.[51] The most commonly used chemical components are tetraethylorthosilicate (TEOS) as the silicon source, ethanol as the solvent, and ammonia as the base. These components interact via a reaction scheme that involves the base-catalyzed hydrolysis and condensation of the silicon precursor. The hydrolysis reaction is initiated by the formation of a hydroxyl moiety through the de-protonation of water by ammonia. This hydroxyl group in turn acts as a nucleophile and attacks the silicon atom in a traditional S_N2 reaction process, displacing one of the ethoxy groups and forming a silanol group. The extent, rate, and location of the hydrolysis of the remaining ethoxy groups will be discussed in further detail below as experimental findings have shown that only a singly hydrolyzed TEOS molecule acts as the active reagent.[53]

The reaction scheme continues with a condensation process that begins with the base-catalyzed de-protonation of the newly formed silanol group. This de-protonated group then acts as a nucleophile in another S_N2 reaction with either a silanol or ethoxysilane group, producing a siloxane linkage as well as either water or ethanol, respectively. Other side reactions that may form trace products include re-esterification, reversal of hydrolysis, and ester exchange.[54] Importantly, the Stöber synthesis yields spherical, extremely monodisperse particles over a size range extending from ~50 nanometers to several micrometers. Possibly

the most intriguing attribute of this process is that the rate of silica particle formation and final size are dictated, and therefore easily adjusted, by the stoichiometric quantities of the reaction constituents.

In an effort to harness the full abilities of this method, many research groups have endeavored to deconvolute the particle growth mechanism involved in the Stöber process. These investigations have not, however, led to a consensus, resulting in a rich medley of proposed mechanisms. Moreover, almost all of the proposed mechanisms involve different aspects from the monomer-addition or aggregative growth theories.[55]

Silica nanoparticle growth mechanism by monomer-addition. The monomer-addition model for silica nanoparticle production was pioneered by Matsoukas and Gulari[56-58] and closely mimics the LaMer model.[13] Matsoukas and Gulari utilized experiments based upon light scattering and Raman spectroscopy to argue that the Stöber process begins with the hydrolysis of the ethoxy group of TEOS as the rate-limiting step.[54] This model begins with an induction period in which no particles are formed as the concentration of the hydrolyzed TEOS increases to a critical level. At this point, the typical LaMer burst nucleation occurs with the condensation reaction between two monomers occurring at a rate that is faster than the production of monomer through the hydrolysis of TEOS ethoxy groups.[54] After nucleation the particles grow through the slow monomer production step (via hydrolysis) and the more rapid reaction with the particle surface (via condensation). Matsoukas and Gulari argue that the monodispersity of the silica particles is accounted for by a self-sharpening mechanism innately incorporated into this growth model, with the rate of particle growth dependent upon particle size (e.g., smaller particles grow faster than larger

particles).[58] Key points to note about this model are: 1) the rate limiting step is the formation of monomers through the hydrolysis of the TEOS; 2) nuclei are formed during a single, brief period prior to particle growth; and 3) the rate of growth dependence on particle size represents a self-sharpening mechanism.

Aggregative-based silica nanoparticle growth mechanism. Contrasting this basic mechanism of Stöber particle formation and growth is the aggregative growth mechanism proposed by Bogush and Zukoshi.[14,15] These authors, through the interpretation of the same and new experimental data, found several inhibitory weaknesses in the monomer growth model, which resulted in their creation of an aggregative growth mechanism. Bogush et al., begin their growth mechanism with the hydrolysis of the TEOS ethoxy groups forming a monomer. This monomer reacts through condensation with other monomers, resulting in a growing oligomer species that eventually undergoes phase separation forming the primary particle.[18,19] As detailed earlier in the general discussion of aggregative growth model, the primary particles then undergo size dependent aggregation. Recall that interaction potential between a large particle and a small particle is greater than the interaction potential between two large particles or two small particles. Thus, the silica nanoparticles grow through scavenging the continuingly nucleating primary particles and aggregating them on their surface. The larger particles continue growth through this aggregation until reaching the system defined upper size limit, yielding a single sized particle.[16] A small amount of growth is attributed to monomer-addition; however, the majority of nanoparticle growth is through aggregation.

Utilizing the aggregative growth model, Bogush et al. successfully modeled several observations related to silica nanoparticle growth. As mentioned above, the aggregative growth model not only explains the particle monodispersity of the Stöber reaction, but also accounts for the dependence of the final particle size on ionic strength (i.e., interaction potentials are greatly affected by the overall ionic strength). Moreover the aggregative growth model allows for particle nucleation and particle growth to occur in parallel, as well as for the rate of particle growth to occur at a level higher than that predicted solely by monomer diffusion.

Since particle growth rate is no longer dependent upon monomer formation kinetics as it is in the monomer growth model, the overall rate-determining step within this model is claimed to be the formation of the primary particles that nucleate through the reaction. Although Bogush et al. recognize that the rate of particle growth equals the rate of hydrolysis, they argue that the hydrolysis is not the rate-limiting step because the reversibility of the hydrolysis and condensation reaction mechanism need to be considered.[15] The reversibility of the hydrolysis and condensation reactions can result in a "psuedo-steady state" concentration of hydrolyzed monomer if a slow reaction is present later in the growth mechanism. They propose that this rate-determining step is the formation of the primary particle, as stated above.

Hybrid silica nanoparticle growth mechanisms. As a result of the inconclusiveness of the two extreme growth mechanistic explanations for silica nanoparticles, the most recently proposed growth models typically advance a mixture of both monomer and aggregative growth. Harris and co-workers have proposed the following

growth scheme that closely mimics the monomer-addition model. It is couched on the lack of experimental data to support the existence of the primary particles proposed in the aggregative growth model.[59-63] In support of the Harris growth scheme, small-angle X-ray scattering (SAXS) and nuclear magnetic resonance (NMR) techniques revealed that the growth process begins with the overall rate-determining hydrolysis of TEOS molecules that continues until a critical concentration is amassed. The NMR results indicate that in Stöber systems with low concentrations of water, only a single ethoxy unit of TEOS is hydrolyzed forming the active monomer.[53] These singly hydrolyzed monomers, when present above a critical concentration, undergo a brief nucleation period through condensation to form the primary particle. Again, this nucleation period is brief and continues only until the monomer concentration falls beneath the critical concentration. The nuclei that are formed within the Harris model, as confirmed by scattering data, are described as mass-fractals. These mass-fractals contain un-hydrolyzed ethoxy groups within their interior resulting in nuclei that possess a low density. The particle growth of these mass-fractals continues through the slow hydrolysis and condensation of interior ethoxy groups. This process results in a densification of the particle and the movement of active reaction sites to the particle surface. At this point, the particle is referred to as a surface-fractal. Growth continues through the hydrolysis of surface bound ethoxy groups that then undergo condensation with the singly hydrolyzed monomers present within the reaction system. This growth and smoothing of the surface-fractal is reminiscent of the monomer addition model.

The Harris model is successful in describing several observable results, including the incorporation of slowly hydrolyzing organosilane molecules into the particle interior as a consequence of reactive, unhydrolyzed ethoxy groups in the interstitial region of the mass-

fractal.[54,64] This model also accounts for smooth nature of the end product. It fails, however, to accurately depict the magnitude of continued nucleation throughout the Stöber synthesis as expressed in the experimental evidence of Bogush et al. In response, Harris and co-workers adjusted the model to allow later nucleating particles to aggregate upon the particle surface.[59]

Another modern growth mechanism that instead reflects the influence of the aggregative growth model was put forth by van Blaaderen and co-workers[54,55,63,65] and is paralleled by the work of Vacassy et al.[64] Again, the process begins with the overall rate-determining hydrolysis of a single TEOS ethoxy group. In agreement with Harris and co-workers, the reactive monomer species is a singly hydrolyzed TEOS molecule.[53,65] The other ethoxy groups are eventually hydrolyzed and undergo condensation reactions, but at a later time as evidenced by the incorporation of slower hydrolyzing organosilane molecules into the interior of the silica particle. van Blaaderen defends the assignment of the system rate-limiting step to the hydrolysis of the first ethoxy group of TEOS by utilizing ^{13}C NMR data that indicate the hydrolysis and condensation back reactions and esterification do not occur to a significant extent. This conclusion casts doubt on Bogush and co-workers aggregative model identification of primary particle formation representing the rate-limiting step.[55,65]

After monomer formation, particle nucleation in the van Blaaderen model is appointed to oligomer aggregation, similar to the aggregative theory. van Blaaderen does, however, disagree with the extent of aggregation, arguing that it only occurs for a brief interval near the beginning of the reaction. This time period depends upon the system constituents, which dictate when the nuclei will be stable as a consequence of their

interaction potentials. Once nuclei achieve stability, growth proceeds through the addition of small oligomers and monomers to the particle surface until the monomer is depleted.

The strengths of this model include the acknowledgment of several experimental observations. Due to the recognition of DLVO colloidal interaction potentials within the van Blaanderen model, not only is the sensitivity of the Stöber system to ionic strength explained, but also the number, as well as the particle size at which aggregation slows to insignificant levels, is accurately described.[55,65] Moreover, this model is able to justify the inexistence of primary particles and does not rely on unrealistic differences in the rate of hydrolysis and condensation (i.e., a system rate-limiting step of condensation due to high rate of hydrolysis but yet a slow rate of condensation), both of which are shortcomings of the Bogush et al., aggregative-growth theory.[55] Finally, this model also is successful in explaining why particles that grow faster and larger posses a rougher surface morphology. That is, the aggregative nucleation in these systems consumes more monomer, which then limits the subsequent surface smoothing through monomer addition.[65]

Formation of polymeric nanoparticle dispersions

The third type of nanoparticle used extensively within this thesis is organic polymeric nanoparticles. Dispersions of polymeric particles, or latexes, with nanometer dimensions are most commonly created by emulsion polymerization. Although there were a few earlier studies,[66-71] the emphasis to understand and exploit this process began in World War II.[72] This situation imposed the need to create an industrial processes to generate synthetic rubber because of the limited access to natural rubber sources. Emulsion polymerization became a prime candidate to mass-produce rubber due to inherent characteristics of the procedure

allowing practical large-scale production. Prior to discussing these attributes and their origins, it is advantageous to first examine the free-radical polymerization process itself.

Free-radical polymerization. In its most simplistic terms, emulsion polymerization is a free-radical polymerization of an olefinic monomer with the characteristic stages of initiation, propagation, and termination. Free-radical polymerization proceeds first through an initiation step in which an initiator is converted into a free-radical (e.g., decomposition via a thermal or redox mechanism). This free-radical initiator adds to the olefinic monomer through breakage of the double bond and creation of a covalent linkage between the initiator and monomer. The remaining free electron from the double bond is then shifted toward the opposite end of the monomer, creating a free-radical monomer unit.[73] With the activated monomer, polymerization commences through the continued addition of the radical to one end of a double bond of a monomer, and subsequent shifting of the radical to the free end of the growing polymer chain. Growth continues until the oligomeric radical combines with another radical unit (i.e., oligomeric radical, monomeric radical or initiator radical), which then terminates growth. Emulsion polymerization is just one of many polymerization mechanisms that utilize free-radical growth. The advantages of the emulsion polymerization over other free-radical polymerization processes, is a result of several factors associated with the emulsion polymerization process such as other components (e.g., surfactant), the physical and chemical properties of these components, as well as the localization of these components within the overall system.

Advantages of emulsion polymerization process. The benefits of emulsion polymerization are most evident when considering issues related to industrial-sized processes. Emulsion polymerization is easily controlled and utilizes a low viscosity and high heat transfer reaction medium, thus facilitating fluid motility as well as system cooling.[74,75] Moreover, the final product dispersion can usually be employed without further isolation. Arguably, the largest advantage is that emulsion polymerization allows for the formation of very high molecular weight polymers at reasonable polymerization reaction rates.[74] Other free-radical polymerization processes have an inverse relationship between the obtained molecular weight and the rate of the reaction. In other words, the usual means to produce a high-molecular weight polymer through a free-radical methodology is to purposely lower the reaction rate (e.g., operating at lower temperatures). Emulsion polymerization, on the other hand, has been found to be free of this constraint, which has obvious industrial and research laboratory advantages to produce high molecular weight polymers.

Emulsion polymerization components and arrangement. There are four basic components in an emulsion polymerization system: water, emulsifier or surfactant, olefinic monomer, and water-soluble initiator. Water acts as the solvent in which all other components are being mixed at a controlled rate leading to the low viscosity and excellent thermal characteristics as noted earlier. Present within the water is an emulsifier or surfactant, a relatively unique ingredient for free-radical polymerization processes. This additive is commonly present at a concentration greater than its critical micelle concentration, or CMC. The CMC represents the concentration in which the surfactant is no longer homogenously solvated in an aqueous medium. Above the CMC, the hydrophobic tail

groups of the surfactant form clusters that possess a hydrophobic interior surrounded by a hydrophilic shell. Micelles typically form at concentrations ranging from 0.001 to 0.1 M.[74] The CMC, however, it is not only dependent upon the characteristics of the surfactant (i.e., hydrophobicity of tail group), but also on the presence of other additives in the reaction mixture (e.g., organic solvents). The physical size of the micelles typically falls in the range of 2-10 nm in diameter, involving approximately 50-150 surfactant molecules. These values, including the micelle concentration, are dependent upon the surfactant identity and its CMC. Furthermore, as the amount of surfactant in excess of the CMC increases, the micelle concentration increases but the diameter decreases.[74,76]

The third major component in an emulsion polymerization is the olefinic monomer. The amount and arrangement, of the monomer within the aqueous bulk depend mostly upon the hydrophobicity of the monomer. A small amount is solvated in the aqueous medium and another small portion is held within the interior of the formed micelles. The majority of the monomer (>95%), however, is present as dispersed monomer droplets whose size depends upon rate of agitation. Under typical reaction conditions, the monomer diameter lies between 1-10 micrometers. These droplets are stabilized through the addition of electrostatic charge to their surface via the adsorption of surfactant to the monomer droplet exterior.[74]

The last component is the water-soluble initiator. It is important to note that this initiator is water-soluble as another class of polymerization, known as suspension polymerization, involves the usage of oil-soluble initiator. Suspension polymerization is more of a true two-phase reaction system in which polymerization proceeds within the hydrophobic monomer droplets providing for a different set of product characteristics as compared to emulsion polymerization. This dependence of the characteristics upon the

initiator not only provides a hint to the complexity of how these components interact with one another but also bestows an impetus to understand the mechanism of emulsion polymerization.

Experimental observations of the emulsion polymerization system. As stated above, the emulsion polymerization is, in simplest terms, a free-radical polymerization scheme. The distinct characteristics, and advantages, of the emulsion polymerization system, as compared to other free-radical polymerizations, are therefore a result of its unique components as well as how and where the components interact. Prior to formulating a mechanism for emulsion polymerization in order to understand how to manipulate product characteristics, the experimental observations regarding the polymerization should be examined.

One of the classic observations of all emulsion polymerization processes is the ability to segment the overall reaction into three distinct temporal regimes regardless of experimental conditions. These intervals, coined Interval I, II, and III, are defined by the identity (i.e., monomer droplet, polymer particle, and surfactant micelle) and concentration of particles in the system as well as by the reaction rate.[72,74,76,77] Interval I is defined by an increase in polymer particle concentration to a constant level, which marks the completion of this mechanistic segment. The end of Interval I is also accompanied by the concurrent disappearance of micelles from the aqueous dispersion as well as by the onset of monomer droplet instability upon cessation of agitation.[74] The length of this period is usually the shortest of the three intervals, taking approximately 2-15% of the total reaction time.

Employing components with higher initiation rates and water solubility can shorten this interval.[74,78]

The emulsion polymerization continues in Interval II, which is characterized by a constant particle concentration and by a steady, or slight increase, in polymerization rate. The particles in this interval increase in size, while that of the monomer droplets decreases. The monomer droplets eventually disappear, marking the ending of Interval II. The duration of Interval II can be lengthened by utilizing monomers of higher hydrophobicity. The emulsion polymerization process is concluded in Interval III with the continued maintenance of particle concentration and exhaustive consumption of water solublilized monomer.[74]

Several other experimental observations have been found when altering reaction conditions.[79] One important observation is the dependence of the rate of polymerization upon micelle concentration, indicating the significance of this component. It is possible in some systems to successfully create polymeric particles with an emulsion polymerization reaction in the absence of surfactant. In addition the reaction rate of the system depends upon initiator concentration, as well as upon the volume of the aqueous phase. Finally, the particle size nests between the pre-initiation dimensions of the micelles and the monomer droplets. These observations indicate that emulsion polymerization possesses a complex, multi-faceted mechanism.

Emulsion polymerization mechanism. Any proposed mechanism, or combination of mechanisms, must account for the reaction characteristics listed above. To accommodate these observations, a proposed mechanism must have parameters whose importance is

dependent on experimental conditions. However, the potential mechanism for emulsion polymerization must begin with the common step of free-radical initiator formation.

It is generally agreed that radicals are formed throughout the continuous aqueous phase due to the extreme water solubility of the radical and initiator.[72] It is unlikely for the initiator to partition into areas of increased monomer concentration and begin propagation because of the high hydrophilicity of the radical. In order to transform the initiator into a molecule with properties that will allow initiator/monomer interaction, the radical is thought to convert into a short oligomeric radical via a limited amount of propagation with monomer solublized within the continuous aqueous phase.[72,74] This oligomeric radical acts as the initiator to the other facets of the polymerization. Although viewed to not have a significant affect on the initiation mechanism, the reaction conditions do have a drastic effect on the rest of the mechanism, or more specifically, the location of particle nucleation in the emulsion polymerization process.

Several studies, mostly by Hansen and Ugelstad[80,81] as well as Fitch and Tsai,[82] have proposed that there are multiple nucleation sites within a single emulsion polymerization reaction mixture that occur within Interval I. This concept, known as the HUFT theory, considers three competing sites of particle nucleation: nucleation in the monomer droplet, within a monomer-swollen micelle, or in the homogenous aqueous matrix. The HUFT theory claims that the dominance of one nucleation site over another, and thus alteration of the particle properties, is dictated by factors such as the physical characteristics of the monomer (i.e., hydrophobicity), agitation rate, and surfactant concentration (both above and below the CMC).[72,74,76] In order to assess which nucleation site dominates under a specified set of reaction conditions, it is worthwhile to first look at each nucleation site separately.

The first possible site of nucleation is within the monomer droplet itself. The oligo-radical would adsorb into the monomer-rich environment and begin the propogation process, leading to the formation of the primary particle. The second competing site for nucleation is within a monomer swollen micelle and was proposed by Harkin.[76] Harkin viewed this location as the ideal nucleation site under "standard" emulsion polymerization conditions (i.e., 0.1 to 0.3 % (w/w) surfactant; water to monomer ratio between 70:30 and 40:60 (w/w))[74] postulating that the micelle interior provided the optimal condition for the interaction between the water insoluble monomer and very water soluble radical.[74] The oligo-radical is adsorbed into the monomer swollen micelle and begins the rapid polymerization propagation process that yields a primary polymer particle.

The final third proposed site for nucleation is known as homogeneous nucleation and was proposed by Fitch and co-workers[83] as well as by Hansen and Ugelstad.[80] Homogenous nucleation takes place entirely in the aqueous phase and involves the continued propagation of the initiated oligo-radical until a critical sized is achieved. This critical size is defined as the point where the growing polymer chain can no longer be solvated and thus precipitates and collapses on itself, forming a primary polymer particle.[18,19,74] In all three of the nucleation sites, the end product is a primary particle. The HUFT theory considers nucleation to occur in all three sites; but the dominance of one site over another is dependent upon the reaction conditions.

The HUFT theory proposes that the monomer droplet is the least likely of the three nucleation sites simply from a geometric surface area argument. Utilizing the above "standardized" emulsion polymerization components[74] and assuming the individual monomer droplets posses a typical diameter of 1-μm, the total cross-sectional areas of all of

the monomer droplets to all of the micelles in the system is approximately 1:30.[72] Likewise, the total cross-sectional area ratio between the solublized monomer (i.e., styrene) and the monomer droplets is 2.5:1. Because of these surface area ratios, probability alone dictates that the oligomeric radicals will not interact to as great of an extent with the monomer droplets as with the components of the other two nucleation sites.[72] These ratios can be altered by significantly increasing the agitation rate, thus reducing the size of the monomer droplets and the differences in surface area ratios. This adjustment of reaction conditions allows the monomer droplets to become a significant source of particle nucleation. The conditions necessitated for this to occur are recognized as a special sub-class of emulsion polymerization referred to as microemulsion polymerization. Even in these situations only about 1 in every 20 droplets capture a radical and instigate nucleation.[76]

The HUFT theory claims that the majority of particle nucleation occurs through homogenous and micelle-based nucleation. In a typical system, only 1 out of every 100 to 1000 micelles capture an oligo-radical.[72,76] (These "un-used" micelles serve an important purpose in Interval II and III and will be discussed in greater detail below.) Micelle-based nucleation does, however, explain several observed characteristics (i.e., particle number dependence on micelle concentration, cessation of particle nucleation upon disappearance of micelles). Homogenous nucleation also helps account for the nucleation of particles when the surfactant is below its CMC, thus no micelles are present. The system can be altered to allow homogenous nucleation to dominate by employing a more hydrophilic monomer as well as by keeping the surfactant level below the CMC.

Primary particle formation continues through a combination of the above three nucleation sites until excess surfactant in the un-used micelles is depleted. At this point,

which also marks the end of Interval I, particle production is halted as all newly formed primary particles become unstable. This situation reflects the lack of surfactant available to coat and therefore stabilize the particles.[74,76] These primary particles that are nucleated after Interval I (via either monomer droplet or homogenous nucleation, as the micelles are now absent), aggregate upon other growing particles surfaces.[20]

Primary particle stabilization and growth. Upon nucleation of the primary particles, the first concern is maintenance of the particles as a stable dispersion within the aqueous medium. To this end, the primary particles are required to have properties dictated by DLVO theory. One means to impart stability is to adsorb solvated surfactant or surfactant from the "un-used" micelles (or micelles that did not act as a nucleation site) on the particles in order to provide electrostatic charge stabilization. If surfactant adsorption does not occur, the particles will become unstable and begin to coagulate into larger particles until stability is achieved in accordance with the size-dependent aspects of DLVO theory.[20] This growth through co-aggulation is system dependent as if enough free-surfactant is present the nucleated particles will remain stable.

With the particle number now holding constant, Interval II begins and is dominated by the growth of primary particles via diffusion of the monomer through the aqueous phase from monomer droplets.[74] Growth continues until the monomer droplet "reserves" are depleted through incorporation into the growing monomer-swollen particles.[74,76] The disappearance of the monomer droplets signals the end of Interval II and the beginning of Interval III. In this final interval, polymerization of the solvated and particle-entrapped monomers continues until depletion.

During the entire growth process (Interval II and III), it is possible for a second radical (e.g., oligo-radical) to enter the growing particle. Due to the small size of the particle interior, the inclusion of a second radical results in the rapid termination of the polymerization reaction. Particles are thus considered to contain no more than one radical at any point in time.[72,74] Monomer uptake into the particle is still allowed to continue upon cessation of polymerization but particle growth is effectively "dead" until another radical is adsorbed into the particle re-initiating propagation. Individual particles therefore undergo an initiator dependent, discontinuous type of growth that results in the observed system dependence on initiator concentration.

Monodispersity within emulsion polymerization. As noted, particle monodispersity is an issue of extreme importance in reference to their application within the analytical sciences. At first glance, the emulsion polymerization mechanism provided does not inherently address particle size homogeneity. To obtain monodisperse particles, the particles must follow a LaMer growth model through burst nucleation (i.e., nucleate at the same time) and exhibit similar growth rates.[75,78,84] Nucleation can be limited through the reduction of Interval I by utilization of a more water-soluble monomer, which increases radical access to micelle interior.[74] Another means to enhance radical access is to employ a mixed surfactant system that will increase the surface area of the micelles as well as reduce the surface charge density of the micelle.[78] After the attainment of "burst" nucleation, equalizing the growth rates for all the particles furthers monodispersity.[84] This situation can be realized through a monomer-addition self-sharpening mechanism, which was described in the discussion of the growth of silica nanoparticles.[58]

Self-assembled nanoparticle structures

Nanoparticles have been used for a variety of purposes ranging from immunological agglutination tests[85,86] to electrochemical material studies.[24] More recently, numerous research efforts have investigated the assembly of nanoparticles for the creation of differing analytical surface platforms.[87] Several methods to assemble nanoparticles on surfaces have evolved from these studies. The commonality between these procedures is self-assembly of the particles into an organized pattern on a surface based upon their properties. The self-assembly of nanoparticles provides an extremely elegant means to create and control microscopic structures, serving as a basis for developing a wide range of analytical platforms and methods. The following briefly overviews several of the broad categories involved with the creation of self-assembled patterns of nanoparticles and are presented in an order of increasing complexity and engineering/procedural requirements.

Self-assembly of crystals from nanoparticles

Assembly through sedimentation. The simplest nanoparticle patterns that can be self-assembled are crystalline arrays. Even so, there exists a plethora of means to accomplish this task. Perhaps the most facile means to form a crystalline array of nanoparticles is through the sedimentation of the nanoparticles in a colloidal dispersion onto a substrate. In these cases, gravitational forces pull the nanoparticles to a surface at a velocity determined by Stokes Law (14):[88]

$$v = \frac{d^2(\rho_p - \rho_l)g}{18\eta_L} \tag{14}$$

where d is the particle diameter, ρ_p and ρ_l are correspondingly the density of the particle and the dispersing matrix, g is the acceleration due to gravity, and η_L is the viscosity of the dispersing matrix. The deposition of the nanoparticle upon the growing crystal in this system is near equilibrium because the thermal energy of the particles is roughly equivalent to their gravitational energy.[89] As a consequence, the nanoparticles, which are assumed to be hard spheres, have the ability to diffuse along the growing nanoparticle array and find the most thermodynamically favorable surface site. On flat surfaces, this energetically favorable crystalline orientation is a fcc crystal with the <111> facet parallel to the surface.[90] Although technically simplistic, this method requires 5-20 days for sample preparation.[89] An alternative method, which requires less preparation time, allows a nanoparticle dispersion to evaporatively deposit on a solvent-wettable substrate.

Assembly through evaporation. This self-assembly method was originally described by Perrin when working with monodisperse gomme-gutte spherical particles.[91] Since then, many other groups have exploited this method to create 2-D crystalline arrays of silica, polymer, semiconductor, virus, and bacterial nanoparticles.[92] The mechanism for the growth of these assemblies has been thoroughly studied by Nagayama and by Dushkin. In their earlier works to establish the formation mechanism,[93] an experimental apparatus was constructed such that the nanoparticles present in a concave droplet could be observed with a microscope during matrix evaporation on a wettable substrate. Several of the systems physical and chemical properties (such as particle dispersity, particle concentration, electrolyte concentration, surfactant, medium evaporation rate, and droplet shape) were altered to observe the effect upon colloidal ordering. The process was discovered to begin

with all particles undergoing Brownian motion. It was only after the medium had evaporated to the point where the solution thickness was less than the particles diameter, which occurred in the center of the concave droplet, would the particles begin to be drawn to the substrate and began to nucleate.

Due to the wettability of the particles, a slightly thicker meniscus of medium would form around the particles on the substrate within the nucleation area. When the meniscus of two particles, or aggregate of particles, made contact within this thinned area, the particles would move towards each other. Upon contact, particles would incorporate themselves into a growing ordered phase. It was also discovered that the particle size, concentration, electrolyte, and droplet shape controlled the size of the ordered domains. Moreover, the rate of evaporation, particle monodispersity, and substrate wettability were found to be crucial factors in forming an array.

Based upon these observations,[93] as well as those from subsequent investigations,[94-100] the mechanism for 2-D particle orientation and growth was theorized to be independent of long-range electrostatic forces because changes in electrolyte concentrations had no observable effect on particle ordering. The mechanism therefore begins with a nucleation step in which evaporation leads to a film with a thickness that approaches the size of the particles. The particles within the nucleation area adhere to the substrate and form a meniscus. The meniscuses of the individual particles in the nucleation area interact resulting in lateral movement of the particles towards each other due to a strong, tangential, and long-range force known as immersion capillary forces.[92] These particles upon physical contact interact and form the nuclei.[92] After nuclei formation, growth of the particles into an ordered 2-D crystal domain is proposed to continue through additional medium evaporation.

2-D crystal growth continues with the evaporation of the liquid medium not only from the bulk but also from the meniscus in between the particles within the nucleated region. Since the particles in the nucleus are wettable (i.e., hydrophilic in a aqueous dispersion), they draw liquid from the "bulk" toward the nucleus to replenish the liquid in the meniscus. This inward convective flux results in the movement of the dispersed nanoparticles through hydrodynamic drag. The particles that move as a result of the convective flux eventually reach the nucleus and combine with the growing ordered array, again in the most energetically favored position, a <111> facet. Although similar in simplicity to the sedimentation method, this process does have slightly higher protocol requirements.

The most important requirement for obtaining 2-D crystals is substrate wettability. That is, the substrate must be wettable by the dispersing medium to provide a stable thin film and allow the progression of nucleation. The substrate must also be smooth and the particles monodisperse in order to obtain a single nucleation sight and commensurately minimize the number of domains. This situation enhances the growth and size of ordered domains. If these requirements are not met, the particles will protrude out of the evaporating film, deforming the liquid surface, forming more nuclei. Furthermore, not only must the particles be monodisperse, but they must also be larger than approximately 120 nm in diameter because water, the most common dispersion medium, does not form stable films below this value.[101] If the particles are smaller than this minimum thickness, the particles will not deform the film surface and initiate the immersion forces and the associated lateral movement. Finally, slower evaporation rates lead to larger domains as fast evaporation disrupts the lateral capillary immersion forces and result in multiple growth fronts.[92]

There are several adaptations of this technique that utilize similar growth mechanisms. The first two variations simply alter the area in which the film thickness approaches nanoparticles size. If a convex droplet is used, the film thickness will be reduced at the outer edges of the droplet first and lead to array growth from the outside of the droplet toward its center.[101,102] Likewise, if the sample is inclined at an angle, the film thickness at the top edge of the droplet will be lower due to the effects of gravity. The array growth subsequently begins at the outer edge of such droplets.[101,102]

Other variations include employing a spin coater to remove liquid from the substrate through centrifugal forces.[103,104] This procedure is usually optimized through trial and error. However, once the proper conditions are identified, it requires significantly less time to prepare a sample. One other final variation of this growth mechanism is referred to as vertical deposition.[92,105,106] This procedure occurs by withdrawing the wetted substrate from a suspension at a rate that is equal to the rate of meniscus retraction due to evaporation. As is well known, a meniscus will form on a wettable substrate with a thickness that is a function of height above the liquid level. At the point where the film thickness is comparable to particle diameter, nucleation, and growth occur as outlined above.

Assembly through electrophoretic deposition. Other means to create crystalline arrays require more complex approaches and include techniques like electrophoretic deposition.[107-114] As stated earlier, colloids forming stable dispersions commonly have a surface bound electrostatic moiety, giving the particle an overall surface charge. As a result of this charge, these particles will undergo an electrophoretic force when placed in an electric field and move in a direction defined by the field (e.g., negatively charged particles will

migrate toward a positively charged electrode). The magnitude of this force can be altered through adjustment of the electric field strength. Thus, this deposition method is somewhat analogous to sedimentation except the substrate in this case must be a conductor so as to establish the electric field. This approach was first reported by Richetti and co-workers,[115] but has since been fined tuned and examined in further detail to deconvolute a mechanism responsible for the growth of a ordered 2-D crystalline array.

Trau et al.[107,108] and Böhmer,[109,110] through experimental and theoretical works independently postulated two slightly different growth mechanisms for electrophoretic deposition. Both theories have the particles drawn toward the electrode surface through electrophoresis and sedimentation; however, the two theories vary in the mechanism that induced crystalline order. Böhmer attributes the aggregation of particles on the surface to electroosmotic flow of solution about the deposited nanoparticles on the electrode surface.[109,110] This flow is a result of the interaction between the electric field and the double layer of the colloid. The directionality of the flow is normal, away from the electrode near the particle and results in an overall lateral fluid flow toward the particle along the electrode surface. Since the particles (and later aggregates) reside near the electrode surface, they move toward one another due to electroosmotic lateral fluid flow. The mechanistic theory presented by Trau et al. again utilizes particles that have been drawn to the electrode surface via electrophoresis, however the 2-D lateral ordering is a result of electrohydrodynamic forces associated with electrode reaction products.[107,108]

Trau's theorized growth mechanism begins with the minute (due to low current densities of < 1 mA/cm^2) production of H_3O^+ and OH^- through the electrolysis of water. This leads to a build up of ions at the electrode surface or a concentration polarization of charged

ions. Upon a smooth and chemically uniform electrode there exists an ion concentration gradient normal to the surface but the hydrodynamic pressure gradient parallel to the electrode is at equilibrium. However, the presence of a particle, which was attracted to the electrode via electrophoresis, disrupts the hydrodynamic pressure equilibrium with its associated double layer. This disruption induces lateral fluid motion along the electrode surface toward the particle. The cumulative effect of the individual particles, with their associated pressure fields, is the lateral movement of the particles along the electrode surface towards one another. Upon particle interaction, they orient in the most thermodynamically favorable configuration, forming a <111>, 2-D crystal.

Both Trau and Böhmer have found that in order to decrease crystalline defects, the system can be placed closer to an equilibrium state by utilizing a small AC amplitude around the necessitated DC offset. This again, as in sedimentation, minimizes the formation of defects by allowing the particles to sample several surface sites to discover the most energetically favorable adsorption position.

Template-assisted assembly. All of the proceeding methods have created fcc oriented crystals with the <111> face exposed.[90] However, it is advantageous to be able to create crystals with other exposed facets, especially within the growing photonic band gap arena. Obtaining crystals with different orientations is most often accomplished through the growth of the crystal upon a substrate that has been physically altered to act as a template. With this general idea in mind, there exist several variations and manipulations of the system to induce this template-guided crystallization.

One of the first applications of a template to induce a particular crystal orientation was present by van Blaaderen and coworkers.[116,117] In this study, holes whose dimensions were of the same size as the particles that were to be used were created in a thin film through traditional lithographic techniques. The lithographically defined holes were arranged upon the surface such that they mapped out the desired crystal facet. The template was then exposed to a colloidal dispersion where sedimentation was allowed to occur. Under this near equilibrium, sedimentation condition, the authors report that it is energetically favorable for a particle to adsorb within a hole. With the first layer of particles oriented in the desired fashion, they now in turn act as the template and define the growth of subsequent layers. This method is analogous to molecular epitaxial growth, but on a mesoscopic scale, thus has been referred to as colloidal epitaxy.[116]

Utilizing this method, fcc crystals with exposed <111>, <110>, and <100> faces have been formed that were several millimeters thick. A drawback is that the size of the hole must be the same size as the particle diameter, which becomes a problem when desiring to template colloids whose size is below the diffraction limit of light and thus cannot be defined lithographically. This limitation has been somewhat rectified through employment of optical tweezers to specifically locate particles on a surface, which then again act as a template to induce epitaxial growth through sedimentation.[118] As previously mentioned, sedimentation can be a time consuming process, therefore other methods to induce crystal orientation with a template have been pursued.

One of the more physically intriguing methods to induce crystal growth on a template, which can also be considered as a mesoscopic epitaxial growth mechanism,[119] uses a bi-modal system (i.e., a system with two distinct sizes of monodisperse particles). It has

been previously shown that larger particles in a bi-modal system are pushed along a wall if the radius of curvature of the wall continuously changes.[120] This movement was attributed to forces caused by an entropic "depletion" or an excluded-volume mechanism. Yodh and co-workers exploited this phenomenon to deposit the larger particles of a bi-modal system into the corners of lithographically defined holes present in a template.[120,121]

The physical driving force for this technique is the increased entropy of the system brought about by the greater volume of space in solution accessible to the smaller particles when a larger particle deposits upon a surface. As the larger particle increases the amount of its surface that is in contact with the substrate (i.e., adsorption at a groove as opposed to a flat), it results in the concurrent increase of solution volume available to the smaller particles. The greater amount of solution volume provides for larger numbers of small particle orientations, thus raises the overall entropy of the system. This rise in entropy results in the larger particles being forced to contact the substrate with as much of its surface area as possible, thus the larger particles migrate toward the corners of the defined template. These particles then serve as a template for colloidal epitaxy growth, which is continually driven by the increase in entropy that results from the deposition of the larger particles onto the growing crystal. Although this method does not require as much preparation time, the template size is still restricted to being on the same order as the particles. Thus, the same lithographic size limitations exist as described above.

Two general techniques have been developed to avoid the particle size constraints due to lithographic limitations. The first method is to simply use templates that are naturally formed and have a periodic structure below the diffraction limit of light. This has been done by Teranishi et al. to organize gold nanoparticles into the grooves of a sodium chloride

crystal through the evaporation of a dispersion of gold nanoparticles. The nanoparticles are originally drawn into the areas of greatest contact with the substrate through capillary forces. Upon further evaporation, the convective particle flux continues to cause crystal growth.[122] In many cases however, the templates that are naturally formed do not have the long-range organization, or other features, desired by scientists. Another approach was therefore instigated by Ozin and co-workers who again utilized lithography to define a template, but the fabricated holes in the substrate are not composed of vertical walls but of tapered, sloping walls.

In these particular studies,[123-125] Ozin exploits the anisotropic etching of silicon <100> by 3 M KOH in an isopropanol/water system of specific areas as defined by photolithography. It is well known that the etch rates of crystalline silicon are dependent upon the crystal direction and that an approximate ratio of etch rates for each crystal direction is <111>:<100>:<110> = 1:300:600.[126] This results in templates whose 2-D orientation is dependent upon the pattern formed by photolithography and whose third dimension is defined by the orientation of the <111> plane that effectively acts as an etch stop. More specifically, each individual feature of the template is composed of walls, which are sloped at a 70.6° angle, and whose depth depends upon the geometry of the photolithographically defined pattern and etch time. This essentially leads to an ordered template of V-shaped groves and holes. A flat piece of poly(dimethyl)sulfoxide (PDMS), which is a well studied elastomer, is then used to cap the created structure and a drop of an aqueous dispersion of nanoparticles is injected at the interface. The dispersion is allowed to slowly evaporate from this setup.

When following this procedure, the particles are observed to first adsorb to the bottom, or apex, of the V-shaped structure because this location provides the greatest amount of contact between the particle and template surface and is thus the region of highest attractive capillary forces. If the template structure is a groove, the deposition of particles continues in the apex until a 1-D chain of particles is assembled along the apex. Next, the particles assemble adjacent to the apex particle along the sidewall. Growth continues up the walls until the reaching the top of the template that is defined by the PDMS. Particles then continue to fill the template through evaporative induced capillary forces in an fcc crystal orientation, with the <100> face being displayed due to the 70.6° angular geometry of the sloped sidewall of the template.[123] This process has been shown to be able to create organized arrays of colloidal crystals in a relatively short period of time (<2 h.) and is amendable to spin coat processing, which further reduces preparation time.[124] It should be noted that the fcc crystal structure is only obtained if the template and particle geometry are matched or commensurate. In other words, if the template geometry, more specifically the length of the apex at the base of the V-shaped template, is not a length that corresponds to an integral number of particles, incommensurate crystal growth will occur.[124]

Xia and co-workers have taken a very similar approach to that described above, where a template with 70.6° sloped walls are anisotropically etched into a Si<100> substrate.[119,127] The difference between these two approaches is revealed within the apparatus and procedural design. Xia and workers did not constrict the particles to only the etched template, as Ozin did with the bounding slab of PDMS. Xia and co-workers also employed a combination of sedimentation and evaporative induced capillary forces as the dispersion was introduced to the template and then sonicated for ~ 1 day prior to drawing off

the excess dispersion and allowing the structure to air dry.[128] Using this procedure, colloidal crystals with the <100> plane oriented parallel to the substrate surface were again obtained and the orientation ascribed to the sloped sidewalls of the template.[119,127] The dependence of the ratio between the template geometry and particle size in growing a true fcc crystal was also confirmed through these studies. An interesting observation noted within these studies is that if the colloidal crystals were allowed to grow to a height sufficient to exceed the depth of the template, and deposit on a flat surface of the template between etched holes, the template would no longer define the crystal growth. The crystal would undergo twinning and grow with the <111> face oriented parallel to the surface.[119,127] This clearly shows that the sloped wall of the template is responsible for the orientation of colloidal crystal growth.

On a related note, Xia's group has been extremely active in this arena of creating complex aggregates of particles in a controlled orientation through prudent choice of the ratio between template dimensions and particle size.[129,130] Through evaporation of a colloidal dispersion upon a photolithographically defined template, the individual holes are filled through a continuous dewetting/colloidal force mechanism.[131] Many intriguing, yet controlled, shapes and crystals, including those with proscribed handedness,[130] have been created.

Patterned crystals of nanoparticles formed through self-assembly

All of the previously discussed deposition methods have created well-organized colloidal crystals from a dispersion. However, many times the overall shape of the structure, such as channels or walls, created with nanoparticles is more important than the formation of a well-defined crystal. As a consequence, several techniques have been created to pattern

nanoparticles in desired crystalline and non-crystalline, mesoscopic architectures. Many of these methods are tangents to the above-discussed procedures, and add the usage of both UV irradiation and electrophoretic deposition to obtain a desired pattern.

Patterned electrophoretic deposition. Electrophoretic deposition, as discussed above, inherently provides a means to draw to and laterally organize particles on a surface, through either electroosmotic[110] or hydrodynamic convection.[108] The structure can be further patterned through the employment of lithography to selectively mask areas of the electrode. This masking blocks particle access and allows particle assembly only upon the exposed electrode regions.[114] A more elegant means to impose a mesoscale pattern upon the colloidal crystal on the electrode surface was shown by Hayward et al.[112] In this study, a transparent semiconductor electrode (i.e., indium-tin-oxide or ITO) was irradiated with UV light through a photomask. It is well known that light impinging upon a semiconductor alters the current density at the electrode interface. Therefore areas of increased current density are formed by selectively illuminating areas of the electrode. The particles are then swept into these areas of increased current density due to the theorized fluid convection.[114] Although these methods provide a crystalline array in a controlled pattern, they are still constrained by the ability of electrophoretic deposition to form a structure that is more than a few particles in thickness. To avoid this limitation, other methods have been conceived by Whitesides and co-workers that will create a mesoscopic pattern composed of a colloidal crystal of a controlled height.

Patterning with micromolding in capillaries. Through the use of microchannels that have been formed in the desired pattern or shape as a relief structure in PDMS, mesoscale patterns of controlled shape and height have been fabricated from colloidal crystals.[132,133] This methodology, coined micromolding in capillaries or MIMIC, involves an elastomer with a pre-patterned relief structure of microchannels being placed on a substrate and then filled with a nanoparticle dispersion through capillary action. The dispersion is allowed to slowly evaporate within the channels, both with and without sonication. Upon removal of the PDMS template, crystalline arrays of the particles are revealed replicating the height and shape of the channels. The colloids pack into a fcc crystal with the <111> plane being oriented parallel to the substrate surface, which is attributed to immersion capillary forces and convective flow that occur during an evaporation colloidal deposition process.[132] Kralchevsky and Nagayama however theorize that the crystalline growth mechanism is due to a phenomenon known as the Kirkwood-Alder phase transition. This type of crystalline freezing occurs between particles when they are repulsive to one another but are trapped in a confined environment.[92] This scenario does exist with the nanoparticles between the micromold and the substrate, however no further supportive experimental evidence is provided.

Controllable non-crystalline, self-assembled nanoparticle patterns

Although desired in some circumstances, there are several applications that do not require particles being assembled into a well-ordered structure. This section briefly discusses a few of these examples.

Magnetophoretic deposition. One such technique to pattern nanoparticles in a non-crystalline fashion has been through the employment of magnetic nanoparticles and imposed magnetic fields.[134-139] The arrangement of the magnetic particles in this procedure, known as magnetophoretic deposition, is a result of the nanoparticles forming a net magnetic dipole in the presence of a magnetic field.[134] The resulting dipolar interactions overcome Brownian motion and assemble along the applied magnetic field lines. This method does not, however, organize the particles in a crystalline fashion.[138] There are also problems associated with the lack of control over the magnetic field lines for users to dictate pattern formation. Besides these limitations, considerable amounts of research effort are still being placed into overcoming these obstacles and utilize this class of nanoparticles to create structures upon a surface.[140]

Organizing with patterned electrostatic charge. Electrostatic interaction between the nanoparticles and the substrate represent another technique that arranges nanoparticles in a user defined mesoscopic, yet non-crystalline, pattern. Controlled areas of isolated charge, which are used to attract oppositely charged colloids from a dispersion, have been created through a variety of means. Fudouzi's group created isolated areas of positive charge due to implanted Ga^+ from a Ga^+-focused ion beam.[141,142] These patterned substrates selectively assembled negatively charged polymeric[141] or silica[142] nanoparticles onto the positively charged areas when exposed to the nanoparticle dispersions.

Similarly, electrostatic interactions were used to pattern iron oxide and graphite nanoparticles onto isolated areas of charge.[143] In these experiments however, the isolated areas of charge were placed upon thin films of PMMA, which were supported upon a rigid

conductive substrate. Charge was localized upon the supported PMMA through placing the substrate into conformal contact with a gold-covered, patterned relief structure in PDMS. A potential difference was then created between the stamp and the substrate resulting in the PMMA slab acquiring charge only in the areas of contact, thus forming a pattern of isolated charge. When this electrostatically patterned substrate was exposed to particles of opposite charge, they selectively adsorbed to the patterned regions.

Finally, a low-throughput means to pattern isolated areas of charge that again attract particles of opposite charge is to bias a scanning probe microscopy (SPM) tip in respect to a substrate. A pattern is then drawn upon the substrate.[144] Although this method provides the user with a great amount of patterning flexibility, the area that can be patterned is limited. It is also noted that SPM tips have been used on multiple occasions to physically manipulate the location of particles already present upon a substrate into a desired pattern. These methods will not be discussed, as the issue at hand in this thesis is the high-throughput formation of nanoparticle patterns as allowed by self-assembly. A few references[145-154] are included here as it is still a viable means to pattern nanoparticles.

Self-assembly of nanoparticles upon patterned self-assembled monolayers. One of the most diverse, and subsequently most applied, means to position nanoparticles upon substrates is through chemical and physical interactions between the dispersed nanoparticles and a self-assembled organic monolayer. Self-assembled monolayers (SAMs) can be generally considered to be composed of three units: a substrate binding moiety, chain linker/spacer, and a terminal functional group.[155] It is a combination of these three units that control the overall interfacial chemistry that the modified substrate displays. SAMs have

found extensive usage for several reasons. One such reason is that the formation and physical/chemical characteristics of monolayers upon a variety of substrates have been studied extensively, particularly upon silicon[155] and gold.[155-159] These studies have provided a means to reproducibly prepare a substrate with known interfacial physical and chemical characteristics. Moreover, the properties of these monolayers can be predicted and tailored through the judicious choice of chain linker and terminal groups, providing a range of mechanisms through which nanoparticles can interact with the tailored substrate such as adhesion and covalent bonding.

Possibly the most relevant aspect to using monolayers to achieve a controlled design of nanoparticles is that there exist several methods to pattern monolayers themselves. This situation provides the ability to cast one monolayer that will allow particle interaction against another monolayer that inhibits adsorption in a desired 2-D orientation. The patterning of monolayers to control and dictate the orientation of nanoparticle structures upon a surface has been accomplished through several differing techniques including SPM tip manipulation, micro-contact printing, and photolithography.

Patterning a monolayer with a SPM probe is one of the more recent techniques to spatially control chemical functional groups on a surface. There exist two discrete means through which an SPM probe can alter the chemical homogeneity of a monolayer: chemical or physical manipulation. Schultz's group accomplished one of the earlier studies of chemically patterning a selected region of a monolayer with an SPM probe.[160] In this report, a Pt-coated probe specifically catalyzed a reaction of the monolayer terminal group in the probe/monolayer interaction region. Nanoparticles were then covalently attached to this

newly modified monolayer region. Others have used this tip-catalyzed reaction of terminal groups as well.[161,162]

Another route to chemically alter a terminal group in a specified pattern is to apply a potential between a conducting SPM probe and the substrate thus oxidizing, or reducing, the monolayer terminal group. This has been shown to be able to further chemically manipulate the monolayer in order to deposit gold clusters.[163] The number of terminal groups that can be chemically altered through tip induced catalysis or oxidation/reduction and obtain a useful functional group is limited. This has resulted in the majority of efforts being placed upon removing an initial monolayer in a designated pattern and then back-filling the newly exposed region with a monolayer displaying a different terminal group. This has been achieved most commonly in a chemical fashion through application of an electric potential between the tip and the substrate that will alter the interaction between the substrate and the monolayers linker moiety. Through these means, the monolayer is removed from the surface and nanoparticles can either be deposited directly into the exposed area[164] or another monolayer can be placed in the area that will induce deposition of polymer,[165] gold,[166,167] or silica,[168] nanoparticles. Monolayers have also been selectively removed from desired areas through physically "scrapping" the monolayers from the surface.[169-173]

Using an SPM probe to pattern a surface, although providing a great amount of spatial control and patterning flexibility, is an extremely low-through put means to pattern a substrate over a large area. Tip arrays have been suggested as a means to avoid these constraints, yet the complexity of tip array usage and fabrication still remain significant hurdles.[174] To provide long range patterning, other techniques have been employed to create segregated patterns of functional groups. Again these protocols either initially place a

monolayer upon a substrate in a pattern and subsequently back-fill, or selectively remove an initial monolayer in the desired pattern and again back-fill a secondary thiol into the freshly exposed regions.

Through the usage of microcontact printing, as originally pioneered by Whitesides and co-workers to create spatially segregated monolayer patterns,[175,176] a monolayer can be placed upon a bare substrate through "inking" a PDMS stamp, that contains a patterned relief structure, with the monolayer of interest. A secondary monolayer can then be deposited in the un-patterned areas through traditional solution deposition. Using this method, a variety of different particles have been selectively patterned on a substrate including gold[177,178] and polymeric[179] nanoparticles. This approach has also been employed to pattern polyelectrolytes, which Hammond and co-workers then deposit silica particles upon.[180] As mentioned above, an alternative method to creating a pattern of monolayers with differing terminal groups on surface is to selectively remove an initial monolayer in the desired pattern and re-deposit a secondary monolayer into the freshly exposed regions.

The most common means to accomplish this task of selectively removing a monolayer is through is through ultraviolet (UV) or electron beam lithography and a photomask. Monolayers on silicon have been removed through both deep UV irradiation[181,182] as well as electron beam lithography[183] through a mask. The monolayers on silicon, upon UV and e-beam irradiation, are removed through the degradation of the C-C bonds and eventually the Si-C bond. This processing creates an area of SiO_2 within the irritated region that is then available for another monolayer, with a different terminal group, to be deposited.

As for thiol monolayers on gold, UV irradiation through a photomask is the most commonly used means to selectively remove a thiol monolayer.[184-186] It is suggested that the mechanism involved is the C-C scission by UV light and oxidation of the sulfur group by ozone created through UV irradiation of surrounding molecular oxygen.[187,188] The oxidized form of sulfur is easily displaced from the irradiated region through introduction to an organic solvent or another thiol species. Employing either of these two methods to selectively pattern a monolayer upon a substrate, polymeric,[189] silica,[190] and gold[191] nanoparticles have been exclusively orientated upon a surface in a controlled manner.

Fundamentals of atomic force microscopy

In order to effectively interrogate the morphology of nanoparticles, as well as the structures and patterns created from them, instrumentation beyond the capabilities of traditional light based microscopies must be employed. This requirement is a direct result of the particles being physically smaller than the diffraction limit of light.[192] Examples of non-light based microscopies that are able to image within this size regime include scanning electron microscopy (SEM), transmission electron microscopy (TEM), and scanning probe microscopy (SPM). SEM and TEM utilize a focused beam of electrons, which posses a wavelength much smaller than that of visible light, but are commonly restricted to operation in a vacuum environment.[193] SPM, on the other hand, is amendable to imaging in a variety of environments including vacuum, air, and liquid. SPM is also capable of providing information about the material properties. Several excellent reviews and books exist within the literature that describe the many variants of SPM, including hardware and characterization capacities.[194-197] This section will however be restricted to a brief

discussion of the inception, instrument design, and detection capabilities of one particular member of the SPM family, the atomic force microscope or AFM.

Whereas SEM and TEM utilize a focused beam of electrons to image a sample, SPM, including AFM, employ the controlled movements of an extremely fine probe. This probe, an example of which is depicted at the end of a cantilever in Figure 1, has a radius of

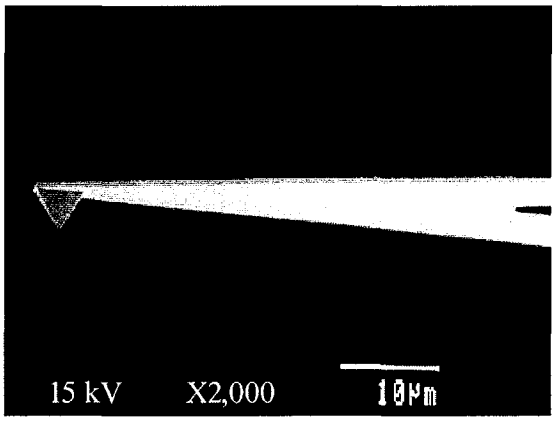

Figure 1. Scanning electron microscope image of a typical silicon nitride SPM probe

curvature ranging from tens of angstrom to tens of nanometers. As the tip is rastered over the sample in a controlled x-y pattern, the interactions of the probe with the sample are monitored. These tip/sample interactions are derived from a variety of differing physical phenomenon depending upon the characteristics of the tip, sample, and SPM imaging mode. The interactions are then translated into a map of morphology, or other properties, as a function of position in x-y space.

The first member of the SPM family was scanning tunneling microscopy (STM), as introduced by Binning et al.[198] This technique correlates a tunneling current between a conductive, biased probe and a conductive sample to map surface electron density, which is often interpreted as a measure of surface topography. STM provided one of the first

techniques that was able to obtain direct images of a conductive substrate down to the atomic level. The significance of this technique is displayed by simply noting the unheard of passage of a mere 4 years between the first published paper on STM and its authors Binning and Roher obtaining the 1986 Nobel Prize in Physics.[199] Although a powerful technique, STM is limited to imaging conductive samples. AFM was created by the same group responsible for the development of STM to remedy this particular limitation and allow for the imaging of non-conductive substrates.[200]

AFM, as it is a part of the SPM community, employs a probe to interrogate the surface of a sample and create a topographical map as generally dictated by movement of the cantilever attached to the probe tip. Importantly, the movement of the cantilever is a result of several physical forces. These forces are determined by the total intermolecular pair potential between the probe and substrate, which is the summation of all the attractive (e.g., van der Waals, electrostatic, magnetic) and repulsive (e.g., Bohr repulsion, electrostatic, elastic, magnetic) potentials.[4,9,201]

Probes that are most commonly used in AFM are composed of silicon nitride or silicon due to the ability to batch process these materials in a lithographic manner.[126,202,203] Furthermore, utilization of this material and microfabrication allows selective and controlled etching, which permits the probes, with a radius of curvature varying from 10-50 nm, to be fully integrated onto the cantilever.[194] Other methods exist through which probes of differing material properties and radius can be placed upon the cantilever (i.e., nanoparticles,[204] carbon nanotube[205-207]) but tend to be serial in production. Overall, probe choice is based upon the magnitude of the forces applied to the surface as well as the properties of the surface that are to be characterized.

Not only has an evolution of tip design/fabrication protocols occurred, but there also exists a range of means to detect the interaction between the probe and surface. The unifying theme amongst these methods is that the cantilever movement, usually a vertical deflection, is monitored and related to probe/sample interactions. Methods to observe cantilever movement include: placing a bias voltage between a STM tip and the AFM cantilever, which the STM tip is aligned above, and correlate the changes in tunneling current to cantilever movements;[9] examine changes in capacitance between the cantilever and an adjacent stationary plate;[9] microfabrication of a piezoresistive material into the cantilever and monitor the voltage change as a function of cantilever stress;[208] reflection of a laser beam off the cantilever backing and observing either the diode laser gain,[9] interference pattern,[9,209] or physical movements of the reflected spot upon a photodiode.[210] It is this last method, known as the optical-lever deflection design, that is the most utilized probe/sample interaction detection mechanism in AFM.

The popularity of the optical lever orientation is due to many factors including the capability of this method to monitor vertical deflections of the cantilever at the sub-angstrom level (0.1 Å).[9] This detection mechanism is attractive because it does not require an alteration of the physical characteristics of the probe, limit the movement of the probe, or apply additional forces upon the cantilever.[9] Moreover, this design is compact and can be operated in a variety of environments. Due to these attributes, most commercial AFM designs, such as the AFM employed in this thesis, use this optical-lever mechanism to determine probe-samples interactions.

The optical-lever design, as shown in Figure 2, is composed of four major components: x-y-z piezoelectric scanner, tip/cantilever assembly, laser/photodiode detection

hardware, and feedback circuitry and software (not shown). The sample is mounted on the x-y-z piezoelectric scanner, which is responsible for the procedures ability to controllably map probe/sample interactions on the x, y, and z-dimensions with sub-angstrom control. These extremely precise movements are a result of the intrinsic properties of the piezoelectric ceramic whose individual unit cells undergo minute, yet exact deformations when a relatively

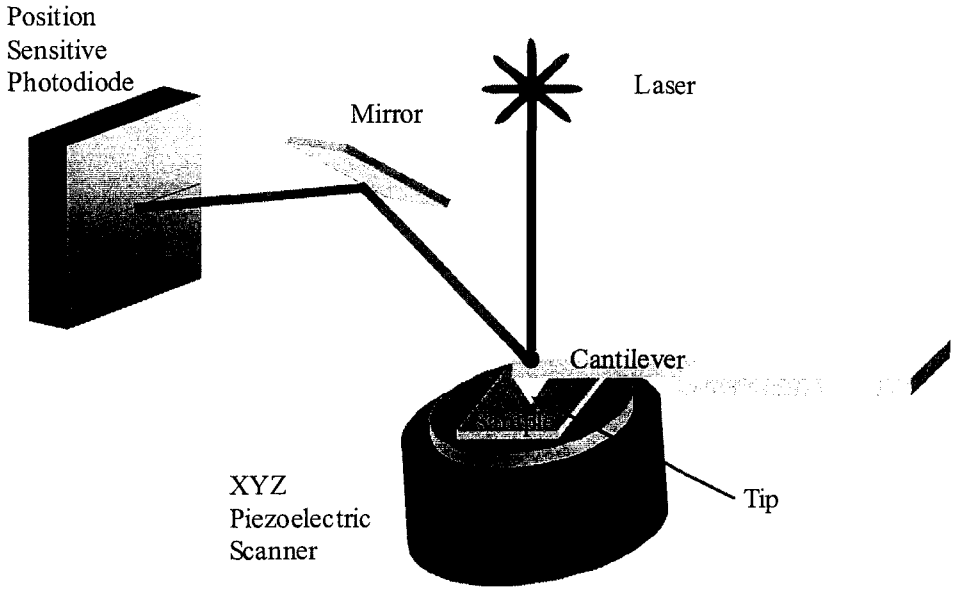

Figure 2. Optical-lever scanning probe microscope design

large (i.e., hundreds of volts/m) electric field is applied across the ceramic.[211-214] A common example of such a piezoelectric material is quartz. SPM scanners most commonly use a lead-zirconium-titanate, or PZT, ceramic ($Pb(Zr_xTi_{1-x})O_3$)[212,214] which has a sensitivity that is an order of magnitude greater than quartz.[214] The piezo scanner is generally manufactured in a tube scanner orientation for SPM applications. This orientation allows for spatial control in all three dimensions while providing for a relatively large scan size.[211] Upon calibration of the scanner with a sample of known x, y, and z dimensions, the x and y movements are

accurate to better than ± 1% and the z-axis is accurate to ± 3%.[215] These values represent the inaccuracy of the calibration standard more than that of the scanner.

The sample of interest is placed upon this scanner and rastered beneath the probe in a controlled x-y pattern. The deflection of the cantilever changes in proportion to the alteration of the probe/sample interactions at differing positions upon the substrate. This deflection is monitored through the reflection of an aligned laser beam off the back of the cantilever onto a position sensitive photodiode, which consists of two photodiodes that are electrically connected in a Wheatstone bridge configuration. Prior to sample interrogation and subsequent cantilever deflection, the laser beam is positioned equally between the photodiodes producing a null signal. Only upon cantilever deflection will the laser beam move and produce a voltage difference from the Wheatstone bridge, creating a signal.

The final component of this instrumental design includes the feedback circuitry and software and is responsible for concerting and organizing all of the collected information and component movements to produce an image. The surface information that can be collected with an AFM of this design includes interfacial free energy,[216-219] and elasticity,[220] but most commonly the AFM is used to map the topography of a sample as a function of x-y coordinates.

Two AFM topographic imaging protocols that are most often employed are contact and tapping (or intermittent-contact) mode. Contact mode, as displayed in Figure 3A, determines topography as a function of x-y position by placing the probe into physical contact with the substrate. If the tip encounters an area of increased height, as it is rastered across the sample, the cantilever will deflect upwards. This change in-turn results in the movement of the laser spot on the photodiode that the feedback circuitry recognizes. The

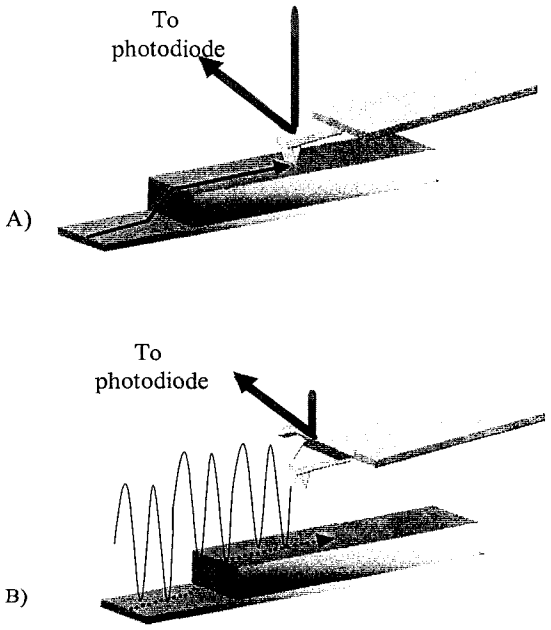

Figure 3. AFM topography modes. A: Contact Mode. B: Tapping Mode

piezo scanner is then directed by the feedback circuitry to lower the z-dimension until the cantilever is returned to its original position. The movement of the z-axis is recorded and displayed within the image as an area of increased topography.

Although topography can be measured as a direct correlation of cantilever deflection without feedback circuitry intervention, the range of heights that could readily be probed would be severely compromised. This situation is a result of the limited degree of cantilever deflection that can be obtained prior to either the reflected laser beam illuminating only one of the two photodiodes or the cantilever physically breaking. Thus, through usage of this homeostatic feedback mechanism, the range of heights that can be imaged is greatly increased and now becomes limited by the scanners z-range capabilities.

The force being applied to the surface (F_N) by the probe in contact mode can be calculated by (15):

$$F_N = k_N S_{PD} V_{PD} \tag{15}$$

where k_N is the cantilevers normal spring constant, S_{PD} is the sensitivity of the photodiode (as attained via calibration), and V_{PD} is the photodiode voltage. The product of the S_{PD} and V_{PD} is a measure of cantilever deflection and is sensitive to ~ 0.01 nm for commercially available instrumentation operating under normal conditions.[9,194] Cantilevers are produced with a variety of spring constants that range from 0.01 to 100-N/m resulting in the overall achievement of normal forces in contact mode that extend between 10^{-13} to 10^{-8} N.[9,194] However, the probe in contact mode is effectively being "dragged" across the surface, thus applying lateral forces upon the sample as well. In some cases these lateral forces may disrupt or modify the surface architecture. As a means to reduce the applied lateral forces, tapping, or intermittent-contact, were created.[221,222]

Tapping mode involves the oscillation of the cantilever/probe near its resonance frequency. This cantilever/probe oscillatory motion can be described as a forced harmonic oscillator with dampening (16):

$$m\frac{d^2z}{dt^2} + \frac{m\omega_0}{Q}\frac{dz}{dt} + kz = F_0\cos(\omega t) + F_{ts} \tag{16}$$

where m is the mass of the spring, k is the spring constant, ω_o is the angular resonance frequency of the spring, Q represents the quality factor of the spring, F_o is the driving force amplitude, ω is the angular frequency of the driving force, t is time, and F_{ts} represents other external forces upon the oscillator.[223,224] As the tip and sample periodically come into contact, the amplitude of the resonating cantilever/probe (A_s), which is set prior to sample engagement, is monitored. The normal force applied to the sample during each probe/sample interaction can be estimated through (17):

$$F_N = k_N\left(\frac{(A_0 - A_s)}{Q}\right) \tag{17}$$

where A_0 is the free amplitude oscillation of the cantilever and As is the set-point amplitude.[221] Although the normal forces applied to the substrate in tapping mode under normal operating conditions are comparable to contact mode (~10^{-10} to 10^{-9} N), the probe/surface lateral forces are greatly attenuated. This is a result of x-y movement only when the probe and sample are not interacting.

Tapping mode acquires a topographic image as depicted in Figure 3B, where the amplitude of the oscillating cantilever is diminished if the tip encounters an area of increased topography. The feedback circuitry recognizes this change through the laser/split photodiode detection apparatus, and lowers the sample until the original amplitude is retained. As in contact mode, the use of this homeostatic feedback circuitry, the z-range that can be observed depends upon the scanner and not the tip/probe characteristics or detection mechanism. It is this mode of the AFM that is employed throughout this thesis to interrogate either individual particle morphology or nanoparticle based structures as contact mode imparts a lateral forces that either alters or destroys the structure of the nanoparticle assembly.

Dissertation Overview

Based upon the themes presented above, this thesis observes and characterizes the directed deposition of a variety of nanoparticles upon a range of substrates. Each chapter as follows is presented as separate manuscripts that address differing nanoparticles and substrates as well as deposition mechanisms. Chapter 2 begins this overall study by observing the self-assembly of polymeric nanoparticles, with their complex surface

chemistry, upon chemically segregated substrates in order to deconvolute the rules of adsorption for polymeric nanoparticles. The usage of nanoparticles to create miniaturized structures with nanometer control of the dimensions in all three dimensions is presented in Chapter 3, as well as the usage of these structures as femtoliter volume wells. This concept of utilizing the nanoparticle based structures as reaction vials, is furthered in Chapter 4 in completing bio-recognition events within individual, segregated wells. Chapter 5 then uses nanoparticles as unique identification markers in immunoassays, or bio-recognition studies, through the coupling of two different nanoparticles in hopes of creating a massively parallel, high-throughput detection platform. Finally this thesis is concluded with a summation and future prospective of the presented technologies.

References

(1) Derjaguin, B. V.; Landau, L. *Acta Physicochim. URSS* **1941**, *14*, 633-662.

(2) Verwey, E. J. W.; Overbeek, J. T. G. *Theory of the Stability of Lyophobic Colloids*; Elsevier Publishing Company, Inc.: Amsterdam, 1948.

(3) Bard, A. J.; Faulkner, L. R. *Electrochemical methods: Fundementals and applications*; Second ed.; John Wiley & Sons, Inc.: New York, 2001.

(4) Israelachvili, J. N. *Intermolecular and Surface Forces*; Second ed.; Academic Press: San Diego, 1992.

(5) Derjaguin, B. V. *Kolloid Zeits.* **1934**, *69*, 155-164.

(6) London, F. *Z. Physik* **1930**, *63*, 245-279.

(7) Hamaker, H. C. *Rec. trav. chim.* **1936**, *55*, 1015-1026.

(8) Hamaker, H. C. *Rec. trav. chim.* **1937**, *56*, 3-25.

(9) Burnham, N. A.; Colton, R. J. *Force Microscopy*; Bonnell, D. A., Ed.; VCH Publishers, Inc: New York, 1993, pp 191-250.

(10) Lifshitz, E. M. *Soviet Phys. JETP* **1956**, *2*, 73-83.

(11) Dzyaloshinskii, I. E.; Lifshitz, E. M.; Pitaevskii, L. P. *Adv. Phys.* **1961**, *10*, 165-209.

(12) Napper, D. H. *Polymeric Stabilization of Colloidal Dispersions*; Academic Press: New York, 1983.

(13) LaMer, V. K.; Dinegar, R. H. *J. Am. Chem. Soc.* **1950**, *72*, 4847-4854.

(14) Bogush, G. H.; Zukoski, C. F., IV *J. Colloid Interface Sci.* **1991**, *142*, 19-34.

(15) Bogush, G. H.; Zukoski, C. F., IV *J. Colloid Interface Sci.* **1991**, *142*, 1-18.

(16) Kim, S.; Zukoski, C. F. *J. Colloid Interface Sci.* **1990**, *139*, 198-212.

(17) Klemperer, W. G.; Ramamurthi, S. D. *J. Non-Cryst. Solids* **1990**, *121*, 16-20.

(18) Flory, P. J. *J. Am. Chem. Soc.* **1936**, *58*, 1877-1885.

(19) Stockmayer, W. H. *J. Chem. Phys.* **1943**, *11*, 45-55.

(20) Feeney, P. J.; Napper, D. H.; Gilbert, R. G. *Macromolecules* **1984**, *17*, 2520-2529.

(21) Handley, D. A. *The Development and Application of Colloidal Gold as a Microscopic Probe*; Hayat, M. A., Ed.; Academic Press, Inc.: San Diego, 1989; Vol. 1, pp 1-8.

(22) Faraday, M. *Philosophical Transactions of the Royal Society of London* **1857**, *147*, 145.

(23) Brust, M.; Walker, M.; Bethell, D.; Schiffrin, D. J.; Whyman, R. *J. Chem. Soc., Chem. Commun.* **1994**, *7*, 801-802.

(24) Lee, D.; Donkers, R. L.; DeSimone, J. M.; Murray, R. W. *J. Am. Chem. Soc.* **2003**, *125*, 1182-1183.

(25) Dolgaev, D. I.; Simakin, A. V.; Voronov, V. V.; Shafeev, G. A.; Bozon-Verduraz, F. *Appl. Surf. Sci.* **2002**, *186*, 546-551.

(26) Neddersen, J.; Chumanov, G.; Cotton, T. M. *Appl. Spectrosc.* **1993**, *47*, 1959-1964.

(27) Zhou, Y.; Wang, C. Y.; Zhu, Y. R.; Chem, Z. Y. *Chem. Mater.* **1999**, *11*, 2310-2312.

(28) Murakata, T.; Higashi, Y.; Yasui, N.; Higuchi, T.; Sato, S. *J. Chem. Eng. Japan* **2002**, *35*, 1270-1276.

(29) Penner, R. M. *J. Phys. Chem. B* **2002**, *106*, 3339-3353.

(30) Pol, V. G.; Gedanken, A.; Calderon-Moreno, J. *Chem. Mater.* **2003**, *15*, 1111-1118.

(31) Hulteen, J. C.; Treichel, D. A.; Smith, M. T.; Duval, M. L.; Jensen, T. R.; Van Duyne, R. P. *J. Phys. Chem. B* **1999**, *103*, 3854-3863.

(32) Kawakami, Y.; Seto, T.; Yoshida, T.; Ozawa, E. *Appl. Surf. Sci.* **2002**, 587-593.

(33) Andres, R. P.; Bielefeld, J. D.; Henderson, J. I.; Janes, D. B.; Kolagunta, V. R.; Kubiak, C. P.; Mahoney, W. J.; Osifchin, R. G. *Nature* **1996**, *273*, 1690-1693.

(34) Handley, D. A. *Methods for Synthesis of Colloidal Gold*; Hayat, M. A., Ed.; Academic Press, Inc.: San Diego, 1989; Vol. 1, pp 13-33.

(35) Privman, V.; Goia, D. V.; Park, J.; Matijevic, E. *Curr. Opin. Colloid Interface Sci.* **1999**, *213*, 36-45.

(36) Goia, D. V.; Matijevic', E. *Colloids Surf., A* **1999**, *146*, 139-152.

(37) Duff, D. G.; Baiker, A.; Edwards, P. P. *Langmuir* **1993**, *9*, 2301-2309.

(38) Chow, M. K.; Zukoski, C. F. *J. Colloid Interface Sci.* **1994**, *165*, 97-109.

(39) Turkevich, J.; Stevenson, P. C.; Hillier, J. *Disc. Faraday Soc.* **1951**, *11*, 55-75.

(40) Frens, G. *Nature Phys. Sci.* **1973**, *241*, 20-22.

(41) Biggs, S.; Chow, M. K.; Zukoski, C. F.; Grieser, G. *J. Colloid Interface Sci.* **1993**, *160*, 511-513.

(42) Van Hyning, D. L.; Zukoski, C. F. *Langmuir* **1998**, *14*, 7034-7046.

(43) Van Hyning, D. L.; Klemperer, W. G.; Zukoski, C. F. *Langmuir* **2001**, *17*, 3128-3135.

(44) Han, M. Y.; Quek, C. H.; Huang, W.; Chew, C. H.; Gan, L. M. *Chem. Mater.* **1999**, *11*, 1144-1147.

(45) Hostetler, M. J.; Wingate, J. E.; Zhong, C.-J.; Harris, J. E.; Vachet, R. W.; Clark, M. R.; Londono, J. D.; Green, S. J.; Stokes, J. J.; Wigall, G. D.; Glish, G. L.; Porter, M. D.; Evans, N. D.; Murray, R. W. *Langmuir* **1998**, *14*, 17-30.

(46) Brust, M.; Fink, J.; Bethell, D.; Schiffrin, D. J.; Kiely, C. *J. Chem. Soc., Chem. Commun.* **1995**, *16*, 1655-1656.

(47) Bethell, D.; Brust, M.; Schiffrin, D. J.; Kiely, C. *J. Electroanal. Chem.* **1996**, *409*, 137-143.

(48) Prasad, B. L. V.; Stoeva, S. I.; Sorensen, C. M.; Klabunde, K. J. *Chem. Mater.* **2003**, *15*, 935-942.

(49) Schaaff, T. G.; Whetten, R. L. *J. Phys. Chem. B* **1999**, *103*, 9394-9396.

(50) Iler, R. K. *The Chemistry of Silica: Solubility, Polymerization, Colloid and Surface Properties, and Biochemistry*; John Wiley & Sons: New York, 1979.

(51) Stöber, W.; Fink, A.; Bohn, E. *J. Colloid Interface Sci.* **1968**, *26*, 62-69.

(52) Kolbe, G. *Das komplexchemische Verhalten der Kieselsäure*: Jena, 1956.

(53) Lee, K.; Look, J.-L.; Harris, M. T.; McCormick, A. V. *J. Colloid Interface Sci.* **1997**, *194*, 78-88.

(54) van Blaaderen, A.; Vrij, A. *J. Colloid Interface Sci.* **1993**, *156*, 1-18.

(55) van Blaaderen, A.; Van Geest, J.; Vrij, A. *J. Colloid Interface Sci.* **1992**, *154*, 481-501.

(56) Matsoukas, T.; Gulari, E. *J. Colloid Interface Sci.* **1988**, *124*, 252-261.

(57) Matsoukas, T.; Gulari, E. *J. Colloid Interface Sci.* **1989**, *132*, 13-21.

(58) Matsoukas, T.; Gulari, E. *J. Colloid Interface Sci.* **1991**, *145*, 557-562.

(59) Harris, M. T.; Brunson, R. R.; Byers, C. H. *J. Non-Cryst. Solids* **1990**, *121*, 397-403.

(60) Boukari, H.; Lin, J. S.; Harris, M. T. *Chem. Mater.* **1997**, *9*, 2379-2384.

(61) Boukari, H.; Long, G. G.; Harris, M. T. *J. Colloid Interface Sci.* **2000**, *229*, 129-139.

(62) Green, D. L.; Jayasundara, S.; Lam, Y.-F.; Harris, M. T. *J. Non-Cryst. Solids* **2003**, *315*, 166-179.

(63) van Blaaderen, A.; Vrij, A. *Synthesis and Characterization of Colloidal Model Particles Made From Organoalkoxysilanes*; Bergna, H. E., Ed.; American Chemical Society: Washington, DC, 1994; Vol. 234, pp 83-111.

(64) Vacassy, R.; Flatt, R. J.; H. Hof, a.; Choi, K. S.; Singh, R. K. *J. Colloid Interface Sci.* **2000**, *227*, 302-315.

(65) van Blaaderen, A.; Kentgens, A. P. M. *J. Non-Cryst. Solids* **1992**, *149*, 161-178.

(66) Hohenstein, W. P.; Mark, H. *J. Polymer Sci.* **1946**, *1*, 127-145.

(67) Hohenstein, W. P.; Mark, H. *J. Polymer Sci.* **1946**, *1*, 549-580.

(68) Dinsmore, R. P.; Co.), G. T. R. *Synthetic Rubber*: USA, 1927.

(69) Talalay, A.; Magat, M. *Synthetic Rubber from Alcohol on the Basis of Russian Literature*; Interscience Publishers: New York, 1945.

(70) Luther, M.; Heuck, C.; A.-G., I. G. F. *Polymerization of Diolefins*: USA, 1932.

(71) Luther, M.; Heuck, C.; A.-G., I. G. F. *Artificial Latex-Like Products*: USA, 1932.

(72) Dunn, A. S. *Harkins, Smith-Ewart and Related Theories*; Lovell, P. A. and El-Aasser, M. S., Ed.; John Wiley and Sons: New York, 1997, pp 125-164.

(73) Carraher, C. E., Jr. *Syemour / Carraher's Polymer Chemistry: An Introduction*; Fourth ed.; Marcel Dekker, Inc.: New York, 1996.

(74) Odian, G. *Emulsion Polymerization*; Third ed.; John Wiley & Sons, Inc.: New York, 1991, pp 335-355.

(75) Daniels, E. S.; Sudol, E. D.; El-Aasser, M. S. *Overview of Polymer Colloids: Preparation, Characterization, and Applications*; Daniels, E. S., Sudol, E. D. and El-Aasser, M. S., Ed.; American Chemical Society: Washington, D.C., 2002; Vol. 801.

(76) El-Aasser, M. S.; Sudol, E. D. *Features of Emulsion Polymerization*; Lovell, P. A. and El-Aasser, M. S., Ed.; John Wiley and Sons: New York, 1997, pp 37-58.

(77) Harkins, W. D. *J. Am. Chem. Soc.* **1947**, *69*, 1428-1444.

(78) Dunn, A. S. *Effects of the Choice of Emulsifier in Emulsion Polymerization*; Piirma, I., Ed.; Academic Press, Inc.: New York, 1982, pp 221-245.

(79) Blackley, D. C. *Emulsion Polymerization: Theory and Practice*; John Wiley and Sons: New York, 1975.

(80) Hansen, F. K.; Ugelstad, J. *J. Polym. Sci., Polym. Chem. Ed.* **1978**, *16*, 1953-1979.

(81) Hansen, F. K.; Ugelstad, J. *Particle Formation Mechanisms*; Piirma, I., Ed.; Academic Press, Inc.: New York, 1982, pp 51-93.

(82) Fitch, R. M.; Tsai, C. H. *Particle Formation in Polymer Colloids. III. Prediction of the Number of Particles by a Homogeneous Nucleation Theory*; Fitch, R. M., Ed.; Plenum Press: New York, 1971, pp 73-102.

(83) Fitch, R. M.; Prenosil, M. B.; Sprick, K. J. *J. Polymer Sci.* **1966**, 95-118.

(84) Vandezande, G. A.; Rudin, A. *Production of Vinyl Acetate-Butyl Acrylate Copolymer Latexes of Narrow Particle Size Distributions*; Daniels, E. S., Sudol, E. D. and El-Aasser, M. S., Ed.; American Chemical Society: Washington, D.C., 192; Vol. 492, pp 114-133.

(85) Molday, R. S.; Dreyer, W. J.; Rembaum, A.; Yen, S. P. S. *J. Cell Biol.* **1975**, *64*, 75-88.

(86) Bangs, L. B. *Pure Appl. Chem.* **1996**, *68*, 1873-1879.

(87) Pris, A. D.; Porter, M. D. *Nano Lett.* **2002**, *2*, 1087-1091.

(88) Mayoral, R.; Requena, J.; Moya, J. S.; López, C.; Cintas, A.; Míguez, H.; Meseguer, F.; Vázquez, L.; Holgado, M.; Blanco, Á. *Adv. Mater.* **1997**, *9*, 257-260.

(89) Salvarezza, R. C.; Vázquez, L.; Míguez, H.; Mayoral, R.; López, C.; Meseguer, F. *Phys. Rev. Lett.* **1996**, *77*, 4572-4575.

(90) Míguez, H.; Meseguer, F.; López, C.; Mifsud, A.; Moya, J. S.; Vázquez, L. *Langmuir* **1997**, *13*, 6009-6011.

(91) Perrin, J. *Ann. Chim. Phys.* **1909**, *18*, 1.

(92) Kralchevsky, P. A.; Nagayama, K. *Particles at Fluids Interfaces and Membranes: Attachment of colloid particles and proteins to interfaces and formation of two-dimensional arrays*; Elsevier: Amsterdam, 2001; Vol. 10.

(93) Denkov, N. D.; Velev, O. D.; Kralchevsky, P. A.; Ivanov, I. B.; Yoshimura, H.; Nagayama, K. *Langmuir* **1992**, *8*, 3183-3190.

(94) Lazarov, G. S.; Denkov, N. D.; Velev, O. D.; Kralchevsky, P. A.; Nagayama, K. *J. Chem. Soc. Faraday Trans.* **1994**, *90*, 2077-2083.

(95) Kralchevsky, P. A.; Nagayama, K. *Langmuir* **1994**, *10*, 23-36.

(96) Dimitrov, A. S.; Dushkin, C. D.; Yoshimura, H.; Nagayama, K. *Langmuir* **1994**, *10*, 432-440.

(97) Dimitrov, A. S.; Nagayama, K. *Langmuir* **1996**, *12*, 1303-1311.

(98) Dushkin, C. D.; Lazarov, G. S.; Kotsev, S. N.; Yoshimura, H.; Nagayama, K. *Colloid Polym. Sci.* **1999**, *277*, 914-930.

(99) Maenosono, S.; Dushkin, C. D.; Yamaguchi, Y.; Nagayama, K.; Tsuji, Y. *Colloid Polym. Sci.* **1999**, *277*, 1152-1161.

(100) Thill, A.; Spalla, O. *Langmuir* **2002**, *18*, 4783-4789.

(101) Dimitrov, A. S.; Nagayama, K. *Chem. Phys. Lett.* **1995**, *243*, 462-468.

(102) Micheletto, R.; Fukuda, H.; Ohtsu, M. *Langmuir* **1995**, *11*, 3333-3336.

(103) Deckman, H. W.; Dunsmuir, J. H. *Appl. Phys. Lett.* **1982**, *41*, 377-379.

(104) Deckman, H. W.; Dunsmuir, J. H. *J. Vac. Sci. Technol., B* **1983**, *1*, 1109-1112.

(105) Jiang, P.; Ostojic, G. N.; Narat, R.; Mittleman, D. M.; Colvin, V. L. *Adv. Mater.* **2001**, *13*, 389-393.

(106) Jiang, P.; Bertone, J. F.; Hwang, K. S.; Colvin, V. L. *Chem. Mater.* **1999**, *11*, 2132-2140.

(107) Trau, M.; Saville, D. A.; Aksay, I. A. *Science* **1996**, *272*, 706-709.

(108) Trau, M.; Saville, D. A.; Aksay, I. A. *Langmuir* **1997**, *13*, 6375-6381.

(109) Böhmer, M. *Langmuir* **1996**, *12*, 5747-5750.

(110) Solomentsev, Y.; Böhmer, M.; Anderson, J. L. *Langmuir* **1997**, *13*, 6058-6068.

(111) Gong, T.; Marr, D. W. M. *Langmuir* **2001**, *17*, 2301-2304.

(112) Hayward, R. C.; Saville, D. A.; Aksay, I. A. *Nature* **2000**, *404*, 56-59.

(113) Holgado, M.; García-Santamaría, F.; Blanco, A.; Ibisate, M.; Cintas, A.; Míguez, H.; Serna, C. J.; Molpeceres, C.; Requena, J.; Mifsud, A.; Meseguer, F.; López, C. *Langmuir* **1999**, *15*, 4701-4704.

(114) Kumacheva, E.; Golding, R. K.; Allard, M.; Sargent, E. H. *Adv. Mater.* **2002**, *14*, 221-224.

(115) Richetti, P.; Prost, J.; Barois, P. *J. Phys. Lett.* **1984**, *45*, 1137-1143.

(116) van Blaaderen, A.; Ruel, R.; Wiltzius, P. *Nature* **1997**, *385*, 321-324.

(117) van Blaaderen, A.; Wiltzius, P. *Adv. Mater.* **1997**, *9*, 833-835.

(118) Hoogenboom, J. P.; Vossen, D. L. J.; Faivre-Moskalenko, C.; Dogterom, M.; van Blaaderen, A. *Appl. Phys. Lett.* **2002**, *80*, 4828-4830.

(119) Yin, Y.; Li, Z.-Y.; Xia, Y. *Langmuir* **2003**, *19*, 622-631.

(120) Lin, K.-h.; Crocker, J. C.; Prasad, V.; Schofield, A.; Weitz, D. A.; Lubensky, T. C.; Yodh, A. G. *Phys. Rev. Lett.* **2000**, *85*, 1770-1773.

(121) Dinsmore, A. D.; Yodh, A. G. *Langmuir* **1999**, *15*, 314-316.

(122) Teranishi, T.; Sugawara, A.; Shimizu, T.; Miyake, M. *J. Am. Chem. Soc.* **2002**, *124*, 4210-4211.

(123) Yang, S. M.; Ozin, G. A. *Chem. Commun.* **2000**, *2000*, 2507-2508.

(124) Ozin, G. A.; Yang, S. M. *Adv. Funct. Mater.* **2001**, *11*, 95-104.

(125) Míguez, H.; Yang, S. M.; Ozin, G. A. *Langmuir* **2003**, *19*, 3479-3485.

(126) Wolter, O.; Bayer, T.; Greschner, J. *J. Vac. Sci. Technol., B* **1991**, *9*, 1353-1357.

(127) Yin, Y.; Xia, Y. *Adv. Mater.* **2002**, *14*, 605-608.

(128) Park, S. H.; Qin, D.; Xia, Y. *Adv. Mater.* **1998**, *10*, 1028-1032.

(129) Yin, Y.; Lu, Y.; Gates, B.; Xia, Y. *J. Am. Chem. Soc.* **2001**, *123*, 8718-8729.

(130) Yin, Y.; Xia, Y. *J. Am. Chem. Soc.* **2003**, *125*, 2048-2049.

(131) Jackman, R. J.; Duffy, D. C.; Ostuni, E.; Willmore, N. D.; Whitesides, G. M. *Anal. Chem.* **1998**, *70*, 2280-2287.

(132) Kim, E.; Xia, Y.; Whitesides, G. M. *J. Am. Chem. Soc.* **1996**, *118*, 5722-5731.

(133) Kim, E.; Xia, Y.; Zhao, X.-M.; Whitesides, G. M. *Adv. Mater.* **1997**, *9*, 651-654.

(134) Bizdoaca, E. L.; Spasova, M.; Farle, M.; Hilgendorff, M.; Caruso, F. *J. Magn. Magn. Mater.* **2002**, *240*, 44-46.

(135) Giersig, M.; Hilgendorff, M. *J. Phys. D: Appl. Phys.* **1999**, *32*, L111-L113.

(136) Hilgendorff, M.; Tesche, B.; Giersig, M. *Aust. J. Chem.* **2001**, *54*, 497-501.

(137) Jang, I. J.; Horng, H. E.; Chiou, Y. C.; Hong, C.-Y.; Wu, J. M.; Yang, H. C. *J. Magn. Magn. Mater.* **1999**, *201*, 317-320.

(138) Petit, C.; Legrand, J.; Russier, V.; Pileni, M. P. *J. Appl. Phys.* **2002**, *91*, 1502-1508.

(139) Nawa, M.; Baba, R.; Nakabayashi, S.; Dushkin, C. *Nano Lett.* **2003**, *3*, 293-297.

(140) Grzybowski, B. A.; Whitesides, G. M. *J. Phys. Chem. B* **2001**, *105*, 8770-8775.

(141) Fudouzi, H.; Kobayashi, M.; Shinya, N. *Adv. Mater.* **2002**, *14*, 1649-1652.

(142) Fudouzi, H.; Kobayashi, M.; Shinya, N. *Langmuir* **2002**, *18*, 7648-7652.

(143) Jacobs, H. O.; Campbell, S. A.; Steward, M. G. *Adv. Mater.* **2002**, *14*, 1553-1557.

(144) Mesquida, P.; Stemmer, A. *Adv. Mater.* **2001**, *13*, 1395-1398.

(145) Ali, M. B.; Ondarçuhu, T.; Brust, M.; Joachim, C. *Langmuir* **2002**, *18*, 872-876.

(146) Brandow, S. L.; Dressick, W. J.; Dulcey, C. S.; Koloski, T. S.; Shirey, L. M.; Schmidt, J.; Calvert, J. M. *J. Vac. Sci. Technol., B* **1997**, *15*, 1818-1824.

(147) Junno, T.; Carlsson, S.-B.; Xu, H.; Montelius, L.; Samuelson, L. *Appl. Phys. Lett.* **1998**, *72*, 548-550.

(148) Liu, X.; Fu, L.; Hong, S.; Dravid, V. P.; Mirkin, C. A. *Adv. Mater.* **2002**, *14*, 231-234.

(149) Martin, M.; Roschier, L.; Hakonen, P.; Parts, Ü.; Paalanen, M.; Schleicher, B.; Kauppinen, E. I. *Appl. Phys. Lett.* **1998**, *73*, 1505-1507.

(150) Resch, R.; Baur, C.; Bugacov, A.; Koel, B. E.; Madhukar, A.; Requicha, A. A. G.; Will, P. *Langmuir* **1998**, *14*, 6613-6616.

(151) Resch, R.; Bugacov, A.; Baur, C.; Koel, B. E.; Madhukar, A.; Requicha, A. A. G.; Will, P. *Appl. Phys. A* **1998**, *67*, 265-271.

(152) Resch, R.; Baur, C.; Bugacov, A.; Koel, B. E.; Echternach, P. M.; Madhukar, A.; Montoya, N.; Requicha, A. A. G.; Will, P. *J. Phys. Chem. B* **1999**, *103*, 3647-3650.

(153) Ritter, C.; Heyde, M.; Schwarz, U. D.; Rademann, K. *Langmuir* **2002**, *18*, 7798-7803.

(154) Yamamoto, K.; Tanuma, C.; Gemma, N. *J. Phys. Chem* **1996**, *100*, 8369-8372.

(155) Ulman, A. *Chem. Rev.* **1996**, *96*, 1533-1554.

(156) Nuzzo, R. G.; Allara, D. L. *J. Am. Chem. Soc.* **1983**, *105*, 4481-4483.

(157) Li, T. T. T.; Weaver, M. J. *J. Am. Chem. Soc.* **1984**, *106*, 6107-6108.

(158) Porter, M. D.; Bright, T. B.; Allara, D. L.; Chidsey, C. E. D. *J. Am. Chem. Soc.* **1987**, *109*, 3559-3568.

(159) Troughton, E. B.; Bain, C. D.; Whitesides, G. M.; Nuzzo, R. G.; Allara, D. L.; Porter, M. D. *Langmuir* **1988**, *4*, 365-385.

(160) Müller, W. T.; Klein, D. L.; Lee, T.; Clarke, J.; McEuen, P. L.; Schultz, P. G. *Science* **1995**, *268*, 272-273.

(161) Lua, Y.-Y.; Niederhauser, T. L.; Wacaser, B. A.; Mowat, I. A.; Woolley, A. T.; Davies, R. C.; Fishman, H. A.; Linford, M. R. *Langmuir* **2003**, *19*, 985-988.

(162) Wang, J.; Kenseth, J. R.; Jones, V. W.; Green, J.-B. D.; McDermott, M. T.; Porter, M. D. *J. Am. Chem. Soc.* **1997**, *119*, 12796-12799.

(163) Liu, S.; Maoz, R.; Schmid, G.; Sagiv, J. *Nano Lett.* **2002**, *2*, 1055-1060.

(164) Zamborini, F. P.; Crooks, R. M. *J. Am. Chem. Soc.* **1998**, *120*, 9700-9701.

(165) Sugimura, H.; Nakagiri, N. *J. Am. Chem. Soc.* **1997**, *119*, 9226-9229.

(166) Zheng, J.; Zhu, Z.; Chen, H.; Liu, Z. *Langmuir* **2000**, *16*, 4409-4412.

(167) Li, Q.; Zheng, J.; Liu, Z. *Langmuir* **2003**, *19*, 166-171.

(168) Masuda, Y.; Seo, W. S.; Koumoto, K. *Jpn. J. Appl. Phys.* **2000**, *39*, 4596-6000.

(169) Amro, N. A.; Xu, S.; Liu, G.-y. *Langmuir* **2000**, *16*, 3006-3009.

(170) Xu, S.; Miller, S.; Laibinis, P. E.; Liu, G.-y. *Langmuir* **1999**, *15*, 7244-7251.

(171) Xu, S.; Liu, G.-y. *Langmuir* **1997**, *13*, 127-129.

(172) Liu, J.-F.; Cruchon-Dupeyrat, S.; Garno, J. C.; Frommer, J.; Liu, G.-Y. *Nano Lett.* **2002**, *2*, 937-940.

(173) Kenseth, J. R.; Harnisch, J. A.; Jones, V. W.; Porter, M. D. *Langmuir* **2001**, *17*, 4105-4112.

(174) Vettiger, P.; Despont, M.; Drechsler, U.; Durig, U.; Haberle, W.; Lutwyche, M. I.; Rothuizen, H. E.; Stutz, R.; Widmer, R.; Binning, G. K. *IBM J. Res. Develop.* **2000**, *44*, 323-340.

(175) Kumar, A.; Biebuyck, H. A.; Whitesides, G. M. *Langmuir* **1994**, *10*, 1498-1511.

(176) Kumar, A.; Whitesides, G. M. *Appl. Phys. Lett.* **1993**, *63*, 2002-2004.

(177) Tien, J.; Terfort, A.; Whitesides, G. M. *Langmuir* **1997**, *13*, 5349-5355.

(178) Maye, M. M.; Luo, J.; Han, L.; Zhong, C.-J. *Nano Lett.* **2001**, *1*, 575-579.

(179) Aizenberg, J.; Braun, P. V.; Wilzius, P. *Phys. Rev. Lett.* **2000**, *84*, 2997-3000.

(180) Chen, K. M.; Jiang, X.; Kimerling, L. C.; Hammond, P. T. *Langmuir* **2000**, *16*, 7825-4834.

(181) Hickman, J. J.; Bhatia, S. K.; Quong, J. N.; Shoen, P.; Stenger, D. A.; Pike, C. J.; Cotman, C. W. *J. Vac. Sci. Technol., A* **1994**, *12*, 607-616.

(182) Mooney, J. F.; Hunt, A. J.; McIntosh, J. R.; Liberko, C. A.; Walba, D. M.; Rogers, C. T. *Proc. Natl. Acad. Sci. U. S. A.* **1996**, *93*, 12287-12291.

(183) Lercel, M. J.; Tiberio, R. C.; Chapman, P. F.; Craighead, H. G.; Sheen, C. W.; Parikh, A. N.; Allara, D. L. *J. Vac. Sci. Technol., B* **1993**, *11*, 2823-2828.

(184) Huang, J.; Hemminger, J. C. *J. Am. Chem. Soc.* **1993**, *115*, 3342-3343.

(185) Tarlov, M. J.; Burgess, D. R. F., Jr.; Gillen, G. *J. Am. Chem. Soc.* **1993**, *115*.

(186) Lewis, M.; Tarlov, M.; Carron, K. *J. Am. Chem. Soc.* **1995**, *117*, 9574-9575.

(187) Zhang, Y.; Terrill, R. H.; Tanzer, T. A.; Bohn, P. W. *J. Am. Chem. Soc.* **1998**, *120*, 2654-2655.

(188) Norrod, K. L.; Rowlen, K. L. *J. Am. Chem. Soc.* **1998**, *120*, 2656-2657.

(189) Friebel, S.; Aizenberg, J.; Abad, S.; Wilzius, P. *Appl. Phys. Lett.* **2000**, *77*, 2406-2408.

(190) Masuda, Y.; Seo, W. S.; Koumoto, K. *Thin Solid Films* **2001**, *382*, 183-189.

(191) Sato, T.; Hasko, D. G.; Ahmed, H. *J. Vac. Sci. Technol., B* **1997**, *15*, 45-48.

(192) Ingle, J. D., Jr.; Crouch, S. R. *Spectrochemical Analysis*; Prentice Hall: Englewood Cliffs, 1988.

(193) Goldstein, J. I.; Romig, A. D., Jr.; Newbury, D. E.; Lyman, C. E.; Echlin, P.; Fiori, C.; Joy, D. C.; Lifshin, E. *Scanning Electron Microscopy and X-Ray Microanalysis:*

A Text for Biologists, Material Scientists, and Geologists; Second ed.; Plenum Press: New York, 1992.

(194) Takano, H.; Kenseth, J. R.; Wong, S.-S.; O'Brien, J. C.; Porter, M. D. *Chem. Rev.* **1999**, *99*, 2845-2890.

(195) Bonnell, D. A. *Scanning Tunneling Microscopy and Spectroscopy: Theory, Techniques, and Applications*; VCH Publishers, Inc.: New York, 1993, pp 436.

(196) Colton, R. J.; Engel, A.; Frommer, J. E.; Gaub, H. E.; Gewirth, A. A.; Guckenberger, R.; Rabe, J.; Heckl, W. M.; Parkinson, B. *Procedures in Scanning Probe Microscopies*; John Wiley & Sons: New York, 1998, pp 639.

(197) Lillehei, P. T.; Bottomley, L. A. *Anal. Chem.* **2000**, *72*, 189R-196R.

(198) Binning, G.; Rohrer, H.; Gerger, C.; Weibel, E. *Phys. Rev. Lett.* **1982**, *49*, 57-61.

(199) Skoog, D. A.; Holler, F. J.; Nieman, T. A. *Principles of Instrumental Analysis*; Fifth ed.; Saunders College Publishing: Philadelphia, 1998.

(200) Binning, G.; Quate, C. F.; Gerber, C. *Phys. Rev. Lett.* **1986**, *56*, 930-933.

(201) Israelachvili, J. N. *Surface Forces*; Hubbard, A. T., Ed.; CRC Press, Inc.: Boca Raton, 1995, pp 793-816.

(202) Albrecht, T. R.; Quate, C. F. *J. Vac. Sci. Technol., A* **1988**, *6*, 271-274.

(203) Albrecht, T. R.; Akamine, S.; Carver, T. E.; Quate, C. F. *J. Vac. Sci. Technol., A* **1990**, *8*, 3386-3396.

(204) Ducker, W. A.; Senden, T. J.; Pashley, R. M. *Langmuir* **1992**, *8*, 1831-1836.

(205) Dai, H.; Hafner, J. H.; Rinzler, A. G.; Colbert, D. T.; Smalley, R. E. *Nature* **1996**, *384*, 147-150.

(206) Wong, S. S.; Harper, J. D.; Lansbury, P. T., Jr.; Lieber, C. M. *J. Am. Chem. Soc.* **1998**, *120*, 603-604.

(207) Wong, S. S.; Joselevich, E.; Woolley, A. T.; Cheung, C. L.; Lieber, C. M. *Nature* **1998**, *394*, 52-55.

(208) Thaysen, J.; Boisen, A.; Hansen, O.; Bouwstra, S. *Sens. Actuators, A* **2000**, *83*, 47-53.

(209) Erlandsson, R.; McClelland, G. M.; Mate, C. M.; Chiang, S. *J. Vac. Sci. Technol., A* **1988**, *6*, 266-270.

(210) Meyer, G.; Amer, N. M. *Appl. Phys. Lett.* **1988**, *53*, 2400-2402.

(211) Amrein, M. *Common Techniques and Problems in Scanning Probe Microscopies*; Colton, R. J., Engel, A., Frommer, J. E., Gaub, H. E., Gewirth, A. A., Guckenberger, R., Rabe, J., Heckl, W. M. and Parkinson, B., Ed.; John Wiley & Sons: New York, 1998, pp 3-49.

(212) Norman, C. J. *Zirconium Oxide Products in Automotive Systems*, 1997; Vol. 2002.

(213) Newnham, R. E.; Amin, A. *Chemtech* **1999**, *29*, 36-46.

(214) Jaffe, B.; Cook, W. R., Jr.; Jaffe, H. *Piezoelectric Ceramics*; R. A. N. Publishers: Marietta, OH, 1971.

(215) , D. I. *Calibration Procedures, Troubleshooting and Maintenance*: Santa Barbara, CA, 1999.

(216) Green, J.-B. D.; McDermott, M. T.; Porter, M. D.; Siperko, L. M. *J. Phys. Chem* **1995**, *99*, 10960-10965.

(217) Overney, R. M. *Nature* **1992**, *359*, 133-134.

(218) Noy, A.; Frisbie, C. D.; Rozsnyai, L. F.; Wrighton, M. S.; Lieber, C. M. *J. Am. Chem. Soc.* **1995**, *117*, 7943-7951.

(219) Frisbie, C. D.; Rozsnyai, L. F.; Noy, A.; Wrighton, M. S.; Lieber, C. M. *Science* **1994**, *265*, 2071-2074.

(220) Tsukruk, V. V.; Sidorenko, A.; Gorunov, V. V.; Chizhik, S. A. *Langmuir* **2001**, *17*, 6715-6719.

(221) Zhong, Q.; Inniss, D.; Kjoller, K.; Elings, V. B. *Surface Science Letters* **1993**, *290*, L688-L692.

(222) Tamayo, J.; García, R. *Langmuir* **1996**, *12*, 4430-4435.

(223) García, R.; Pérez, R. *Surf. Sci. Rep.* **2002**, *47*, 197-301.

(224) Edwards, G. A., Personal Communication.

CHAPTER 1: FABRICATION OF TWO-DIMENSIONAL MICROSTRUCTURES THROUGH THE SELF-ORGANIZATION OF POLYMERIC NANOPARTICLES ON COMPOSITIONALLY PATTERNED THIOLATE MONOLAYERS

Andrew D. Pris[1], Jennifer H. Granger[2], Jeremy R. Kenseth[3], and Marc D. Porter[1,4]

Abstract

This paper examines issues related to the patterning of polymeric colloidal nanoparticles through their self-assembly on compositionally patterned substrates for the fabrication of microstructures on a surface. Using several well-developed techniques, the surface chemistry of gold substrates has been compositionally tailored with thiols to create hydrophilic/hydrophobic patterns. Polymeric nanoparticles were then self-assembled on the hydrophilic monolayer regions of the hydrophilic/hydrophobic pattern. Several different types of polymeric nanoparticles and hydrophilic test monolayers were judiciously chosen and the subsequent patterns analyzed with atomic force microscopy (AFM). The results garnered from the AFM images of various combinations of monolayer pattern / nanoparticle composition were used to describe the interactions of importance to an adsorption-based polymeric nanoparticle deposition.

[1] Microanalytical Instrumentation Center, Ames Laboratory-USDOE, and Department of Chemistry, Iowa State University, Ames, IA 50011
[2] Waters Corporation, 34 Maple Street, Milford, MA 01757-3696
[3] Combisep, Inc., 2711 South Loop Drive, Suite 4200, Ames, IA 50010
[4] Corresponding Author

Introduction

The ability to manipulate the size, shape, and assembly of nanometeric objects is an active pursuit across numerous fronts. This broad level of interest is driven by: 1) the intrigue in the unique phenomena arising at this length scale (e.g., quantum dots,[1,2] photonic bandgap crystals,[3,4] nanoelectrode ensembles,[5] and catalysts[6]) and 2) the use of such materials as building blocks for the construction of miniaturized platforms for a variety of lab-on-a-chip and related microelectromechanical system (MEMS) applications.[7-11] In many instances, the creation of these structures is directed by capillary forces (i.e., natural lithography),[12-24] electric field gradients,[25-29] and/or combinations of chemical interactions with an underlying substrate.[30-50] Chemical interactions arguably offer the greatest flexibility in controlling the self-assembly of such architectures.

Our interest in this area rests with the use of polymeric nanoparticles in an electrostatic driven layer-by-layer protocol for the creation of structures with sub-micrometer dimensions (e.g., arrays of femtoliter volume well plates).[11] This protocol is based on the ability to deposit alternating layers of oppositely charged polymeric nanoparticles on a substrate until reaching the target number of layers, which defines the height of the structure (i.e., the well depth). The lateral dimensions of the structure are then defined via photolithographic masking and UV photo-degradation. With this facile procedure, structures with nanometer heights and micrometer lateral dimensions can be created to yield a massively dense array of ultrasmall volume reaction wells. Furthermore, these structures can be prepared from materials that have the robustness required for many types of miniaturized analytical platforms.

In order to investigate an alternate means to create the lateral patterns of nanoparticles upon a surface, studies regarding the adsorption of polymeric nanoparticles on thiol self-assembled monolayers (SAMs) on gold were pursued. SAMs on gold provide several desirable attributes such as being well understood,[51-54] available with a variety of terminal functional groups, and can be patterned upon the surface.[55-63] These characteristics of SAMs can be exploited to provide patterns of chemically distinct areas upon a gold substrate.

It is possible to use these compositionally varied lateral surface patterns to direct the adsorption of colloidal particles onto one portion of the surface and not the other. Several methodologies have been present in the literature in which gold,[33,47,64-68] silica,[69,70] or polymeric particles[45,50,71-73] have been spatially localized on a variety of compositionally patterned monolayers based upon electrostatic interactions, hydrophobicity, capillary forces, and van der Waals interactions. In the beginning, we theorized that this concept could be used to form a polymeric nanoparticle pattern by acting as a template for the layer-by-layer growth, nanoparticle-based architectures. However, the paramount motive to begin this study was to obtain an increased knowledge of the lateral patterning concept. Therefore, an important parameter to understand in this patterned monolayer / nanoparticle adsorption concept is the interplay between the patterned monolayer and nanoparticle surface chemistry.

The surface chemistry presented by the monolayer is easily controlled through choice of a terminal functional group. The surface chemistry of the nanoparticle, on the other hand, presents a much more complex scenario. In the examples presented above, colloidal particles with simple surface chemistry (i.e., gold, silica, micron-sized polymeric particles) were used. We, however, desire to exploit nanometer-sized polymeric particles that inherently have a

complex surface chemistry. This complex surface chemistry, as illustrated in Figure 1, stems from many factors including latent surfactant (i.e., sodium dodecyl sulfate), charged polymerization initiator moieties (i.e., potassium persulfate), and covalently bound charged functional groups (i.e., amines, carboxylates, sulfates). These charged groups are critical in maintaining the polymeric nanoparticles as a dispersion, as the dispersion will otherwise undergo flocculation due to attractive hydrophobic and van der Waals forces as predicted by the DLVO theory.[74-76] Due to the desire to both use polymeric nanoparticles with their complex surface chemistry and gain an understanding of the adsorption mechanism upon patterned monolayers, we have judiciously chosen several different monolayer functional groups and polymeric nanoparticles with varying functional groups and quantities of surfactant. The degree to which a particular nanoparticle, with its associated surface chemistry (i.e., functional groups, presence of surfactant), adsorbed upon a monolayer pattern with a defined terminal groups was observed and a general adsorption theory for the nanoparticles and monolayers used in this study is presented.

Experimental Section

Reagents and Materials

Octadecanethiol (ODT), 11-mercapto-1-undecanol (ROH), 16-mercaptohexadecanoic acid (RCOOH), 2-aminoethane thiol (RNH_2), and 4-nitrothiophenol ($ArNO_2$) were purchased from Aldrich (Milwaukee) and used as received. The sulfonate-terminated thiol, 11-mercaptodecane-1-sulfonate (RSO_3^-), was synthesized using standard literature procedures.[77] Perchloric acid was obtained from Fisher and was used as received. Aqueous dispersions

(10% (w/w), pH~5.5) of polystyrene (PS, 80-nm, ~$3.3*10^{14}$ particles/mL), poly(methyl methacrylate) (PMMA, 80-nm, ~$3.9*10^{14}$ particles/mL), carboxylate-modified polystyrene (carb-PS, 90-nm, ~$2.4*10^{13}$ particles/mL), and surfactant-free polystyrene (sf-PS, 100-nm, ~$2.1*10^{14}$ particles/mL) nanoparticles were purchased from Bangs Laboratories and used as received.

Gold Substrate Fabrication

Gold substrates were prepared by cleaving a silicon wafer ((100) single crystal, Montco Silicon) into 10 x 10 mm chips. The chips were cleaned sequentially in an ultrasonic bath for 30 min in deionized water (Millipore, 18 MΩ) and 30 min in methanol (Fisher). Upon completion of the second sonication step, the chips were dried with nitrogen (Air Products), placed in a vacuum evaporator (Edwards High Vacuum Products), and coated with 15 nm of chromium at 0.1 nm/s which was followed by 300 nm of gold (99.9% purity) at 0.2-0.3 nm/s. Throughout the coating procedure, the pressure in the deposition chamber was ~8×10^{-6} Torr. The substrates were then removed from the evaporator and either used immediately or stored in a desiccator. Prior to use, the stored substrates were vigorously rinsed in extensive amounts of ethanol (Quantum, punctilious grade).

Monolayer Pattern Formation

Compositionally patterned monolayers were created following the general guidelines established within the literature for thiolate monolayer photopatterning.[55,78,79] Briefly, a gold substrate was placed into a 1 mM thiol solution for 24 h. Ethanol was used as the

solvent except in the case for 11-mercaptodecane-1-sulfonate which was dissolved in 0.1 M $HClO_4$. A copper or nickel transmission electron microscopy (TEM) grid (2000 mesh, hole size: 7.5-μm, bar size: 5.0-μm) was then carefully sandwiched between the monolayer-coated sample and a quartz plate. The masked sample was irradiated for 20 min with a 200 W, medium-pressure mercury lamp (Oriel), which was reflected off an air-cooled dichroic mirror (220-260 nm) and focused by a fused-silica lens. Reports have shown that this technique converts the gold-bound thiolates in the irradiated regions to various forms of oxygenated sulfur (e.g., SO_3^-) that are easily rinsed from the surface with most organic solvents.[55-58] After irradiation, the sample was removed from the mask assembly and vigorously rinsed with ethanol. The sample was then placed into a second 1 mM thiol solution, again for 24 h. Next, the sample was vigorously rinsed with ethanol and dried under a directed stream of high purity nitrogen. This procedure results in a compositionally patterned surface coating in which the chemical groups in the grid region are defined by the first monolayer deposited, and those in the square regions are determined by the deposited thiol after photolithographic processing.

Contact Angle Measurements

The wettability of the different monolayer coatings was characterized/verified by static contact angle measurements that used water as the probe liquid. A 10-μL drop of de-ionized water was placed on five different locations of the sample and the static contact angle recorded. The values shown in Table 1 are the average of the five measurements. The results show, in accordance with numerous literature findings,[51,77,80,81,82,83] that the coated

substrates span a wide range of surface free energies. The ODT rests at the low surface free energy end of this spectrum, where as the high hydrophilicity end of the spectrum is represented by the RCOOH and RSO_3^- coatings.

Polymeric Nanoparticle Deposition

Prior to particle deposition, the compositionally patterned sample was mounted on a sheet of Parafilm® that was stretched across a glass plate. A small volume (20 μL) of the polymeric nanoparticle dispersion of interest was pipetted onto the patterned sample. The sample was then enclosed in a humid environment which was built by placing several drops of de-ionized water on the Parafilm® sheet around the sample and then pressing a plastic Petri dish into the Parafilm® around the sample and water. The sample is then incubated in this sealed humidity chamber at room temperature for 24 h. After this incubation, the sample was vigorously rinsed sequentially with de-ionized water and ethanol and then dried with high purity nitrogen.

Atomic Force Microscopy

A MultiMode NanoScope IIIa SFM (Digital Instruments), equipped with a 150-μm tube scanner, was operated under ambient conditions. The system was used in both tapping and contact mode to investigate different material properties. All polymeric nanoparticle patterns were first interrogated in tapping mode at 1 Hz by employing a 124-μm TESP silicon probes (Nanosensors) with a force constant between 38.5 and 72.4 N/m. The resonance frequencies of the cantilevers were between 298 and 365 kHz. The cantilever

oscillation amplitude setpoint was controlled at 80% of the free oscillation amplitude and was maintained through the electronic-mechanical feedback loop of the instrument providing a $F_N \sim 10^{-9}$N. All contact mode measurements were made with 200-μm oxide-sharpened Si_3N_4 cantilevers (Nanoprobes), with normal bending and torsional force constants of ~0.06 and ~80 N/m, respectively.

Results and Discussion

Altered System Components

The goal of this study is deduce of a set of tenets that will assist in determining the optimal substrate surface group (i.e., monolayer) to use when patterning a particular type of nanoparticle with a given surface charge and surfactant concentration. It has been shown in previous reports that the chemical functional groups present in the monolayer pattern[33,45,47,50,64-73] as well as on the particle surface and solution components (i.e., pH,[67,69,84,85] ionic strength,[44,69] surfactant[69,73,86]) affect the adsorption of particle upon surfaces. Therefore, the experimental materials were chosen to provide a means to systematically alter these three major system components (monolayer functionality, particle surface chemistry, surfactant concentration) and observe their effects on creating a controlled nanoparticle pattern.

Monolayer Templates. Several SAMs with chemically distinct terminal groups were patterned on a gold surface against a monolayer of octadecanethiol (ODT) to investigate the adsorption mechanism for polymeric nanoparticles. The chemically distinct

thiols were chosen so as to attain a range of electrostatics, hydrophobicity, organization on the surface, and other van der Waals interactions. For reference purposes, Table 1 summarizes the surface pK_a and the static contact angle of water on these test monolayers, with the decrease in contact angles corresponding to an increase in surface free energy. Since ODT is a well-characterized coating, and has been shown to preferentially resist the adsorption of several types of materials, it was used as an internal reference for comparing the effects of the different terminal groups on polymeric nanoparticle adsorption.[51,53,65,78]

Nanoparticle Surface Chemistry and Surfactant Concentration. To probe the effects of nanoparticle surface chemistry and surfactant concentrations on the adsorption of polymeric nanoparticles to the various compositionally patterned surfaces, four types of nanoparticle dispersions were utilized: PS, PMMA, carb-PS, sf-PS (Table 1). Each of these dispersions presents different permutations of surface and solution components. These polymeric nanoparticles were created through emulsion polymerization and all posses a unique and complex surface chemistry central to forming a stable dispersion in solution through electrostatic repulsion.[74-76,87] Each of the dispersions employed in this study draw their stability from various sources of electrostatic charge. The PS nanoparticle dispersion, Figure 1A, draws some stability from residual charged sulfate initiator groups, but mostly from latent surfactant[88] that is adsorbed to the particles surface from the dispersing matrix. If too little surfactant is present, the dispersion will flocculate.

In order to obtain stable dispersions with decreased amounts of surfactant present both upon the particle surface and in solution, increased covalently bound charged functional

groups must be added to the nanoparticle surface. This is the case with the carb-PS and PMMA nanoparticles. These two nanoparticle dispersions, as illustrated in Figures 1B and 1C, have lesser amounts of surfactant present as the surfaces of the nanoparticle now display negatively charged carboxylate groups (pK_a~5.0) either from covalent modification, as is the case for the carb-PS, or hydrolysis of ester bonds in the polymer backbone by water, as with PMMA. If surfactant is completely removed from the system, a concurrent increase in particle surface charge must accompany this action. This is displayed in the sf-PS dispersion, Figure 1D, which is stabilized entirely through a high degree of residual sulfate initiator groups present on the particle surface.

Key Nanoparticle Pattern Characteristics

AFM images were obtained for the different combinations of nanoparticle dispersions and patterned substrates. Several criteria were established from the analysis of these images in order to deconvolute the important factors involved with the successful patterning of polymeric nanoparticles. The criteria established for each dispersion and pattern included: 1) the functionality of the surface where the nanoparticle preferentially deposited (i.e., ODT or test monolayer), 2) the effect of the location of a particular monolayer (i.e., grid or square) upon the adsorption of the nanoparticle, 3) the surface coverage of the adsorbed nanoparticle coating, 4) the ordering of the adsorbed nanoparticles (i.e., close pack arrangement), and 5) the number of nanoparticle layers.

Carboxylate-Modified Polystyrene Nanoparticle Patterns

As illustrated in Figure 1B, the carb-PS nanoparticles are stabilized by the presence of surface bound carboxylate groups (pK_a~5) as well as small amounts of adsorbed anionic surfactants. Example tapping mode AFM height images typically observed for samples prepared by exposure of compositionally patterned substrates to carb-PS dispersion are shown in Figure 2. Figures 2A, C are for substrates prepared respectively with R-OH or R-COOH deposited in the grid regions with ODT coating the square-shaped domains. Figure 2B, D are images for substrates prepared using the same coating combination, but with the locations of the coatings reversed. For example, the substrate in Figure 2B was patterned with the R-OH in the square domains and ODT in the grid regions. These images are similar to the images obtained when using RSO_3^- and RNH_2 as the test monolayers in that the carb-PS nanoparticles adsorb to these coatings regardless of the location within the pattern. No deposition of the carb-PS nanoparticle was detected on either portion of the $ArNO_2$ / ODT pattern. These findings are summarized in Table 2 and indicate a preference for the carb-PS nanoparticle to adsorb to the more hydrophilic monolayers.

To gauge the degree of particle coverage on the chosen monolayer, the AFM software was employed. These coverage values (i.e., the percent of a defined domain (square or grid) covered by nanoparticles) are presented in Table 3 and, for the case of carb-PS nanoparticles, indicate relatively dense coverage (~76% and ~72% respectively for the grid and square domains) of the hydrophilic monolayer regions regardless of their location. These particle coverage values are above the 54.7% "jamming limit" of the random sequential adsorption model. Hammond and co-workers have noted that adsorbed particle coverages greater than

the jamming limit indicate the presence of lateral surface diffusion as a result of other forces acting on the nanoparticles after adsorption.[69]

The AFM was also employed to assist in identifying the origin of the lateral surface forces after the adsorption of the nanoparticles by observing if more complex ordering was present. AFM images of the adsorbed particles (not shown here but similar to that shown in Figure 1 of reference 11) show a single layer of randomly arranged particles that did not posses any identifiable organization (i.e., close-packing). A random distribution on hydrophilic monolayers is not unexpected based upon two experimental parameters: static solution deposition and low particle size / adsorption area ratio. The first parameter reflects the deposition of the nanoparticles from a static solution (i.e., not allowed to dry on the pattern), thus limiting the capillary forces between particles that often impose a close-packed particle structure upon the particles while drying. The second experimental parameter refers to several intriguing studies that show ordering of the particles is expected only when the size of the pattern is an integral multiple of the particle diameter and when this multiple is below ~5.[89] Under these conditions, organization is attributed to capillary forces between the particles and the substrate, but is disrupted at pattern sizes greater than ~5 times the particle diameter due to the variations in the size of the particles.

Poly(Methyl Methacrylate) Nanoparticle Patterns

PMMA nanoparticles were also investigated in order to determine the effect of charge and surfactant on nanoparticle adsorption. Like carb-PS, the PMMA nanoparticles, as portrayed in Figure 1C, are stabilized as a dispersion through negatively charged carboxylate

species (pK_a~5.0), which are present as a result of the slow hydrolysis of the ester bond present within the polymer backbone with water, as well as by small amounts of an anionic surfactant. The carb-PS and PMMA nanoparticles are therefore expected to have comparable adsorption tendencies due to their similar surface chemistries regardless of the fact that their bulk is composed of different materials.

Typical images of the PMMA nanoparticles adsorbing to hydrophilic grid and square regions are depicted in Figure 3. As expected, the images for the patterns of ROH (Figures 3A, B), RCOOH (Figures 3C, D), RSO_3^-, and RNH_2 mimic those of the carb-PS nanoparticle. Again, the PMMA nanoparticles prefer to adsorb to the hydrophilic test monolayers regardless of their location upon the surface, as summarized in Table 2. Unlike carb-PS however, the PMMA nanoparticles did adsorb to a small degree to the $ArNO_2$ monolayer in the square and grid domains. This is tentatively attributed to the slight increase in surface carboxylate concentration on the PMMA as opposed to the carb-PS.

Not only were the adsorption tendencies analogous to carb-PS but, as shown in Table 3, the coverage of the nanoparticle on the test monolayers was also similar to the carb-PS nanoparticles. The PMMA nanoparticles covered around 64% of the grid regions and 74% of the square domains. Likewise, the AFM images depict the PMMA nanoparticles adsorbing in a dense fashion without further organization in a single layer.

Polystyrene Nanoparticle Patterns

Unlike the carb-PS, the PS nanoparticle dispersion (Figure 1A) is stabilized through a high concentration of anionic surfactant and residual sulfate groups, thus providing insight

into the effect of high surfactant concentrations upon the adsorption process. The AFM images of the polystyrene adsorption are therefore markedly different than those for the carb-PS nanoparticles. As evident in the AFM images, the PS nanoparticles adsorb only to RSO_3^- (Figure 4A), RCOOH, ROH (Figure 4C), and RNH_2 monolayer when localized in the grid region while the ODT was present within the square domain. No deposition of PS nanoparticle upon a $ArNO_2$ / ODT pattern was observed. Table 2 again summarizes the results of the PS nanoparticle adsorption on the tested monolayers as obtained via AFM. Furthermore, as shown in the AFM images and quantitated in Table 3, when the PS particles do adsorb it is at very low particle coverages (less than 10%) with no surface organization. To insure that the nanoparticles were in fact adsorbing on the grid regions of the monolayer pattern, the sample was interrogated in contact mode AFM. The friction image (Figure 4B), which maps the compositional differences of the pattern based upon the varied frictional interactions between the AFM probe and the surface, confirmed that the nanoparticles were preferentially localized on the grid region. The stark contrast between these results and those for carb-PS and PMMA, indicate that the lack of surfactant and/or presence of surface functional groups must be a critical factor in the adsorption mechanism.

Surfactant-Free Polystyrene Patterns

To investigate the effect of surfactant, a fourth nanoparticle was studied, sf-PS. These nanoparticles, as illustrated in Figure 1D, are stabilized entirely through the presence of a large amount of negatively charged sulfate surface groups. The dispersion is devoid of surfactant. Within the RSO_3^- / ODT (Figure 5C, D), RCOOH / ODT, and ROH / ODT

(Figures 5A, B) patterns, the AFM images show that the sf-PS nanoparticles adsorb preferentially to the grid region regardless of the chemical functionality present in that domain. For the RNH_2 / ODT pattern, the nanoparticle adsorbs only to the RNH_2 when it is present in the grid region, and no deposition of sf-PS is observed for the $ArNO_2$ patterns. These results are again summarized in Table 2. Although there is an apparent non-specificity of adsorption of the surfactant-free particles, it should be noted that when a hydrophilic monolayer is present within the grid region (Figure 5A and 5C) the nanoparticles were better confined to the grid region than when the ODT was present in the grid region. This finding is evident in Table 3, which shows that the particle coverage is higher when the hydrophilic monolayer is present in the square regions. It therefore appears that the nanoparticles are allowed to spread into the square regions from the grid only when a hydrophilic monolayer is present in the square domains. Lastly, AFM images indicate that the nanoparticles are present in a single layer and not organized in any fashion upon the preferred deposition monolayer.

General Theory of Polymeric Nanoparticle Adsorption

Several trends in these data provide clues into the underlying factors that control particle localization. These trends include the particles: 1) preferentially adsorbing to the hydrophilic monolayer; 2) adsorbing equally as well to the preferred monolayer when present in either the grid or square domains; 3) organizing in a dense, non-jamming limit fashion; 4) adsorbing in a single layer; and 5) adsorption specificity being dependent upon the presence and concentration of surfactant. To identify the individual components in the overall

adsorption mechanism for this process, we begin by analyzing the nanoparticles that are most readily and reproducibly localized on the test monolayer / ODT patterns: carb-PS and PMMA. These particles, although composed of different bulk materials, both exhibit nearly identical surface chemistry of carboxyl groups and residual surfactant. We can therefore analyze these findings to identify the factors that play key roles in the polymeric nanoparticle deposition process.

Surfactant is an expected key component in our adsorption system. Several past studies have verified the formation of a fluid-like monolayer of anionic surfactants upon a hydrophobic substrate. The surfactant hydrophobic tails interacting with the hydrophobic surface controls this formation and the coverage is a nonlinear function of the surfactant solution concentration.[90] These fluid layers thus alter the surface chemistry of the substrate to that of the surfactant head group.[73,90-97] This dynamic structure is used in the biochemical arena to prevent and desorb non-specifically bound material from hydrophobic substrates through a detergency process.[78,92,93,95,98,99] On the contrary, when interacting with a hydrophilic substrate, an anionic surfactant will assemble as an easily displaced sub-monolayer or bi-layer type structure.[96,97,100-102]

Due to this detergency effect, the surfactant present in the system is an important factor within this patterning mechanism. This dynamic surfactant monolayer effectively constrains macroscopic hydrophobic/hydrophobic interactions in this system as nanoparticles did not in any case preferentially adsorb to the ODT.[76,103-108] This is illustrated by Table 2 where all of the dispersions containing surfactant (carb-PS, PMMA, and PS) did not adsorb to the ODT monolayer. Furthermore, in the case of the PS dispersions, this high surfactant

excess may also increase the detergency capability of the system thus preventing and desorbing the nanoparticles from even the hydrophilic monolayers as demonstrated in Table 2 and Figure 4. Conversely, in the absence of surfactant with the sf-PS dispersion, as illustrated in Table 2 and Figure 5, the nonspecific adsorption of this dispersion underscores the importance of the surfactant towards allowing precise nanoparticle localization.

With the understanding that the surfactant limits the adsorption of the particles on the hydrophobic regions, the process by which the nanoparticles adsorb with varied success to the assorted hydrophilic monolayers still must be deduced. Based upon the highly successful patterning of carb-PS and PMMA, the adsorption mechanism must also employ an interaction between the carboxylate functional group and the hydrophilic monolayer. We therefore propose that the primary force in the adsorption of the studied particles upon the hydrophilic monolayers is hydrogen bonding.

Hydrogen bonding is a well-known cooperative intermolecular interaction that has been shown to contribute significantly in the adsorption mechanism of molecules upon monolayers.[85,109,110] This interaction can occur under the stipulation that both species contain functional groups capable of hydrogen bonding (i.e., hydrogen bonded to a highly electronegative atoms (F, N, O)). Upon examining the constituents involved in our ideal patterning scenario, both carb-PS and the PMMA surfaces have a significant fraction of protonated carboxyl species as predicted by weak acid/base theory when at a pH slightly greater than the pK_a. Likewise, with the exception of the 4-nitrothiophenol, all of the test monolayers posses an end group capable of hydrogen bonding. This proposition is supported by examining the adsorption profile of the carb-PS and PMMA upon these monolayers

(Table 2 and 3). The particles adsorb significantly to the monolayers that are capable of hydrogen bonding, but are unable to adsorb to the 4-nitrothiophenol pattern. Thus, the surfactant and hydrogen bonding mediated adsorption theory is consistent with the data for the carb-PS and PMMA adsorption.

One possible exception to this proposition is the adsorption of the carb-PS and PMMA to RSO_3^-. This monolayer is mostly deprotonated at the utilized pH, and therefore has a limited number of functional groups present to hydrogen bond with the particles. Furthermore, this monolayer mimics the surface chemistry that is imparted by the surfactant (sodium dodecyl sulfate), which inhibits the adsorption of the particles. Yet, besides both of these noted limitations, the carb-PS and PMMA adsorb well upon the sulfonate monolayer and not to the hydrophobic ODT.

The key distinction between the RSO_3^- and the surfactant monolayer on the ODT lies in the mobility of these species. The ability of the surfactant to prevent and remove adsorbed materials (i.e., detergency) is theorized to involve a dynamic, or fluidic, movement of the surfactant layer to surround a particle.[99,111-113] The thiolate gold-bound sulfonate monolayer, on the other hand, does not have a comparable mobility, which prevents it from contributing in the prevention/removal mechanism. Moreover, this confinement of the RSO_3^- monolayer has been shown to raise the pK_a of the monolayer, thus increasing the amount of hydrogen bonding terminal end groups present on the substrate.[110] This test monolayer is therefore an allegory of the proposed surfactant and hydrogen bonding mediated adsorption theory rather than an exception.

This surfactant/hydrogen bonding mediated adsorption theory is further tested by extending it towards the PS nanoparticle adsorption behavior. These nanoparticles, as previously mentioned, are stabilized through the presences of sulfonate groups as well as residual surfactant, which is present in greater concentration than in either the carb-PS or PMMA dispersions.[114,115] This difference in surface chemistry and surfactant concentration allows us to probe the relative importance of the components of our theory as well as look for other less prominent forces.

As before, the surfactant that is present in the matrix is preventing the adsorption of the particles upon the hydrophobic ODT pattern. However, the data (Tables 2 and 3, Figure 4) not only show a decreased amount of PS particle adsorption, but a tendency to adsorb only to the hydrogen bonding monolayers when present in the grid region of the pattern. A two-fold explanation of this phenomenon, utilizing the same ideas expressed above, begins by observing the different surface chemistry and matrix environment of the PS particles. The sulfonic acid groups at the PS surface are mostly deprotonated at the pH utilized reducing the likelihood of hydrogen bonding interactions between the surface and the particle. Furthermore, the PS dispersion contains an increased concentration of surfactant, which not only prevents the adsorption of the particle to the hydrophobic monolayers, but possibly reduces the adsorption of the particles to the hydrophilic areas as well. The cumulative effect of the decreased probability of the particle to find favorable hydrogen bonding environment and the increased tendency to desorb, results in the observed decreased adsorption density upon the hydrophilic monolayers. This overall decrease in the dominance of the hydrogen

bonding involved in the adsorption of PS nanoparticles, has a further effect in allowing more recessive stabilization forces to become more prominent.

Lastly, within systems that display no affinity towards a patterned functional group (i.e., sf-PS), it was noted that when and if they adsorb, it is on the grid region. We do not understand the basis of this phenomenon, but are concerned that minimal scarring of the gold surface from the conformal contact between the sample and photolithographic mask used in the patterning process may play a role. The presence of topographic features that act as a particle adsorption template in conjunction with capillary forces have been reported.[76,116,117] Further experimentation is currently underway to determine the effects of small surface asperities in the patterning of polymeric nanoparticles as well as to create the negative of the photolithographic mask used.

Conclusion

Through the judicious choice of both polymeric nanoparticles and monolayers within a hydrophilic/phobic compositionally patterned surface, a theory for the self-assembled adsorption mechanism of polymeric nanoparticles has been presented. The adsorption process is mediated through the combination of surfactant and hydrogen bonding, whose importance can be adjusted though the type of nanoparticle and solution components used. The difference between the adsorption theory of polymeric nanoparticles and other particles that have been studied to date upon hydrophilic/phobic patterns lies in the critical addition of surfactant. Further investigations involving the development and extension of this theory toward a greater variety of both hydrophilic monolayers and polymeric nanoparticles are underway. We envision that this increased understanding of the polymeric nanoparticles

adsorption mechanism will allow for the usage of smaller building blocks in successfully creating miniaturized structures. Current and future works allowed by this understanding include increasing the complexity of the polymeric structures to create more functional platforms. These complex patterns can be created through a variety of several differing techniques including photolithography, microcontact printing, and AFM tip modification,[62,63] or the combination of methodologies as displayed in Figure 6.

Acknowledgements

This work was supported by the Microanalytical Instrumentation Center, and the Office of Basic Energy Science, Chemical Sciences Division of the U.S. Department of Energy. The Ames Laboratory is operated for the U. S. Department of Energy by Iowa State University under Contract W-7405-eng-82.

References

(1) Bruchez, M.; Moronne, M.; Gin, P.; Weiss, S.; Alivisatos, A. P. *Science* **1998**, *281*, 2013-2016.

(2) Chan, W. C. W.; Nie, S. *Science* **1998**, *281*, 2016-2018.

(3) Jiang, P.; Ostojic, G. N.; Narat, R.; Mittleman, D. M.; Colvin, V. L. *Adv. Mater.* **2001**, *13*, 389-393.

(4) Xia, Y.; Gates, B.; Li, Z.-Y. *Adv. Mater.* **2001**, *13*, 409-413.

(5) Cheng, W.; Dong, S.; Wang, E. *Anal. Chem.* **2002**, *74*, 3599-3604.

(6) Toshima, N.; Yonezawa, T. *New Journal of Chemistry* **1998**, *22*, 1179-1201.

(7) Soper, S. A.; Ford, S. M.; Qi, S.; McCarley, R. L.; Kelly, K.; Murphy, M. C. *Anal. Chem.* **2000**, *72*, 643A-651A.

(8) Figeys, D.; Pinto, D. *Anal. Chem.* **2000**, *72*, 330A-335A.

(9) Reyes, D. R.; Iossifidis, D.; Auroux, P.-A.; Manz, A. *Anal. Chem.* **2002**, *74*, 2623-2636.

(10) Auroux, P.-A.; Iossifidis, D.; Reyes, D. R.; Manz, A. *Anal. Chem.* **2002**, *74*, 2637-2652.

(11) Pris, A. D.; Porter, M. D. *Nano Letters* **2002**, *2*, 1087-1091.

(12) Deckman, H. W.; Dunsmuir, J. H. *Appl. Phys. Lett.* **1982**, *41*, 377-379.

(13) Deckman, H. W.; Dunsmuir, J. H. *J. Vac. Sci. Technol., B* **1983**, *1*, 1109-1112.

(14) Deckman, H. W.; Dunsmuir, J. H.; Garoff, S.; McHenry, J. A.; Peiffer, D. G. *J. Vac. Sci. Technol., B* **1988**, *6*, 333-336.

(15) Denkov, N. D.; Velev, O. D.; Kralchevsky, P. A.; Ivanov, I. B.; Yoshimura, H.; Nagayama, K. *Langmuir* **1992**, *8*, 3183-3190.

(16) Dimitrov, A. S.; Dushkin, C. D.; Yoshimura, H.; Nagayama, K. *Langmuir* **1994**, *10*, 432-440.

(17) Dimitrov, A. S.; Nagayama, K. *Langmuir* **1996**, *12*, 1303-1311.

(18) Kim, E.; Xia, Y.; Whitesides, G. M. *Adv. Mater.* **1996**, *8*, 245-247.

(19) Jiang, P.; Bertone, J. F.; Hwang, K. S.; Colvin, V. L. *Chem. Mater.* **1999**, *11*, 2132-2140.

(20) Park, S. H.; Xia, Y. *Langmuir* **1999**, *15*, 266-273.

(21) Jiang, P.; Hwang, K. S.; Mittleman, D. M.; Bertone, J. F.; Colvin, V. L. *J. Am. Chem. Soc.* **1999**, *121*, 11630-11637.

(22) Xia, Y.; Tien, J.; Qin, D.; Whitesides, G. M. *Langmuir* **1996**, *12*, 4033-4038.

(23) Jiang, P.; Cizeron, J.; Bertone, J. F.; Colvin, V. L. *J. Am. Chem. Soc.* **1999**, *121*, 7957-7958.

(24) Kulinowski, K. M.; Jiang, P.; Vaswani, H.; Colvin, V. L. *Adv. Mater.* **2000**, *12*, 833-838.

(25) Böhmer, M. *Langmuir* **1996**, *12*, 5747-5750.

(26) Giersig, M.; Mulvaney, P. *Langmuir* **1993**, *9*, 3408-3413.

(27) Trau, M.; Saville, D. A.; Aksay, I. A. *Science* **1996**, *272*, 706-709.

(28) Kumacheva, E.; Golding, R. K.; Allard, M.; Sargent, E. H. *Adv. Mater.* **2002**, *14*, 221-224.

(29) Hayward, R. C.; Saville, D. A.; Aksay, I. A. *Nature* **2000**, *404*, 56-59.

(30) Patil, Y.; Mayya, K. S.; Sastry, M. *Langmuir* **1999**, *15*, 6587-6590.

(31) Bandyopadhyay, K.; Patil, V.; Vijayamohanan, K.; Sastry, M. *Langmuir* **1997**, *13*, 5244-5248.

(32) Colvin, V. L.; Goldstein, A. N.; Alivisatos, A. P. *J. Am. Chem. Soc.* **1992**, *114*, 5521-5230.

(33) He, H. X.; Zhang, H.; Li, Q. G.; Zhu, T.; Li, S. F. Y.; Liu, Z. F. *Langmuir* **2000**, *16*, 3846-3851.

(34) Doron, A.; Katz, E.; Willner, I. *Langmuir* **1995**, *11*, 1313-1317.

(35) Wang, J.; Zhu, T.; Song, J.; Liu, Z. *Thin Solid Films* **1998**, *327-329*, 591-594.

(36) Zhu, T.; Zhang, X.; Wang, J.; Fu, X.; Liu, Z. *Thin Solid Films* **1998**, *327-329*, 595-598.

(37) Schmitt, J.; Machtle, P.; Eck, D.; Mohwald, H.; Helm, C. A. *Langmuir* **1999**, *15*, 3256-3266.

(38) Auer, F.; Scotti, M.; Ulman, A.; Jordan, R.; Sellergren, B.; Garno, J.; Liu, G.-Y. *Langmuir* **2000**, *16*, 7554-7557.

(39) Templeton, A. C.; Zamborini, F. P.; Wuelfing, W. P.; Murray, R. W. *Langmuir* **2000**, *16*, 6682-6688.

(40) Fan, H.; López, G. P. *Langmuir* **1997**, *13*, 119-121.(41) Lvov, Y.; Ariga, K.; Onda, M.; Ichinose, I.; Kunitake, T. *Langmuir* **1997**, *13*, 6195-6203.

(42) Yonezawa, T.; Onoue, S.-y.; Kunitake, T. *Chem. Lett.* **1998**, 689-690.

(43) Lvov, Y. M.; Price, R. R.; Selinger, J. V.; Singh, A.; Spector, M. S.; Schnur, J. M. *Langmuir* **2000**, *16*, 5932-5935.

(44) Serizawa, T.; Takeshita, H.; Akashi, M. *Langmuir* **1998**, *14*, 4088-4094.

(45) Müller, W. T.; Klein, D. L.; Lee, T.; Clarke, J.; McEuen, P. L.; Schultz, P. G. *Science* **1995**, *268*, 272-273.

(46) Chen, J. Y.; Klemic, J. F.; Elimelech, M. *Nano Letters* **2002**, *2*, 393-396.

(47) Bhat, R. R.; Fischer, D. A.; Genzer, J. *Langmuir* **2002**, *18*, 5640-5643.

(48) Masuda, Y.; Seo, W. S.; Koumoto, K. *Thin Solid Films* **2001**, *382*, 183-189.

(49) Masuda, Y.; Itoh, M.; Yonezawa, T.; Koumoto, K. *Langmuir* **2002**, *18*, 4155-4159.

(50) Plummer, S. T.; Bohn, P. W. *Langmuir* **2002**, *18*, 4142-4149.

(51) Bain, C. D.; Troughton, E. B.; Tao, Y.-T.; Evall, J.; Whitesides, G. M.; Nuzzo, R. G. *J. Am. Chem. Soc.* **1989**, *111*, 321-335.

(52) Bain, C. D.; Evall, J.; Whitesides, G. M. *J. Am. Chem. Soc.* **1989**, *111*, 7155-7164.

(53) Porter, M. D.; Bright, T. B.; Allara, D. L.; Chidsey, C. E. D. *J. Am. Chem. Soc.* **1987**, *109*, 3559-3568.

(54) Ulman, A. *Chem. Rev.* **1996**, *96*, 1533-1554.

(55) Tarlov, M. J.; Burgess, D. R. F., Jr.; Gillen, G. *J. Am. Chem. Soc.* **1993**, *115*.

(56) Lewis, M.; Tarlov, M.; Carron, K. *J. Am. Chem. Soc.* **1995**, *117*, 9574-9575.

(57) Zhang, Y.; Terrill, R. H.; Tanzer, T. A.; Bohn, P. W. *J. Am. Chem. Soc.* **1998**, *120*, 2654-2655.

(58) Norrod, K. L.; Rowlen, K. L. *J. Am. Chem. Soc.* **1998**, *120*, 2656-2657.

(59) Kumar, A.; Biebuyck, H. A.; Whitesides, G. M. *Langmuir* **1994**, *10*, 1498-1511.

(60) Kumar, A.; Whitesides, G. M. *Science* **1994**, *263*, 60-62.

(61) Xia, Y.; Whitesides, G. M. *Langmuir* **1997**, *13*, 2059-2067.

(62) Wadu-Mesthrige, K.; Xu, S.; Amro, N. A.; Liu, G.-y. *Langmuir* **1999**, *15*, 8580-8583.

(63) Kenseth, J. R.; Harnisch, J. A.; Jones, V. W.; Porter, M. D. *Langmuir* **2001**, *17*, 4105-4112.

(64) Sato, T.; Hasko, D. G.; Ahmed, H. *J. Vac. Sci. Technol., B* **1997**, *15*, 45-48.

(65) Tien, J.; Terfort, A.; Whitesides, G. M. *Langmuir* **1997**, *13*, 5349-5355.

(66) Zheng, J.; Zhu, Z.; Chen, H.; Liu, Z. *Langmuir* **2000**, *16*, 4409-4412.

(67) Maye, M. M.; Luo, J.; Han, L.; Zhong, C.-J. *Nano Letters* **2001**, *1*, 575-579.

(68) Guo, Q.; Arnoux, C.; Palmer, R. E. *Langmuir* **2001**, *17*, 7150-7155.

(69) Chen, K. M.; Jiang, X.; Kimerling, L. C.; Hammond, P. T. *Langmuir* **2000**, *16*, 7825-4834.

(70) Mesquida, P.; Stemmer, A. *Adv. Mater.* **2001**, *13*, 1395-1398.

(71) Aizenberg, J.; Braun, P. V.; Wilzius, P. *Phys. Rev. Lett.* **2000**, *84*, 2997-3000.

(72) Friebel, S.; Aizenberg, J.; Abad, S.; Wilzius, P. *Appl. Phys. Lett.* **2000**, *77*, 2406-2408.

(73) Ramos, L.; Weitz, D. A. *Langmuir* **2001**, *17*, 2275-2277.

(74) Derjaguin, B. V.; Landau, L. *Acta Physicochim. URSS* **1941**, *14*, 633-662.

(75) Verwey, E. J. W.; Overbeek, J. T. G. *Theory of the Stability of Lyophobic Colloids*; Elsevier: Amsterdam, 1948.

(76) Israelachvili, J. N. *Intermolecular and Surface Forces*; Second ed.; Academic Press: London, 1992.

(77) Turyan, I.; Mandler, D. *J. Am. Chem. Soc.* **1998**, *120*, 10733-10742.

(78) Jones, V. W.; Kenseth, J. R.; Porter, M. D.; Mosher, C. L.; Henderson, E. *Anal. Chem.* **1998**, *70*, 1233-1241.

(79) O'Brien, J. C.; Stickney, J. T.; Porter, M. D. *Langmuir* **2000**, *16*, 9559-9567.

(80) Shimazu, K.; Teranishi, T.; Sugihara, K.; Uosaki, K. *Chem. Lett.* **1998**, 669-670.

(81) Sugihara, K.; Shimazu, K.; Uosaki, K. *Langmuir* **2000**, *16*, 7101-7105.

(82) Chen, X.; Patel, N.; Davies, M. C.; Roberts, C. J.; Tendler, S. J. B.; Williams, P. M.; Davies, J.; Dawkes, A. C.; Edwards, J. C. *Appl. Phys. A* **1998**, *66*, S631-S634.

(83) Bryant, M. A.; Crooks, R. M. *Langmuir* **1993**, *9*, 385-387.

(84) Jiang, X.; Ortiz, C.; Hammond, P. T. *Langmuir* **2002**, *18*, 1131-1143.

(85) Clark, S. L.; Hammond, P. T. *Langmuir* **2000**, *16*, 10206-10214.

(86) Zheng, H.; Lee, I.; Rubner, M. F.; Hammond, P. T. *Adv. Mater.* **2002**, *14*, 569-572.

(87) Odian, G. *Emulsion Polymerization*; Third ed.; John Wiley & Sons, Inc.: New York, 1991, pp 335-355.

(88) Although not specified by the vendor, sodium dodecyl sulfate is the most commonly utilized surfactants in the emulsion polymerization process.

(89) Lee, I.; Zheng, H.; Rubner, M. F.; Hammond, P. T. *Adv. Mater.* **2002**, *14*, 572-577.

(90) Montgomery, M. E., Jr.; Wirth, M. J. *Langmuir* **1994**, *10*, 861-869.

(91) Sigal, G. B.; Mrksich, M.; Whitesides, G. M. *Langmuir* **1997**, *13*, 2749-2755.

(92) Petrash, S.; Sheller, N. B.; Dando, W.; Foster, M. D. *Langmuir* **1997**, *13*, 1881-1883.

(93) Shen, D.; Wu, X.; Liu, X.; Kang, Q.; Chen, S. *Microchem. J.* **1999**, *63*, 322-332.

(94) Ward, R. N.; Davies, P. B.; Bain, C. D. *J. Phys. Chem. B* **1997**, *101*, 1594-1601.

(95) Green, R. J.; Su, T. J.; Lu, J. R.; Penfold, J. *J. Phys. Chem. B* **2001**, *105*, 1594-1602.

(96) Grosse, I.; Estel, K. *Colloid Polym. Sci.* **2000**, *278*, 1000-1006.

(97) Giasson, S.; Kuhl, T. L.; Israelachvili, J. N. *Langmuir* **1998**, *14*, 891-898.

(98) Perrin, A.; Lanet, V.; Theretz, A. *Langmuir* **1997**, *13*, 2557-2563.

(99) Fainerman, V. B.; Lucassen-Reynders, E. H.; Miller, R. *Colloids Surf., A* **1998**, *143*, 141-165.

(100) Grant, L. M.; Ducker, W. A. *J. Phys. Chem. B* **1997**, *101*, 5337-5345.

(101) Lichtenbelt, J. W. T.; Heuvelsland, W. J. M.; Oldenzeel, M. E.; Zsom, R. L. J. *Colloids and Surfaces, B: Biointerfaces* **1993**, *1*, 75-82.

(102) Penfold, J.; Staples, E.; Tucker, I.; Thomas, R. K. *Langmuir* **2002**, *18*, 5755-5760.

(103) Parker, J. L.; Claesson, P. M. *Langmuir* **1994**, *10*, 635-639.

(104) Ishida, N.; Kinoshita, N.; Miyahara, M.; Higashitani, K. *J. Colloid Interface Sci.* **1999**, *216*, 387-393.

(105) Ishida, N.; Sakamoto, M.; Miyahara, M.; Higashitani, K. *Langmuir* **2000**, *16*, 5681-5687.

(106) Yakubov, G. E.; Butt, H.-J.; Vinogradova, O. I. *J. Phys. Chem. B* **2000**, *104*, 3407-3410.

(107) Considine, R. F.; Drummond, C. J. *Langmuir* **2000**, *16*, 631-635.

(108) Mahnke, J.; Stearnes, J.; Hayes, R. A.; Fornasiero, D.; Ralston, J. *Physical Chemistry Chemical Physics* **1999**, *1*, 2793-2798.

(109) Sun, L.; Kepley, L. J.; Crooks, R. M. *Langmuir* **1992**, *8*, 2101-2103.

(110) Sun, L.; Crooks, R. M. *Langmuir* **1993**, *9*, 1775-1780.

(111) Doudevski, I.; Hayes, W. A.; Woodward, J. T.; Schwartz, D. K. *Colloids Surf., A* **2000**, *174*, 233-243.

(112) Mackie, A. R.; Gunning, A. P.; Wilde, P. J.; Morris, V. J. *Langmuir* **2000**, *16*, 2242-2247.

(113) Welin-Klintstrom, S.; Askendal, A.; Elwing, H. *J. Colloid Interface Sci.* **1993**, *158*, 188-194.

(114) Mohan, D., PolyMicrospheres.

(115) Turner, K., Bangs Laboratories.

(116) Yin, Y.; Lu, Y.; Gates, B.; Xia, Y. *J. Am. Chem. Soc.* **2001**, *123*, 8718-8729.

(117) Ozin, G. A.; Yang, S. M. *Advanced Functional Materials* **2001**, *11*, 95-104.

Figure Captions

Figure 1: Representative surface chemistry of A) polystyrene, B) carboxylate modified polystyrene, C) polymethyl(methacrylate), and D) surfactant-free polystyrene dispersions

Figure 2: Typical tapping mode height images of carboxylate-modified polystyrene nanoparticles patterned on: (A) 11-mercapto-1-undecanol and (C) 16-mercaptohexadecanoic acid in the grid region and on (B) 11-mercapto-1-undecanol and (D) 16-mercaptohexadecanoic acid in the square regions

Figure 3: Tapping mode height images of PMMA nanoparticles patterned on: (A) 11-mercapto-1-undecanol and (C) 16-mercaptohexadecanoic acid within the grid region and (B) 11-mercapto-1-undecanol and (D) 16-mercaptohexadecanoic acid in the square regions

Figure 4: Contact mode height (A) and friction (B) image of polystyrene nanoparticles patterned on 11-mercaptodecane-1-sulfonate monolayer in the grid region and (C) tapping mode height image of polystyrene nanoparticles patterned on 11-mercapto-1-undecanol monolayer in the grid region

Figure 5: Tapping mode height images of surfactant-free polystyrene nanoparticles patterned on:(A) 11-mercapto-1-undecanol and (C) 11-mercaptodecane-1-sulfonate in the grid region and (B) 11-mercapto-1-undecanol (D) 11-mercaptodecane-1-sulfonate in the square regions

Figure 6: Tapping mode height image depicting the ability to "plow" within the first monolayer and subsequently deposit a second monolayer and polymeric nanoparticles in the "plowed" region

Table 1: List of Abbreviations and Descriptors

Polymeric Nanoparticle (diameter)	**Abbreviation**	**Descriptor**
Carboxylate-modified polystyrene (90-nm)	carb-PS	Carboxylate, sulfate groups and minimal surfactant
Poly(methyl methacrylate) (80-nm)	PMMA	Carboxylate groups and minimal surfactant
Surfactant-free polystyrene (100-nm)	sf-PS	Sulfate groups
Polystyrene (80-nm)	PS	Sulfate groups and surfactant
Monolayer Coating Precursor		
11-mercaptodecane-1-sulfonate	RSO_3^-	$pK_a<1.5$, $\theta\sim15°$
16-mercaptohexadecanoic acid	RCOOH	$pK_a<6.4$, $\theta\sim15°$
11-mercaptor-1-undecanol	ROH	$\theta\sim16°$
2-aminoethane thiol	RNH_2	$pK_a<10$-11, $\theta\sim31.5°$
octadecane thiol	ODT	$\theta\sim100°$
4-nitrothiophenol	$ArNO_2$	$\theta\sim51°$

Table 2: Results of Nanoparticle Deposition

Particle Type	Test Monolayer	Region of Particle Deposition
carb-PS	RSO_3^-	test monolayer in square and grid
	RCOOH	test monolayer in square and grid
	ROH	test monolayer in square and grid
	RNH_2	test monolayer in square and grid
	$ArNO_2$	no deposition detected
PMMA	RSO_3^-	test monolayer in square and grid
	RCOOH	test monolayer in square and grid
	ROH	test monolayer in square and grid
	RNH_2	test monolayer in square and grid
	$ArNO_2$	small amount in test monolayer in square and grid
PS	RSO_3^-	test monolayer in grid
	RCOOH	test monolayer in grid
	ROH	test monolayer in grid
	RNH_2	test monolayer in grid
	$ArNO_2$	no deposition detected
sf-PS	RSO_3^-	grid regardless of functional group
	RCOOH	grid regardless of functional group
	ROH	grid regardless of functional group
	RNH_2	test monolayer in grid
	$ArNO_2$	deposition in all locations

Table 3: Percent Particle Coverage on Test Monolayer Region

Particle Type	Test Monolayer Location	RSO_3^-	RCOOH	ROH	RNH_2	$ArNO_2$
PS-carb	grid	86	63	83	75	XXX
	square	58	86	103	44	XXX
PMMA	grid	36	70	86	8	5
	square	89	81	97	30	8
PS	grid	13	9	8	8	XXX
	square	XXX	XXX	XXX	XXX	XXX
sf-PS	grid	96	84	75	77	156
	square	208	130	180	XXX	278

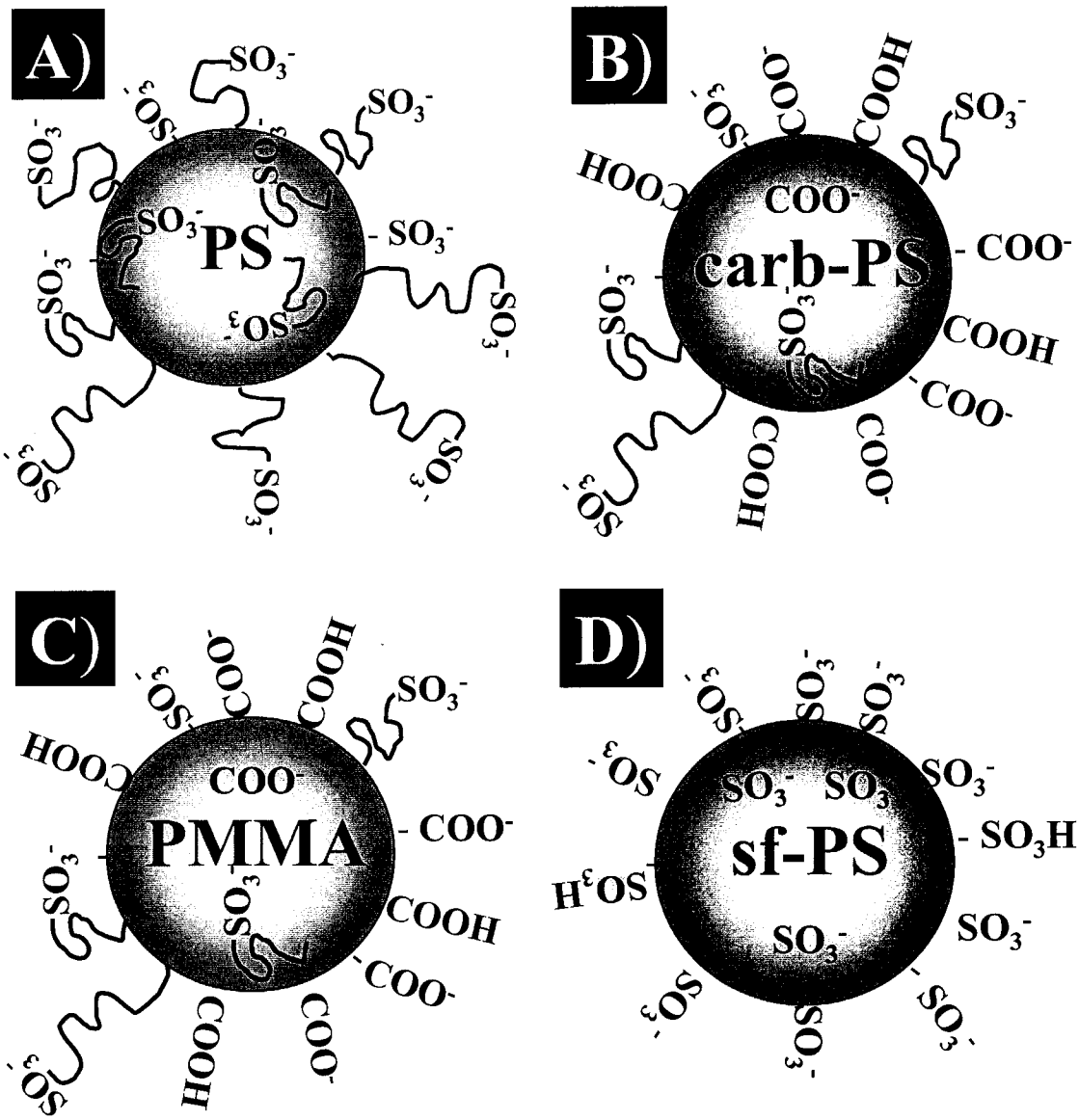

Figure 1

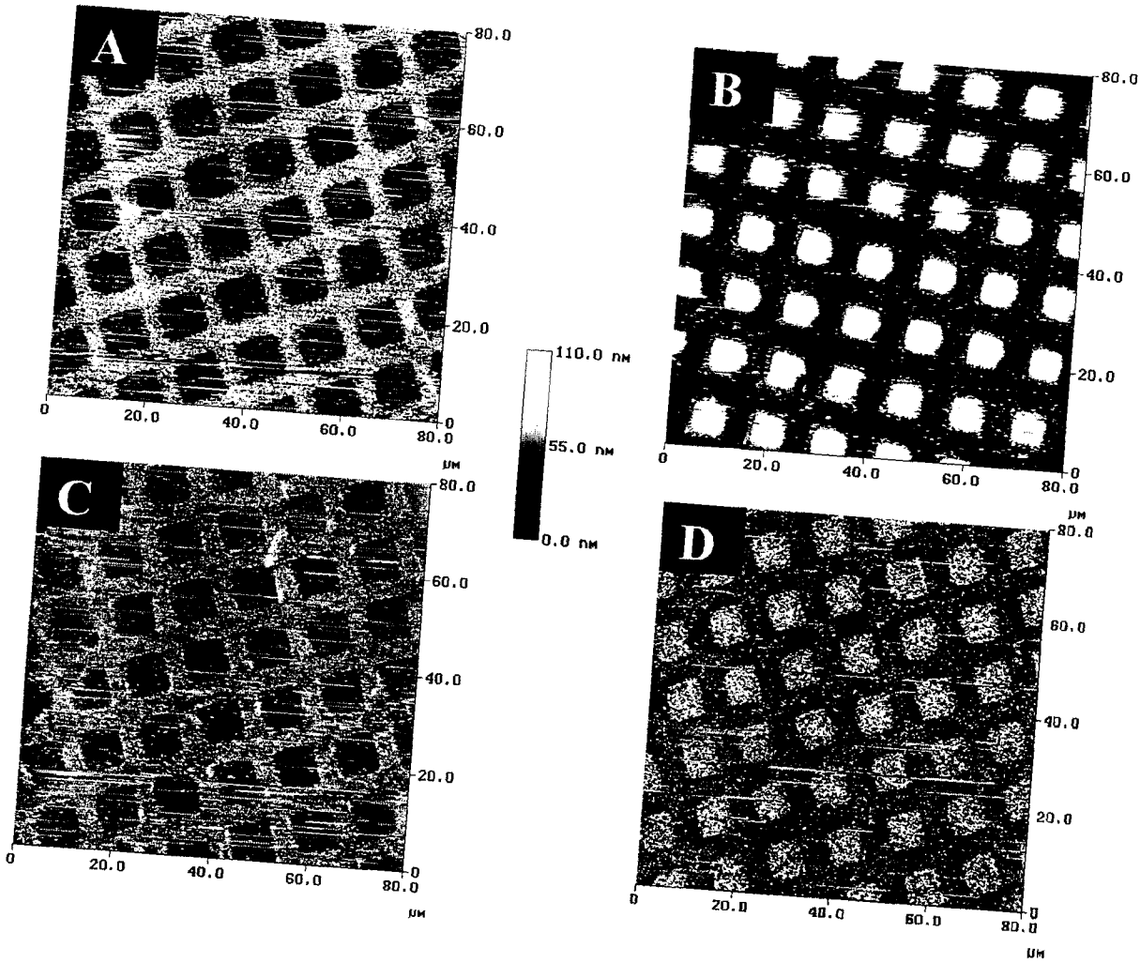

Figure 2

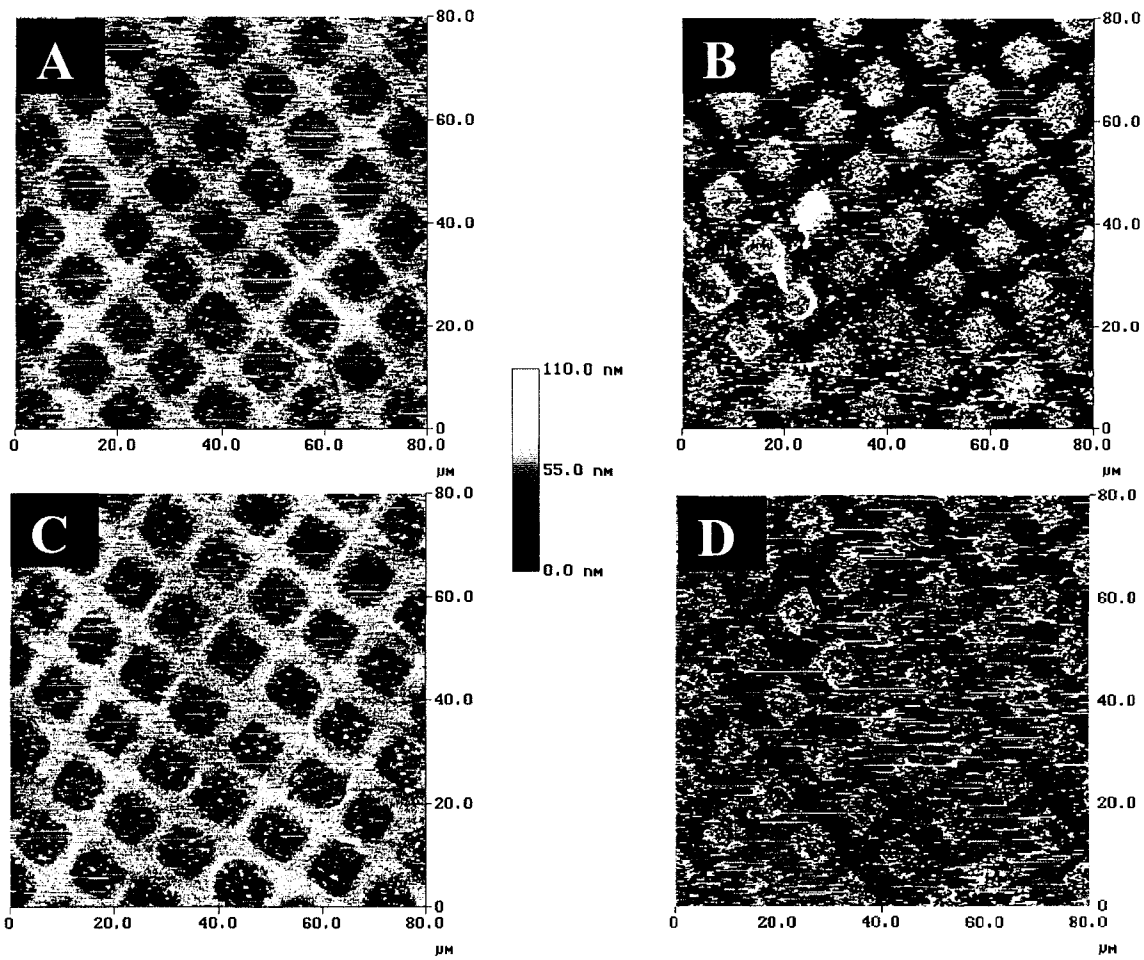

Figure 3

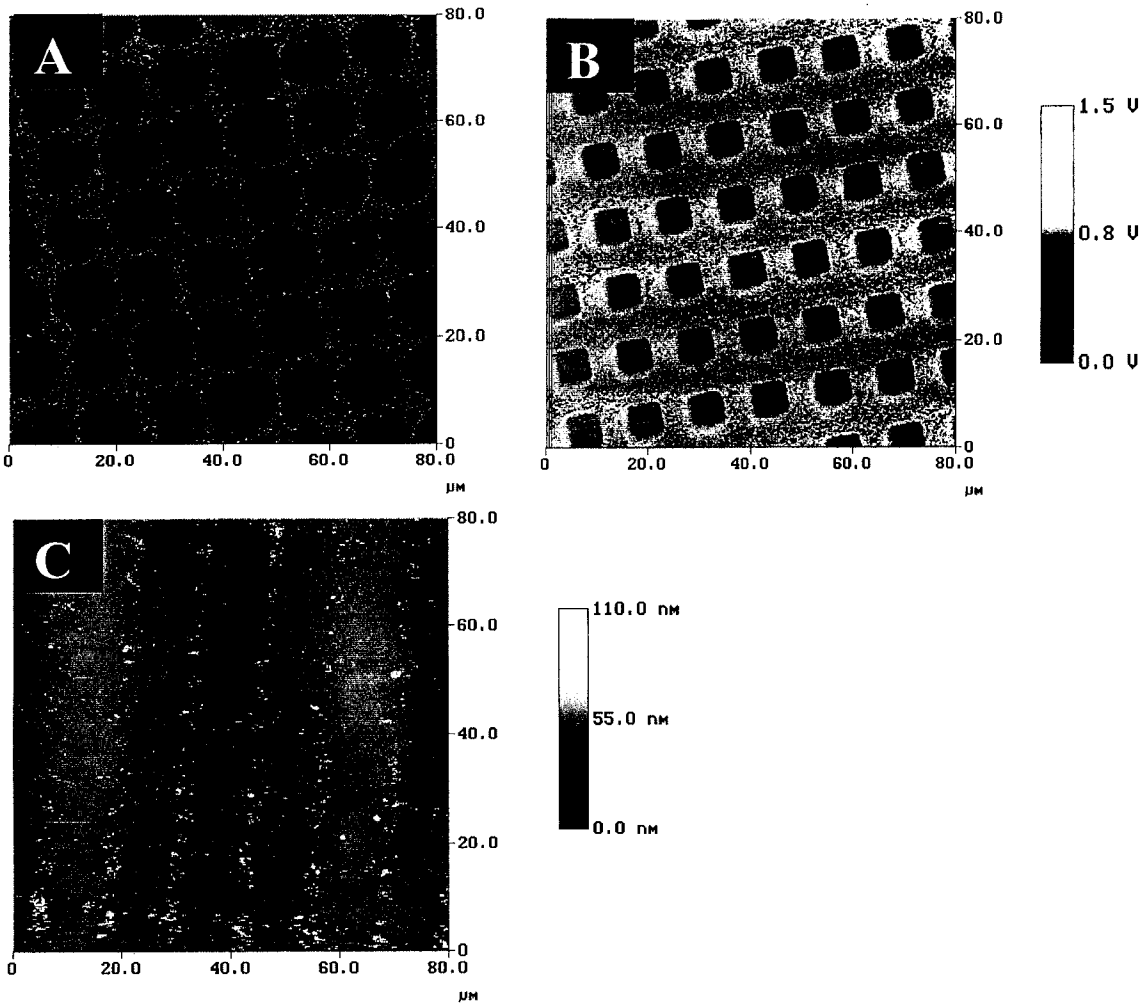
A
B
C
80.0
60.0
40.0
20.0
0
20.0
40.0
60.0
80.0
μm
1.5 V
0.8 V
0.0 V
110.0 nm
55.0 nm
0.0 nm

Figure 4

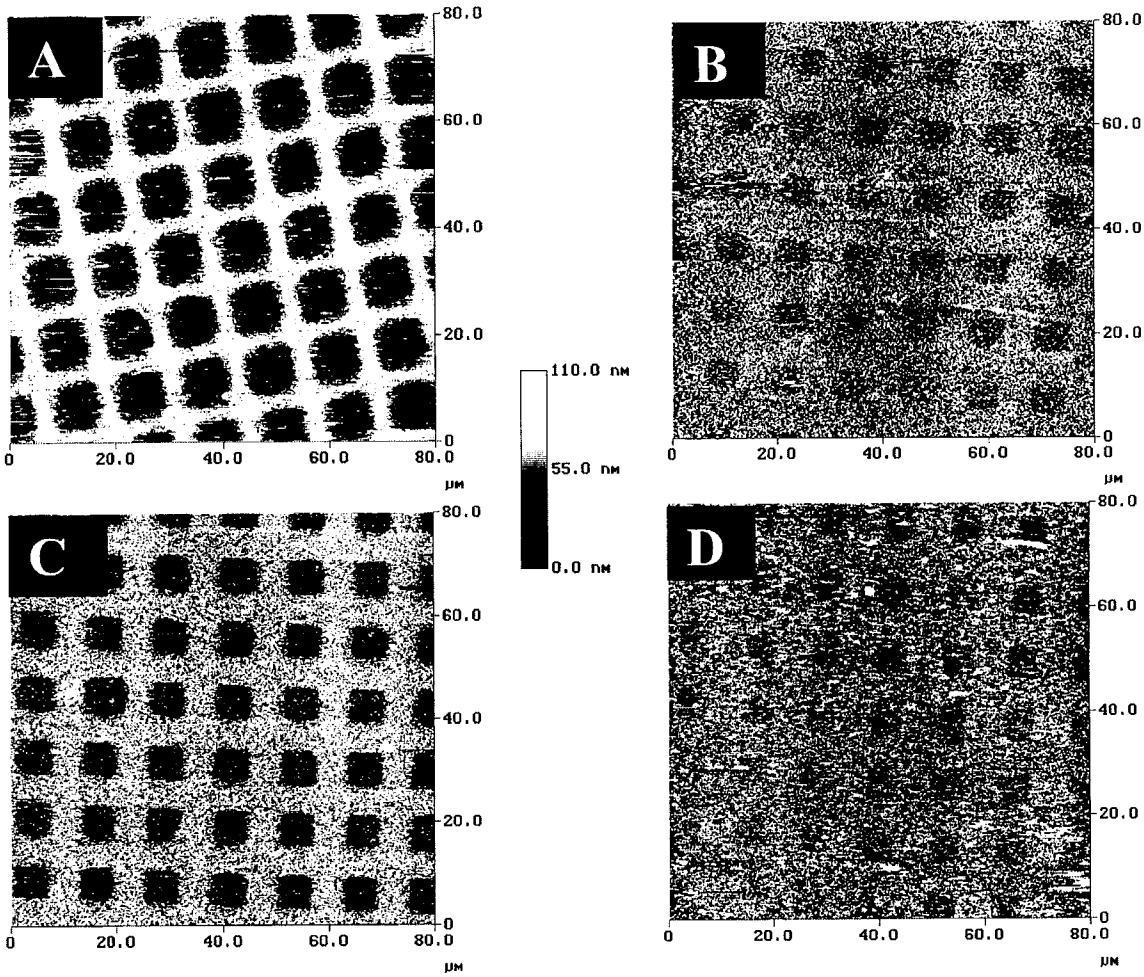

Figure 5

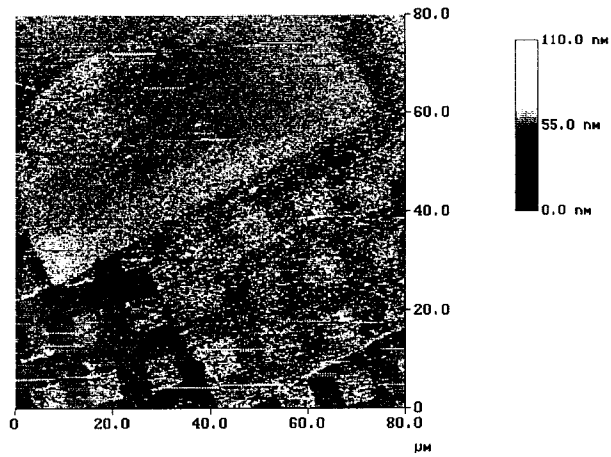

Figure 6

CHAPTER 2: CREATION OF SUB-MICROMETER STRUCTURES USING POLYMERIC NANOPARTICLE LAYERS AND PHOTOLITHOGRAPHY

A letter published in *NanoLetters*[1]

Andrew D. Pris[2] and Marc D. Porter[2,3]

Abstract

This Letter describes a novel route for the facile construction of mechanically robust, submicron architectures. The method couples the layer-by-layer deposition of charged polymeric nanoparticles with photopatterning and thermal processing. The merits of the method are demonstrated by the fabrication and microscopic characterization of massively dense (~650,000 wells/cm^2), ultrasmall volume (3-15 fL) well arrays. The well depth is controlled by the number of nanoparticle layers, with well depths as low as ~4-nm obtained. The lateral dimensions of the wells, which were several microns, are defined by the photomask. Thermal processing not only further enhances the structural stability of the array, but also dramatically reduces the depth of the wells. Potential applications of this preparative strategy are discussed briefly.

---

[2] Microanalytical Instrumentation Center, Ames Laboratory-USDOE, and Department of Chemistry, Iowa State University, Ames, IA 50011

[3] Corresponding Author

Introduction

Miniaturization continues to drive advances in many areas of combinatorial discovery (e.g., pharmaceuticals and catalysts). The basis of these advances - the ability to prepare, manipulate, and analyze minute samples in a high throughput manner - is now well established.[1-4] One of the steps in furthering the discovery process is therefore the creation of microsystems (e.g., reaction wells) that can process ever-smaller amounts of sample. To this end, most microstructured systems have been constructed by "top-down" fabrication schemes, which include a range of wet[5-12] and dry[13] etching processes and various types of micromolding.[14-17] In such cases, the depth of a structural feature is dependent on the etch rate of a substrate, with wells trenched, for example, in silicon having volumes of only a few picoliters.[5-7,16] Low volume wells have also been built by a "bottom-up" process that used photolithography to both cross-link and pattern ultrathin (3 to 15-nm) polymeric films.[18]

This Letter describes a new bottom-up strategy for the facile construction of ultrasmall well arrays. The approach photopatterns coatings formed by the systematic, layer-by-layer stacking of polymeric nanoparticles.[19-29] We report herein that this methodology can be used for the construction of dense (~650,000 wells/cm^2), low volume (3-15 fL) well arrays in which the nanometer-sized well depth is controlled by the number of nanoparticle layers. We also show that these arrays can be stabilized by thermal processing with little to no loss of lateral structural definition.

Results and Discussion

The construction of our well arrays draws on the layer-by-layer deposition of polymeric nanoparticles devised by Tsukruk and co-workers.[27,29] This procedure alternates the exposure of a chemically modified silicon surface to colloidal dispersions of positively charged and negatively charged polystyrene nanoparticles. By employing a pH that maintains a surface charge opposite that of the particles in the deposition solution, multilayer stacks of polymeric nanoparticles can be formed upon the substrate a single layer at a time. The number of repetitions in the particle deposition process therefore determines the coating thickness.

In our case, the multilayer stacks were formed using 53±8-nm diameter amidine-modified polystyrene nanoparticles (AMPNs) and 63±5-nm diameter carboxylate modified latex nanoparticles (CMPNs) (Interfacial Dynamics Corporation; 4% (w/w) aqueous dispersions), and an acidic deposition (0.1 M HCl) solution. In 0.1 M HCl, the AMPNs are positively charged due to protonated amine groups, whereas the CMPNs are negatively charged due largely to deprotonated sulfonic acid moieties present from the entrapment of anionic surfactant (lauryl sulfate) and initiator (unspecified) from the emulsion polymerization process.[30-32] The following sections describe how this preparative concept is exploited in order to manipulate the coating thickness, and, in turn, the well depth, at the resolution of a single nanoparticle layer.

Scheme 1 summarizes the four-step fabrication of our well arrays, noting that the samples are protected from direct exposure to the ambient between each deposition step by a thin layer of 0.1 M HCl. Step 1 cleans a silicon substrate[33] in a freshly prepared

peroxysulfuric acid solution (**Caution: "Piranha" is a strongly oxidizing solution and should be handled with extreme care**), which is followed by extensive rinsing with deionized water. This step removes adventitiously adsorbed materials from the silicon surface, and imparts a negative charge to the strongly hydrophilic surface.[34-38] In Step 2, the substrate is rinsed with 0.1 M HCl, and is then mounted on a sheet of fresh Parafilm™; the Parafilm™ sheet functions as a hydrophobic barrier that confines the contacting liquid to the top of the substrate. Next, 200 μL of the AMPN solution is carefully pipetted into the retained aqueous layer of 0.1 M HCl, which is allowed to stand for ~20 min. The resulting solution, which we estimate has a pH~2, deposits a layer of positively charged AMPNs on the silicon surface, which is conveniently idealized as a densely packed particle layer in Step 2a.

The second nanoparticle layer is deposited in Step 3. Step 3 closely parallels the processing in Step 2, but replaces the AMPN solution with the CMPN solution. This step electrostatically couples a CMPN layer to the underlying AMPN layer (Step 3a).[39,40] Moreover, the repetition of Steps 2 and 3 results in the controlled, layer-by-layer increase in the number of particle layers deposited on the substrate (e.g., Steps 2b and 3b). This process can be exited at any point in the cycle by moving to Step 4, which uses photolithography to form the well array within the nanoparticle-based coating.

In Step 4, the sample is again rinsed with 0.1 M HCl, dried carefully under a stream of purified nitrogen, and then irradiated for 40 min with UV light[41] through a photomask. UV-irradiation degrades the polymeric coating through a photooxidative mechanism that is only partially understood.[42,43] After irradiation, the sample is extensively rinsed with

ethanol. The ethanol rinse removes the material degraded by the photolithographic processing, revealing a dense array of wells that, as detailed later, have a depth defined by the number of particle layers and lateral dimensions controlled by the photomask.

Several sets of microscopic characterizations were employed to characterize the structure of our nanoparticle-based well arrays throughout their fabrication. Figure 1 presents an atomic force microscopy (AFM)[44] image (2.5 x 2.5 μm) of a coating formed upon completion of Step 1 (i.e., after deposition of a AMPN layer). As expected, the AMPN layer has a pebbled topography, indicative of a dense, but disordered, array of spherically shaped nanoparticles. The root-mean-square roughness of the coating is ~20-nm. Topographic images for samples prepared for up to five particle layers (thicker layers were not examined) were nearly identical in topography and roughness to that for the first particle layer.

Figure 2 presents an AFM image of a well array formed by exposing a three-layer coating of polymeric nanoparticles (i.e., AMPN/CMPN/AMPN) to UV irradiation for 40 min through a micromesh-type photomask. This mask, which is a 2000 mesh grid (3.05 mm diameter) used for mounting samples for transmission electron microscopy, has 7.5-μm square-shaped openings separated by 5.0-μm wide metallic bars. As is evident, the surface is composed of wells that strongly mimic the lateral dimensions of the pattern in the photomask. Furthermore, the wells have an average depth of 90-nm, which will be shown shortly to correspond to the thickness for a coating prepared by the deposition of three nanoparticle layers. We note that: 1) assessments of the well depth rely on the topographic difference between the irradiated and non-irradiated regions of the sample surface; and 2) a

roughness comparable to the underlying substrate is used as evidence for the complete removal of the degraded material within the irradiated regions.

An example of the utility of this approach for constructing well arrays with extremely large densities is presented in the sequence of optical microscopy (OM) images in Figure 3.[45] This sequence begins in Figure 3A with an image of the entire three layer nanoparticle array, and gradually progresses to higher levels of magnification in Figures 3B and 3C. Inspection of the latter images shows that the wells are uniform in size throughout the area exposed by the photomask. Moreover, an estimate based on the mask area and size of the features within the photomask yields an array density of ~650,000 wells/cm^2, which begins to demonstrate the merits of our concept for the facile preparation of ultrahigh density arrays.

The ability to manipulate the depth of the wells was examined by varying the number of nanoparticle layers and analyzing the topographic changes by AFM after photopatterning. Figure 4 summarizes the results, and includes a plot of the theoretical thickness for a closest-packed, ABA structure of 60-nm particles for comparative purposes.[46] The plot of the experimentally determined well depths reveals that the first particle layer has an average thickness of nearly 45-nm, whereas the thickness for all subsequent layers increases by only ~35-nm per layer. In both cases, the observed thicknesses are well below those predicted for a closest packed, three-dimensional particle stack. The difference between the observed and predicted thicknesses is attributed to the disorder in particle packing, as evident in Figure 1. Nevertheless, the experimental findings clearly demonstrate the ability to reliably manipulate the well depth simply by changing the number of nanoparticle layers, which translates to

volume elements ranging from ~3 fL for a single nanoparticle layer to 15 fL for the five layer coating.

The data in Figure 4B also show an increase in the relative uncertainty of the well depth as the number of particle layers increases. This situation is particularly evident in the well depth for the five-layer particle coating, and is attributed to the incomplete removal of the polymeric material within the interior of the wells. The inability to fully remove the polymeric coating was revealed by AFM images, which showed that the roughness at the bottom of the wells was strongly dependent on irradiation time. A 40 min irradiation, while effective in the removal of material for up to three particle layers, was ineffective when patterning a four- and five-particle layer. This complication was addressed by simply irradiating the thicker samples for longer period of times (i.e., 60 min).

We also examined the mechanical integrity of the as-formed wells. Tests have shown, for example, that the as formed arrays are structurally stable even after 24 hr immersions in 0.1 M HCl, distilled water, or 0.1 M NaOH.[47] This stability reflects the intrinsic strength of the adhesion between neighboring particles and between the particles and underlying substrate.[48] The structure of the arrays, however, did degrade when sonicated for ~40 min in deionized water. While the lateral dimensions of the array remained intact, the roughness at the tops of the walls increased with sonication time.

In experiments designed to overcome this instability, we found that thermal processing could readily enhance the robustness of a well array. This processing entailed heating a well array in an annealing oven at 230 °C for 75 min.[49,50] Figure 5 presents an AFM image of a well array prepared from four layers of nanoparticles

(AMPN/CMPN/AMPN/CMPN) after thermal processing. The image shows that thermal processing markedly reduces both the well depth (see below) and the roughness at the top of the well walls. However, the lateral dimensions of the wells, as defined by the photomask, are only marginally affected with little (0.25-μm^2) to no reduction of well area. We attribute the effective retention of the lateral integrity of these microstructures to the strong cohesive interactions of the polymer because the oven temperature was set above the glass transition temperature of polystyrene, but below its melting point. Moreover, a thermally-processed array is structurally stable when sonicated in a range of aqueous solutions (i.e., 0.1 M HCl and 1% sodium dodecylsulfate). Thus, thermal processing enhances the mechanical stability by forming a strongly interconnected structure with minimal loss in lateral definition.

Data incorporated into Figure 4 provide a more comprehensive perspective of how thermal processing changes the topography of the multilayer stack by plotting the well depth after thermal processing as a function of the number of nanoparticle layers. In comparison to the results in Figure 4B, thermal processing strongly decreases the well depth. This decrease reflects the filling of the interstitial voids in the as-formed coatings due to the slow flow of the amorphous polystyrene at this temperature. The plot also shows that thermal processing affects the well depth of the first particle layer more than that of the subsequent layers. That is, the well depth for an array prepared from a single particle layer is nearly 45-nm before melting but only ~4-nm after melting. This difference represents a decrease of more than 90%. However, the relative decrease in thickness is much less (~43%) for all subsequent layers. We are, at present, uncertain as to the origin of this difference, and are designing studies aimed at determining whether a portion of the first layer has partially covered the

bottom of the wells. More importantly, these findings indicate that the well depth can be reproducibly manipulated while enhancing the structural stability of the microfabricated array.

As another test of the potential utility of our well arrays, the ability to confine liquids without leakage between neighboring wells was examined. Figure 6 presents OM images that demonstrate the successful isolation of 10 ppm Rhodamine 110 and 10 ppm Rhodamine B (58% glycerin/water) solutions in four neighboring wells (no thermal processing). The individual solutions were dispensed in each well by using a pulled glass micropipette mounted on micromanipulators. As is evident, the dispensed solution remains effectively localized within its designated well. In contrast to studies of wells with a higher aspect ratio (e.g., wells anisotropically etched in silicon[12]), we found that the extremely low aspect ratio of our wells resulted in the rapid evaporative loss of liquids, even those with low volatilities (e.g., 58% glycerin/water).[16,17] For example, a mixture of glycerin/water evaporated, while under microscopic illumination, within 1-2 min. However, the evaporative loss of liquids was restricted by mounting the wells upon a Peltier cooler (3 °C), which was then placed upon the microscope sample stage, leading to the liquids being stable for up to 6 h.

Conclusion

In summary, a new preparative strategy for the facile fabrication of microstructured materials has been developed and applied to the preparation of high density, low volume well arrays. This strategy takes specific advantage of the ability to control the thickness of such structures at nanometer length scales by the layer-by-layer deposition of charged polymeric

nanoparticles. Coupled with photolithographic techniques and thermal processing, the size, shape, and stability of the resulting architecture can be readily manipulated. We add that varying the particle size can further extend the flexibility of this approach. Experiments aimed at exploring the range and scope of this concept are planned, with approaches to spatially confine solutions for addressing substrates (e.g., antibody arrays) presently being designed. Strategies to stabilize the confined liquids with respect to evaporation are also being examined, as are methods to accurately quantitate the amount of liquid dispensed into each of the wells.

Acknowledgments.

A.D.P. expresses appreciation for a Phillips Petroleum Company Research Fellowship. This work also was supported by the Office of Basic Energy Research, Chemical Sciences Division, U. S. Department of Energy and by the Microanalytical Instrumentation Center of Iowa State University through the W. M. Keck Laboratory for the Fabrication of Microminiaturized Analytical Instrumentation. The Ames Laboratory is operated for the U.S. Department of Energy by Iowa State University under Contract W-7405-Eng-82.

References and Notes

(1) Soper, S. A.; Ford, S. M.; Qi, S.; McCarley, R. L.; Kelly, K.; Murphy, M. C. *Anal. Chem.* **2000**, *72*, 643A-651A.

(2) Figeys, D.; Pinto, D. *Anal. Chem.* **2000**, *72*, 330A-335A.

(3) Reyes, D. R.; Iossifidis, D.; Auroux, P.-A.; Manz, A. *Anal. Chem.* **2002**, *74*, 2623-2636.

(4) Auroux, P.-A.; Iossifidis, D.; Reyes, D. R.; Manz, A. *Anal. Chem.* **2002**, *74*, 2637-2652.

(5) Tan, W.; Yeung, E. S. *Anal. Chem.* **1997**, *69*, 4242-4248.

(6) Ball, J. C.; Scott, D. L.; Lumpp, J. K.; Daunert, S.; Wang, J.; Bachas, L. G. *Anal. Chem.* **2000**, *72*, 497-501.

(7) Nagai, H.; Murakami, Y.; Morita, Y.; Yokoyama, K.; Tamiya, E. *Anal. Chem.* **2001**, *73*, 1043-1047.

(8) Pantano, P.; Walt, D. R. *Chem. Mater.* **1996**, *8*, 2832-2835.

(9) Dam, T. H.; Pantano, P. *Rev. Sci. Instrum.* **1999**, *70*, 3982-3986.

(10) Evans, U.; Colavita, P. E.; Doescher, M. S.; Schiza, M.; Myrick, M. L. *Nano Lett.* **2002**, *2*, 641-645.

(11) Epstein, J. R.; Lee, M.; Walt, D. R. *Anal. Chem.* **2002**, *74*, 1836-1840.

(12) Hjelt, K. T.; van den Doel, R. ; Lubking, W.; Vellekoop, M. J. *Sens. Actuators, A* **2000**, *85*, 384-389.

(13) Crofcheck, C. L.; Grosvenor, A. L.; Anderson, K. W.; Lumpp, J. K.; Scott, D. L.; Daunert, S. *Anal. Chem.* **1997**, *69*, 4768-4772.

(14) Jackman, R. J.; Duffy, D. C.; Ostuni, E.; Willmore, N. D.; Whitesides, G. M. *Anal. Chem.* **1998**, *70*, 2280-2287.

(15) Hyun, J.; Chilkoti, A. *J. Am. Chem. Soc.* **2001**, *123*, 6943-6944.

(16) Clark, R. A.; Hietpas, P. B.; Ewing, A. G. *Anal. Chem.* **1997**, *69*, 259-263.

(17) Clark, R. A.; Ewing, A. G. *Anal. Chem.* **1998**, *70*, 1119-1125.

(18) Yan, M.; Bartlett, M. A. *Nano Lett.* **2002**, *2*, 275-278.

(19) Iler, R. K. *J. Colloid Interface Sci.* **1966**, *21*, 569-594.

(20) Fendler, J. H. *Chem. Mater.* **1996**, *8*, 1616-1624.

(21) Serizawa, T.; Takeshita, H.; Akashi, M. *Langmuir* **1998**, *14*, 4088-4094.

(22) Dokoutchaev, A.; James, J. T.; Koene, S. C.; Pathak, S.; Prakash, G. K. S.; Thompson, M. E. *Chem. Mater.* **1999**, *11*, 2389-2399.

(23) Caruso, F.; Möhwald, H. *Langmuir* **1999**, *15*, 8276-8281.

(24) Musick, M. D.; Keating, C. D.; Lyon, L. A.; Botsko, S. L.; Peña, D. J.; Holliway, W. D.; McEvoy, T. M.; Richardson, J. N.; Natan, M. J. *Chem. Mater.* **2000**, *12*, 2869-2881.

(25) Mamedov, A. A.; Kotov, N. A. *Langmuir* **2000**, *16*, 5530-5533.

(26) Chen, K. M.; Jiang, X.; Kimerling, L. C.; Hammond, P. T. *Langmuir* **2000**, *16*, 7825-4834.

(27) Bliznyuk, V. N.; Tsukruk, V. V. *Polym. Prepr.* **1997**, *38*, 963-964.

(28) Fulda, K.-U.; Kampes, A.; Krasemann, L.; Tieke, B. *Thin Solid Films* **1998**, 752-757.

(29) Bliznyuk, V. N.; Campbell, A.; Tsukruk, V. V. *Organized Multilayer Films of Charged Organic Latexes*; Frank, C. W., Ed.; American Chemical Society: Washington, DC, 1998; Vol. 695, pp 220-232.

(30) We note that under these pH conditions the carboxyl groups are largely protonated. However, flocculation tests confirmed that both nanoparticle dispersions were stable in the deposition solution for several hours.

(31) Domina, D., Interfacial Dynamics Corporation, Personal Communication.

(32) Odian, G. *Principles of Polymerization*; Third ed.; John Wiley & Sons, Inc.: New York, 1991, pp 335-355.

(33) This procedure has also been used successfully with glass, quartz, and gold substrates.

(34) Carim, A. H.; Dovek, M. M.; Quate, C. F.; Sinclair, R.; Vorst, C. *Science* **1987**, *237*, 630-633.

(35) Wasserman, S. R.; Tao, Y.-T.; Whitesides, G. M. *Langmuir* **1989**, *5*, 1074-1087.

(36) Zhong, Z.; Gates, B.; Xia, Y.; Qin, D. *Langmuir* **2000**, *16*, 10369-10375.

(37) Grisaru, H.; Cohen, Y.; Aurbach, D.; Sukenik, C. N. *Langmuir* **2001**, *17*, 1608-1619.

(38) Madou, M. J. *Fundamentals of Microfabrication*; CRC Press LLC: Boca Raton, 1997.

(39) Negatively charged 60 nm aldehdye/sulfate-modified polystyrene nanoparticles were also tested and yielded similar results.

(40) Control studies that attempted to create multiple layers of the same polymeric nanoparticle yielded only single particle layers, indicating that the deposition mechanism is initiated by an electrostatic attraction and not a hydrophobic interaction.

(41) The light source was a 200-W, medium-pressure mercury lamp (Oriel). The beam was collimated, reflected off an air-cooled, dichroic mirror (200-260 nm), and focused by a fused-silica lens.

(42) Ranby, B.; Rabek, J. F. *Photodegradation, Photo-oxidation and Photostabilization of Polymers*; John Wiley & Sons: London, 1975.

(43) Kuzina, S. I.; Mikhailov, A. I. *Eur. Polym. J.* **1998**, *34*, 1157-1162.

(44) A MultiMode NanoScope IIIa SFM (Digital Instruments) equipped with a recently calibrated 150 μm tube scanner was operated in Tapping Mode under ambient conditions for all measurements.

(45) Optical and fluorescent microscopy images were acquired using an Olympus BX50WI epi fluorescence microscope equipped with a DC-330 3CCD color camera (Dage-MTI) and a mercury light source. All fluorescence images were collected using a 51004v2 filter set (excitation BP: 475-492.5 nm, 545-565 nm; emission BP: 503-533 nm, 582-622 nm (Chroma Technology Corp.)).

(46) Askeland, D. R. *The Science and Engineering of Materials*; Third ed.; PWS Publishing Company: Boston, 1994.

(47) Immersion studies in 0.1 M NaOH were carried out on a gold substrate since NaOH is a known silicon etchant.

(48) Israelachvili, J. N. *Intermolecular and Surface Forces*; Second ed.; Academic Press: London, 1992.

(49) For polystyrene, the glass transition temperature (T_g) is 100 ^oC and its melting point (T_m) is 240-250 ^oC.

(50) Schrader, D. *Physical Constants of Poly(styrene)*; Fourth ed.; Brandrup, J., Immergut, E. H. and Grulk, E. A., Ed.; John Wiley & Sons, Inc.: New York, 1999, pp V91-V94.

Figure Captions

Scheme 1: Procedure for the construction of microwell arrays by combining multilayer nanoparticle deposition and photolithography.

Figure 1: AFM image (2.50 x 2.50 μm) and cross-sectional topographic plot for a layer of AMPNs deposited on a silicon substrate.

Figure 2. AFM image (80 x 80 μm) and cross-sectional topographic plot of a well array prepared by photopatterning a three layer coating of nanoparticles (AMPN/CMPN/AMPN) with a micromesh-type photomask.

Figure 3: OM images of a photopatterned array of microwells prepared in a three-layer coating of nanoparticles (AMPN/CMPN/AMPN). (A) Image of the entire microstructure (see text for details); (B) 10x image; (C) 100x image.

Figure 4: Plots of the (A) theoretically predicted well depth for a closest packed, ABA structure of 60-nm particles (dashed line, slope = 48.9 nm/layer); (B) experimentally determined well depth (solid line, bars represent standard deviation, 54 samples/layer, slope = 35.3 nm/layer (r^2=0.995)); and (C) experimentally determined well depth after thermal processing (18 samples/layer, error bar size is of the same magnitude as the data symbol) as a function of the number of nanoparticle layers. The even-numbered layers have CMPNs as the topmost layer, and the odd-numbered layers have AMPNs as the topmost layer.

Figure 5: AFM image (80 x 80 μm) and topographic cross sectional plot of thermally processed well array prepared using a four-layer nanoparticle coating (AMPN/CMPN/AMPN/CMPN) on silicon.

Figure 6: OM images of neighboring three layer nanoparticle coating (AMPN/CMPN/AMPN) wells filled with alternating 58% glycerin/water solutions of 10 ppm Rhodamine 110 and 10 ppm Rhodamine B: (A) bright field image; (B) fluorescent image.

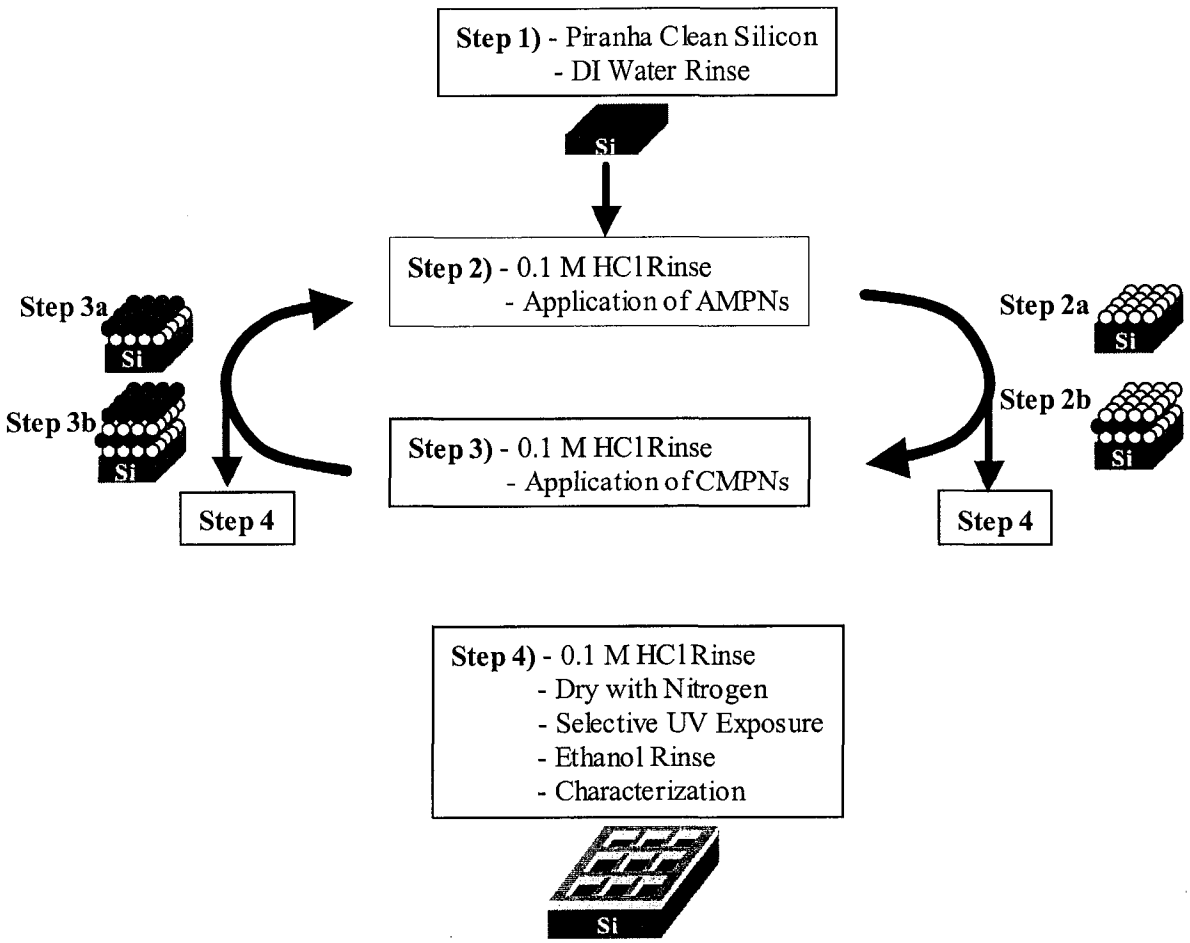
Step 1) - Piranha Clean Silicon
- DI Water Rinse
Si
Step 2) - 0.1 M HCl Rinse
- Application of AMPNs
Step 2a
Si
Step 2b
Si
Step 3a
Si
Step 3b
Si
Step 3) - 0.1 M HCl Rinse
- Application of CMPNs
Step 4
Step 4
Step 4) - 0.1 M HCl Rinse
- Dry with Nitrogen
- Selective UV Exposure
- Ethanol Rinse
- Characterization
Si

Scheme 1

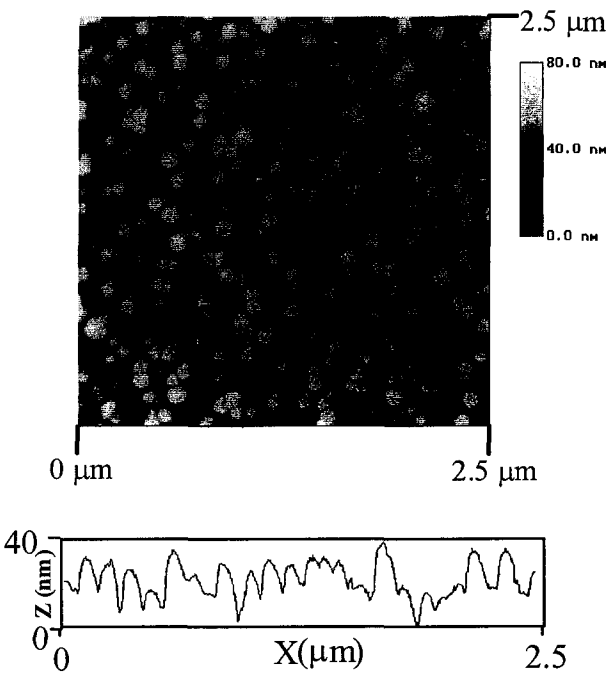

Figure 1

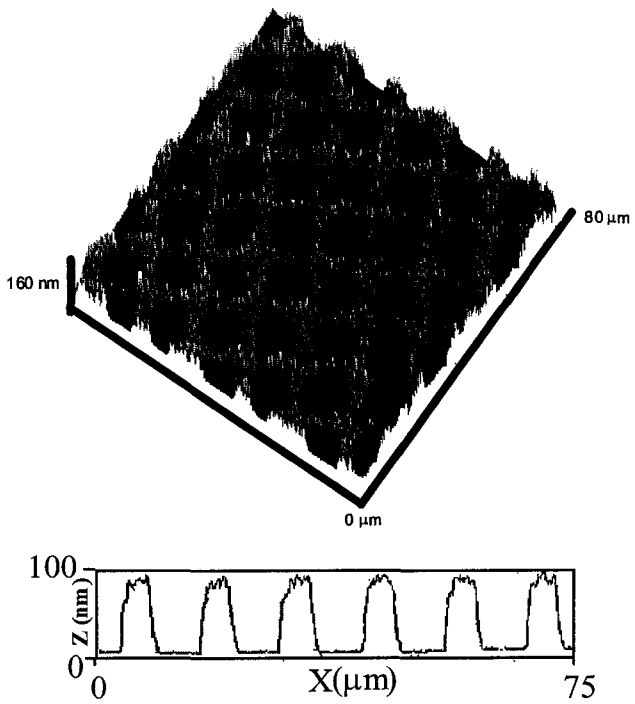

Figure 2

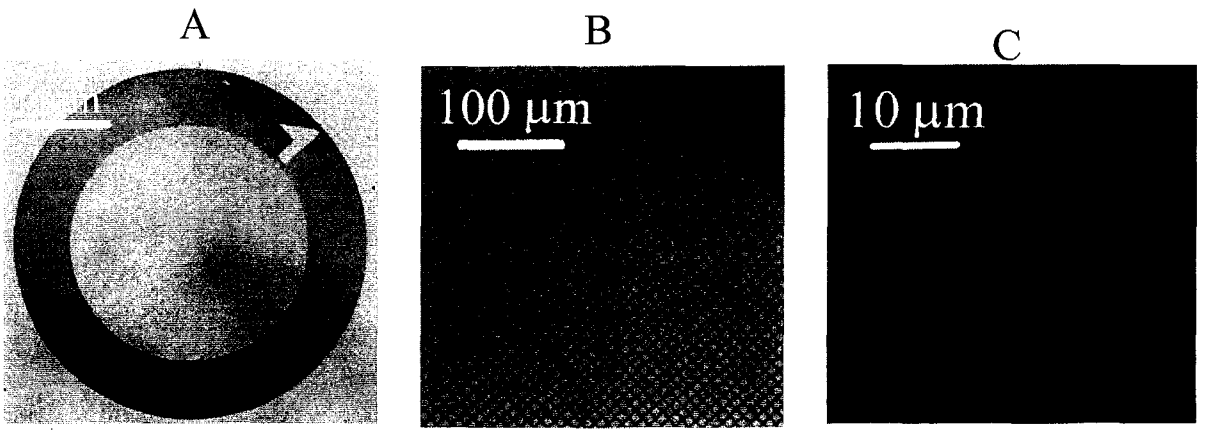

Figure 3

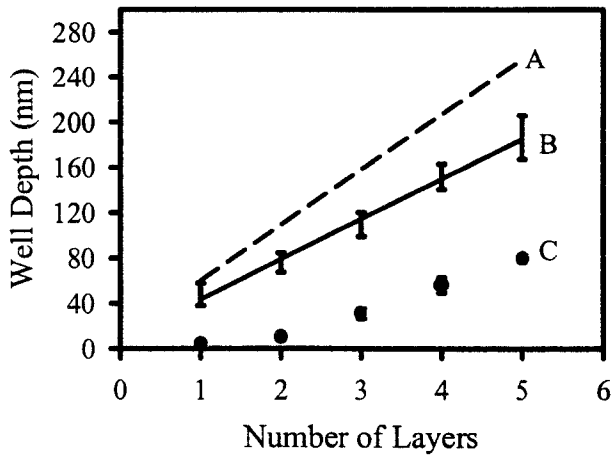
280
240
200
160
120
80
40
0
Well Depth (nm)
A
B
C
0
1
2
3
4
5
6
Number of Layers

Figure 4

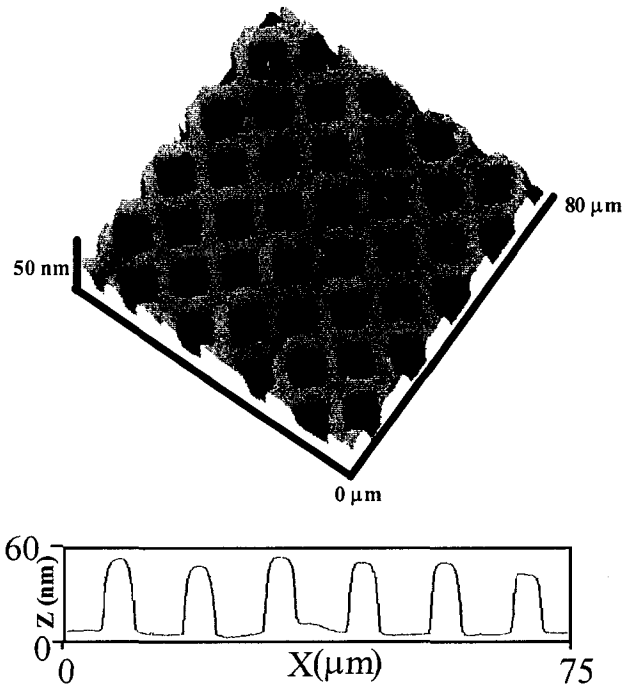

Figure 5

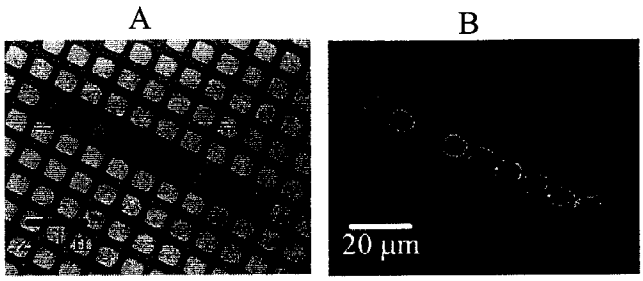

Figure 6

CHAPTER 3: SUBPICOLITER VOLUME WELL ARRAY CREATED FROM THE LAYER-BY-LAYER DEPOSITION OF POLYMERIC NANOPARTICLES: TOWARDS A MINIATURIZED, HIGH-THROUGHPUT SCREENING PLATFORM

Andrew D. Pris[1] and Marc D. Porter[1,2]

Abstract

This paper describes the conceptual usage of a massively dense array of subpicoliter volume elements, created through the layer-by-layer deposition, thermal processing, and photopatterning of polymeric nanoparticles, as a micro-chemical reactor and as a biorecognition platform. Through the ability to selectively address individual volume elements, in combination with the facile construction and structural flexibility of the platform, this platform has clear potential for use in high-throughput screening (HTS). This capability is demonstrated by completing schemes within individual wells that vary in complexity from simple chemical reactions (i.e., acid-base chemistry) to complex biorecognition (i.e., immunoassays). The advantages of utilizing this miniaturized platform and future prospects are also briefly discussed.

Introduction

Miniaturized analytical array test platforms for high-throughput screening (HTS) is of major importance to the pharmaceutical, catalytic, genomic, and proteomic arenas.[1-5] In many instances, HTS relies on the fabrication of a massive array of individually

[1] Microanalytical Instrumentation Center, Ames Laboratory-USDOE, and Department of Chemistry, Iowa State University, Ames, IA 50011
[2] Corresponding Author

programmable addresses laid out in a patterned spatial configuration. There are two extremes in the general strategy for array construction. One extreme builds arrays by employing parallel processing techniques (e.g., microfluidic channel deposition of materials,[6,7] electrospray,[8] robotic contact printing,[9-13] screen printing[14]). This approach, however, comes at the cost of creating large sized (e.g., micrometer length scales) array elements with fairly inflexible fabrication protocols.

The other extreme focuses on the construction of extremely small (e.g., nanometer length scales) array elements in order to markedly enhance address density. These ultra small elements are created through a variety of techniques, including mixed monolayer deposition,[15,16] photopatterning monolayers,[17-20] micro-contact printing of monolayers or proteins,[21,22] particle lithography,[23,24] mechanical manipulation (i.e., scrapping),[25-27] or direct placement (e.g., dip-pen lithography) of monolayers.[28] These approaches, although yielding extremely small address sizes, are often restrictively serial and / or complex in their preparation. As a result, the number of analytes (e.g., antigens) that the array targets are usually smaller then that available using more macroscopic constructs.

To combine the best of both extremes, several novel miniaturized bioarray design concepts have recently emerged, that serve as representative examples. These concepts create array elements that posses sub-micrometer dimensions and are capable of localizing and isolating subpicoliter volumes. These microwells have been fabricated through a variety of processes, including wet[29-36] and dry[37] chemical etching as well as micromolding.[38-41] Moreover, these microwells allow for: 1) confinement and isolation of extremely low sample volumes; and 2) interrogation of individual array elements. This microwell concept and associated advantages have been utilized to monitor a variety of biological processes

including cellular[42-45] and enzymatic[29] production of dilute analytes as well as genomic[35] and proteinaceous biorecognition.[46-50]

We have recently described a unique way to create ultradense sub-micrometer well arrays with femtoliter volumes through a "bottom-up" fabrication process.[51] Our procedure draws upon the layer-by-layer deposition of oppositely charged polymeric nanoparticles that is then coupled with photolithographic development and an optional thermal processing step. This extremely facile preparative method provides a means to obtain a variety of quantized well dimensions based upon the choice of nanoparticle size to define the well depth and photomask to select the lateral dimensions of the well. Due to the flexibility of this procedure these test platforms have potential use in HTS studies. In this paper, we first describe the ability of this novel massively dense array platform to discretely localize and isolate reaction components and products of a simple acid-base reaction. We then extend upon this through depicting a proof-of-concept biorecognition assay in which antigens are addressed into specific array elements in a desired pattern. The specific antigens are then successfully labeled and visualized within the proper array address. Combined, these studies implicate the HTS potential of this ultra-dense platform.

Experimental Section

Microwell Fabrication

The preparation of these densely packed microarrays has been previously described.[51] Briefly, a 1 cm x 1 cm silicon (111) substrate (Montco Silicon)[52,53] is cleaned in a freshly prepared peroxysulfuric acid solution (3:1 H_2SO_4 (Fisher):30% H_2O_2(Fisher)) (**Caution: "Piranha" is a strongly oxidizing solution and should be handled with extreme care**).

The substrate is then immediately and extensively rinsed with distilled, deionized water (Millipore), noting that a thin layer of retained rinse solution prevents adsorption of adventitious materials between each step in the fabrication procedure.

The layer-by-layer cyclic deposition process of the nanoparticle begins by rinsing the substrate with a 0.1 M HCl (Fisher) aqueous solution. To the retained rinse layer, 200 μL of the as received positively charged 60-nm amidine-modified polymeric nanoparticles (AMPN, Interfacial Dynamics Corp., 4% dispersion, 53 ± 8 nm) was pipetted into the retained layer of rinse solution upon the substrate,[54] allowed to stand for 20 min, and then removed by rinsing with 0.1 M HCl. This step yields a single densely packed, but disordered, monolayer of nanoparticles.[51] If structures possessing increased heights were desired the deposition cycle was continued by pipetting 200 μL of the negatively charged 60-nm carboxylate modified latex nanoparticles (CMLN, Interfacial Dynamics Corp., 4% dispersion, 63 ± 5 nm) onto the substrate.[55] Again this was allowed to sit for 20 min before rinsing with the 0.1 M HCl resulting in a two-layered film upon our substrate.[56,57] If increased heights were desired, this sequential repetition of the AMPN and CMLN was continued and resulted in a controlled, layer-by-layer increase of particle layers. Once the desired height was achieved, the sample was rinsed with 0.1 M HCl and dried with a directed stream of nitrogen (Air Products).

The substrate is next masked with a 2000 mesh TEM grid (7.5 μm holes, 5 μm bars, Electron Microscopy Sciences), and exposed for 40 min to UV light from a 200 W, medium-pressure mercury lamp (Oriel) that was collimated and reflected off of an air-cooled, dichroic mirror (200-260 nm) and focused by a fused-silica lens. The UV irradiation degrades the polymeric film within the exposed regions through a photo-oxidation mechanism that is only partially understood.[58,59] After irradiation, the sample was rinsed with ethanol (Aaper, USP

grade) that exposes an array of volume elements in which the structure depth is defined by the number of particle layers and whose lateral dimensions are controlled by the photomask.

An optional thermal processing step can also be taken which involved placing the substrate into an annealing oven at 230°C for 75 min.[60,61] This process controllably reduced the vertical height of the structure without compromising the lateral integrity. With this process, in which only 60-nm sized particles were used, massively dense array (~650,000 wells/cm^2) of ordered volume elements were created with height increments varying between 4-180 nm depending upon the number of layers deposited. More important to this study however is that the volumes of these wells were controllably varied between 3-15 fL.

Instrumentation

Atomic Force Microscopy (AFM) AFM structural characterizations were completed with a Multimode Nanoscope IIIa SFM (Digital Instruments) equipped with a recently calibrated 150-μm tube scanner. All images were obtained under ambient conditions in tapping mode with a 124-μm silicon cantilever/tip (Nanosensors). The set point amplitude of the cantilever was set to 80% of the free oscillation amplitude and maintained by the feedback circuitry of the instrument, leading to a F_N of ~10^{-9} N.

Epi-fluorescence Microscopy Bright field and fluorescence images were acquired using an Olympus BX5OWI epi-fluorescence microscope equipped with either a SenSys 1400 digital camera (Photometrix) or a DC-330 3CCD color camera (Dage-MTI). All images were taken with a mercury light source for excitation and with a 51004v2 filter set

(excitation BP: 475-492.5 nm, 545-565 nm; emission BP: 503-533 nm, 562-622 nm)(Chroma Technology Corp.) for fluorescence mapping.

Well-Addressing Hardware and Procedure

The microwell array was mounted on a Peltier cooler (Model AC-9550C, ILX Lightware) and was then positioned under the objective of the optical microscope. The temperature of the cooler was maintained 1°C above the calculated dew point by a thermoelectric controller (Model TC-5100, Seastar Optics Inc.). Under these conditions, solutions placed within the wells were stable 6 h or longer.

Micropipettes with sub-micron diameter tips were created with a glass microelectrode puller (Model PP-830, Narishige) from thin-walled, single-barrel, inner-filament, borosilicate glass capillaries (World Precision Instruments). After filling with solution, the micropipettes were directed to the array address with a three-dimensional micromanipulator (Model MMO-202, Narishige). Solutions were drawn into the address through capillary action by gently touching the solution extending from the end of the micropipette to the underlying substrate. This simple filling procedure leads to a solution volume of approximately 1.0 pL or less.

Acid-Base Reaction Scheme

Using two separate sets of micropipettes and micromanipulators, two rows of wells were filled with an aqueous solution of 0.05 M NaOH (Fisher) with 50% glycerin (Fisher),[36] or with 10 ppm resorufin (Aldrich) in a 50:50 glycerin: water (pH 5.5) solution. The micropipette containing the 0.05 M NaOH/glycerin solution then re-addressed the solutions

in one of the rows of wells containing the 10 ppm resorufin. Fluorescent and bright field images were captured utilizing the Photometrix camera with a 5 s integration time.

Immunoassay Procedure

Absorption of the antigen onto the sidewalls of the microwells proceeded by creating a 20 μg/mL solution of either whole polyclonal rabbit IgG (Pierce) or whole polyclonal mouse IgG (Pierce) within an adsorption buffer. The adsorption buffer consisted of 50 mM sodium borate (pH 9.0) (Fisher) with 1% (v/v) Tween-80 (Aldrich) and 0.02% sodium azide (Sigma). To this adsorption buffer 50% (v/v) glycerin was added to reduce the rate of evaporation of the subpicoliter volumes in the individual wells.[36] An antigen solution was then loaded into a pulled micropipette and addressed into the designated microwells as described above. Baseline bright field and fluorescent images (~1 s integration time) were taken with the DC-330 3CCD color camera. The antigen solutions were allowed to stand in the addressed wells for 90 min at which point the entire chip was vigorously rinsed with the adsorption buffer and placed into a well of a standard 24-well polystyrene titer plate (Corning Inc.) containing 3 mL of the adsorption buffer. This 3 mL of adsorption buffer was gradually exchanged out to 3 mL of blocking buffer through a 5x volume exchange. The blocking buffer consisted of 50 mM sodium phosphate (Fisher) (pH 7.4) containing 3% (w/w) bovine serum albumin (BSA, Sigma), 0.01% (v/v) Tween-80, and 10 mM sodium azide. The chip was allowed to sit in the blocking buffer for 14 h. After this blocking period, the solution over the chip was again slowly exchanged out through a 5x volume exchange to 3 mL of labeling buffer that was composed of 50 mM sodium phosphate (pH 7.4) with 1% (w/w) BSA and 10 mM sodium azide.

The labeling antibody solution was created in a darkened room by placing Alexa Fluor 568 goat anti-mouse IgG (H+L) (Molecular Probes) and Alexa Fluor 488 goat anti-rabbit IgG (H+L) (Molecular Probes), each at a concentration of 0.1 mg/mL, into 3 mL of the labeling buffer. The labeling antibody solution was placed into a well of the 24-well titer plate and the chip was moved into this well. The plate was wrapped in aluminum foil and held in a dark room for 5 h. After this time, within a dark room, the 3 mL of labeling antibody solution was gradually exchanged out to 3 mL of the labeling buffer through a 5x volume exchange. This was in turn exchanged out to 3 mL of distilled, deionized water. The chip containing the addressed microwells was then removed from the titer plate, extensively rinsed with deionized water, and dried with a stream of nitrogen. The chip was then imaged in both bright field and fluorescent (~0.5 s integration time) modes within a dark room with the epi-fluorescent microscope and the DC-330 3CCD color camera as described above.

Results and Discussion

Characteristics of Microwell Array

Characterization of this potential HTS array of microwell elements has been described in a recent report.[51] Atomic force microscopy (AFM) was utilized to show that this facile preparatory route yields robust structures with great reproducibility as shown in Figure 1. Moreover, this method allows for a great amount of design flexibility in all three dimensions. The height of the structures can be easily controlled at the nanometer level not only through the manipulation of the number of nanoparticle layers and size of nanoparticles, but also by utilizing a thermal processing step. The lateral dimensions of the platform are manipulated through the choice of photomask. This attribute yields a large number of

possible permutations in platform design by drawing on the extensive amount of literature in the photolithographic arena. Our earlier report demonstrated that these structures could isolate liquids localized within individual volume elements and restrict mixing between adjacent wells. Herein, we draw upon these characteristics and utilize this procedure to create a chip that possesses uniform elements of controlled volume at a density nearing 650,000 wells/cm^2.

Simple Reaction in a Well: Acid-Base Reaction Scheme

As a starting point for assessment of the viability for preforming a HTS assay with our well array, a simple acid-base reaction study was performed using the fluorescent dye resorufin. Resorufin is a well characterized fluorescent dye that has been used to monitor a range of enzymatic reactions.[62-64] Its optical properties are strongly pH dependent (pK_a~8.0). Upon protonation, the absorption maximum shifts from ~560 nm to ~480 nm.[65] Protonation also results in a marked drop in the fluorescent quantum yield, providing a useful marker for qualitatively testing the use of our well arrays in a simple chemical reaction scheme.

This test was carried out by selectively filling a small number of volume elements. Two rows of a microwell array platform were specifically addressed with a pH 5.5 solution of resorufin while two other rows immediately to the right of the previously labeled wells were addressed with a 0.05 M NaOH solution. Figure 2A shows an optical image of the results of this step. The fluorescent intensity of both solutions is minimal (Figure 2B) until the micropipette containing the 0.05 M NaOH is again used to address the top row of volume elements containing resorufin. Aside from the volumes in the top row on the left hand side appearing slightly larger, the bright field image (Figure 2C) shows no change after this

second addressing step. The fluorescent image (Figure 2D) however depicts a marked change within the wells containing the combination of resorufin and NaOH. Only when both of these components are present does the resorufin molecule undergo deprotonation resulting in the increased fluorescent quantum yield and fluorescent intensity.

Immunoassay Within Selected Volume Elements

One particular advantage to utilizing this microwell array for immuno-diagnostic events is that these particular microwell walls are composed of polystyrene. Many standard immunoassays protocols have been developed for use in the commonly used polystyrene titer plates.[66] Because of this, we can employ these procedures and apply it toward our unique volume element platform. Figure 3 depicts the overall immunoassay concept from the vantage point of a single volume element (Figure 3A). An antigen of interest is specifically placed into a selected well (Figure 3B) and adsorbed onto the walls of the microwell (Figure 3C). Following this adsorption step is a blocking protocol with BSA (Figure 3D).[66] This procedure is meant to saturate all other sites capable of non-specific adsorption with BSA, thus rendering all unlabeled regions, and volume elements, immunologically inactive. As a result of this blocking step, when the labeling antibodies are exposed to the chip, they cannot adsorb non-specifically to the hydrophobic polystyrene as BSA is now occupying all of these sites. The labeling antibodies will thus only bind to the platform due to specific antigen/antibody interactions and not as a result of non-specific adsorption (Figure 3E).

The immunoassay within the volume well array begins with the selective deposition of the antigens. Figure 4A depicts the placement of the rabbit IgG antigen with a micropipette in the design of an "R" and as part of a registry number "3". Figure 4C shows

the labeling of adjacent volume elements with mouse IgG in the shape of an "M" and completion of the registry number "3". As can be seen in both Figures 4B and 4D, these solutions have no detectable fluorescence upon the green fluorescent background that appears due to the high number of integrations used to fully document the fluorescent background.[67]

Figure 5A depicts the bright field image of the addressed volume elements after the completion of the immunoassay procedure. As can be seen, the labeling procedure has left no indications of which wells were specifically labeled within the bright field. This situation, however, is changed by observing the fluorescent images in Figure 5B in which specific labeling of the rabbit IgG is marked by the green fluorescence of the Alexa Fluor 488 goat anti-rabbit IgG and the mouse IgG volume elements are successfully labeled with the red fluorescence of the Alexa Fluor 568 goat anti-mouse IgG. Figure 6A and 6B display higher magnification images of the "M", "R", and "3" to show the successful labeling and addressing of the desired volume elements. Moreover, only those wells specifically addressed show a detectable fluorescence, indicating the successful isolation of antigens within the designated volume elements as well as the successful blocking of the un-labeled wells in the array. Blank studies (not shown) in which the antigenic solution was created without antigen and was pipetted into individual microwells possessed no change in fluorescence following the labeling step. This result also indicates a successful bio-specific recognition process.

Conclusions

The successful proof-of-concept results are extremely encouraging when considering this microwell array methodology for a HTS platform. Further impetus to pursue this platform for HTS experiments is provided by the combination of the design flexibility of this platform with the material choice of polystyrene, for which many experimental protocols have been published. Research in progress further addresses the usage of this platform for HTS experiments through the usage of microchannels within PDMS. This would not only increase the parallel nature in which the individual volume elements could be accessed but also allow for the possibility of utilizing the wells as a downstream sampling mechanism for separations performed within the microchannel for a combinatorial chemistry application. This and other work in biological and catalytic assay schemes continue with our laboratories.

Acknowledgements

A.D.P. expresses appreciation for a Phillips Petroleum Company Research Fellowship. This work was also supported by the Office of Basic Energy Research, Chemical Sciences Division, U.S. Department of Energy and by the Microanalytical Instrumentation Center of Iowa State University through the W. M. Keck Laboratory for the Fabrication of Microminiaturized Analytical Instrumentation. The Ames Laboratory is operated for the U.S. Department of Energy by Iowa State University under Contract W-7405-Eng-82.

References and Notes

(1) Khandurina, J.; Guttman, A. *Curr. Opin. Chem. Biol.* **2002**, *6*, 359-366.

(2) Templin, M. F.; Stoll, D.; Schrenk, M.; Traub, P. C.; Vöhringer, C. F.; Joos, T. O. *Trends Biotechnol.* **2002**, *20*, 160-166.

(3) Battersby, B. J.; Trau, M. *Trends Biotechnol.* **2002**, *20*, 167-173.

(4) Mayer, G.; Schober, A.; Köhler, J. M. *Reviews in Molecular Biotechnology* **2001**, *82*, 137-159.

(5) Morris, N. D.; Mallouk, T. E. *J. Am. Chem. Soc.* **2002**, *124*, 11114-11121.

(6) Lee, H. J.; Goodrich, T. T.; Corn, R. M. *Anal. Chem.* **2001**, *73*, 5525-5531.

(7) Bernard, A.; Michel, B.; Delamarche, E. *Anal. Chem.* **2001**, *73*, 8-12.

(8) Avseenko, N. V.; Morozova, T. Y.; Ataullakhanov, F. I.; Morozov, V. N. *Anal. Chem.* **2002**, *74*, 927-933.

(9) MacBeath, G.; Schreiber, S. L. *Science* **2000**, *289*, 1760-1763.

(10) Ng, H. T.; Fang, A.; Huang, L.; Li, S. F. Y. *Langmuir* **2002**, *18*, 6324-6329.

(11) Delehanty, J. B.; Ligler, F. S. *Anal. Chem.* **2002**, *74*, 5681-5687.

(12) Fang, Y.; Frutos, A. G.; Lahiri, J. *J. Am. Chem. Soc.* **2002**, *124*, 2394-2395.

(13) Korbel, G. A.; Lalic, G.; Shair, M. D. *J. Am. Chem. Soc.* **2001**, *123*, 361-362.

(14) Dequaire, M.; Heller, A. *Anal. Chem.* **2002**, *74*, 4370-4377.

(15) Hobara, D.; Imabayashi, S.-i.; Kakiuchi, T. *Nano Lett.* **2002**, *2*, 1021-1025.

(16) Dong, Y.; Shannon, C. *Anal. Chem.* **2000**, *72*, 2371-2376.

(17) Jones, V. W.; Kenseth, J. R.; Porter, M. D.; Mosher, C. L.; Henderson, E. *Anal. Chem.* **1998**, *70*, 1233-1241.

(18) O'Brien, J. C.; Jones, V. W.; Porter, M. D.; Mosher, C. L.; Henderson, E. *Anal. Chem.* **2000**, *72*, 703-710.

(19) O'Brien, J. C.; Stickney, J. T.; Porter, M. D. *Langmuir* **2000**, *16*, 9559-9567.

(20) O'Brien, J. C.; Stickney, J. T.; Porter, M. D. *J. Am. Chem. Soc.* **2000**, *122*, 5004-5005.

(21) Bernard, A.; Renault, J. P.; Michel, B.; Bosshard, H. R.; Delamarche, E. *Adv. Mater.* **2000**, *12*, 1067-1070.

(22) Inerowicz, H. D.; Howell, S.; Regnier, F. E.; Reifenberger, R. *Langmuir* **2002**, *18*, 5263-5268.

(23) Garno, J. C.; Amro, N. A.; Wadu-Mesthrige, K.; Liu, G.-Y. *Langmuir* **2002**, *18*, 8186-8192.

(24) Michel, R.; Reviakine, I.; Sutherland, D.; Fokas, C.; Csucs, G.; Danuser, G.; Spencer, N. D.; Textor, M. *Langmuir* **2002**, *18*, 8580-8586.

(25) Wadu-Mesthrige, K.; Xu, S.; Amro, N. A.; Liu, G.-y. *Langmuir* **1999**, *15*, 8580-8583.

(26) Kenseth, J. R.; Harnisch, J. A.; Jones, V. W.; Porter, M. D. *Langmuir* **2001**, *17*, 4105-4112.

(27) Zhou, D.; Sinniah, K.; Abell, C.; Rayment, T. *Langmuir* **2002**, *18*, 8278-8281.

(28) Ivanisevic, A.; Im, J.-H.; Lee, K.-B.; Park, S.-J.; Demers, L. M.; Watson, K. J.; Mirkin, C. A. *J. Am. Chem. Soc.* **2001**, *123*, 12424-12425.

(29) Tan, W.; Yeung, E. S. *Anal. Chem.* **1997**, *69*, 4242-4248.

(30) Ball, J. C.; Scott, D. L.; Lumpp, J. K.; Daunert, S.; Wang, J.; Bachas, L. G. *Anal. Chem.* **2000**, *72*, 497-501.

(31) Nagai, H.; Murakami, Y.; Morita, Y.; Yokoyama, K.; Tamiya, E. *Anal. Chem.* **2001**, *73*, 1043-1047.

(32) Pantano, P.; Walt, D. R. *Chem. Mater.* **1996**, *8*, 2832-2835.

(33) Dam, T. H.; Pantano, P. *Rev. Sci. Instrum.* **1999**, *70*, 3982-3986.

(34) Evans, U.; Colavita, P. E.; Doescher, M. S.; Schiza, M.; Myrick, M. L. *Nano Lett.* **2002**, *2*, 641-645.

(35) Epstein, J. R.; Lee, M.; Walt, D. R. *Anal. Chem.* **2002**, *74*, 1836-1840.

(36) Hjelt, K. T.; Doel, R. v. d.; Lubking, W.; Vellekoop, M. J. *Sens. Actuators, A* **2000**, *85*, 384-389.

(37) Crofcheck, C. L.; Grosvenor, A. L.; Anderson, K. W.; Lumpp, J. K.; Scott, D. L.; Daunert, S. *Anal. Chem.* **1997**, *69*, 4768-4772.

(38) Jackman, R. J.; Duffy, D. C.; Ostuni, E.; Willmore, N. D.; Whitesides, G. M. *Anal. Chem.* **1998**, *70*, 2280-2287.

(39) Hyun, J.; Chilkoti, A. *J. Am. Chem. Soc.* **2001**, *123*, 6943-6944.

(40) Clark, R. A.; Hietpas, P. B.; Ewing, A. G. *Anal. Chem.* **1997**, *69*, 259-263.

(41) Clark, R. A.; Ewing, A. G. *Anal. Chem.* **1998**, *70*, 1119-1125.

(42) Biran, I.; Walt, D. R. *Anal. Chem.* **2002**, *74*, 3046-6054.

(43) Yasukawa, T.; Glidle, A.; Cooper, J. M.; Matsue, T. *Anal. Chem.* **2002**, *74*, 5001-5008.

(44) Troyer, K. P.; Wightman, R. M. *Anal. Chem.* **2002**, *74*, 5370-5375.

(45) Ostuni, E.; Chen, C. S.; Ingber, D. E.; Whitesides, G. M. *Langmuir* **2001**, *17*, 2828-2834.

(46) Aguilar, Z. P.; Vandaveer, W. R., IV; Fritsch, I. *Anal. Chem.* **2002**, *74*, 3321-3329.

(47) Christodoulides, N.; Tran, M.; Floriano, P. N.; Rodriguez, M.; Goodey, A.; Ali, M.; Neikirk, D.; McDevitt, J. T. *Anal. Chem.* **2002**, *74*, 3030-3036.

(48) Yakovleva, J.; Davidsson, R.; Lobanova, A.; Bengtsson, M.; Eremin, S.; Laurell, T.; Emnéus, J. *Anal. Chem.* **2002**, *74*, 2994-3004.

(49) Schobel, U.; Coille, I.; Brecht, A.; Steinwand, M.; Gauglitz, G. *Anal. Chem.* **2001**, *73*, 5172-5179.

(50) Grosvenor, A. L.; Feltus, A.; Conover, R. C.; Daunert, S.; Anderson, K. W. *Anal. Chem.* **2000**, *73*, 2590-2594.

(51) Pris, A. D.; Porter, M. D. *Nano Lett.* **2002**, *2*, 1087-1091.

(52) Other substrates have been used including glass (Fisher), fused quartz (GM Associates), and gold.

(53) Gold substrates were prepared by cleaning the 1 cm x 1 cm silicon (111) substrate in an ultrasonic bath for 30 min in water and 30 min in methanol. Following washing, the substrates were dried with high-purity argon (Air Products) and placed into a vacuum evaporator (Edwards). The substrates were primed with the deposition of 15 nm chromium at 0.1 nm/s followed by 300 nm of gold (99.9% purity) at 0.3-0.4 nm/s. During the coating procedure, the pressure in the deposition chamber was ~8 x 10^{-6} Torr.

(54) All polymeric dispersions were tested and shown to be stable within the 0.1 M HCl solution for greater then 2 hours thus displaying their stability within acidic solutions.

(55) Negatively charged 60 nm aldehdye/sulfate-modified polystyrene nanoparticles were also tested and yielded similar results.

(56) Control studies that attempted to create multiple layers of the same polymeric nanoparticle yielded only single particle layers, indicating that the deposition

mechanism is initiated by an electrostatic attraction and not a hydrophobic interaction.

(57) We note that under these pH conditions the carboxyl groups are largely protonated. However, flocculation tests confirmed that both nanoparticle dispersions were stable in the deposition solution for several hours.

(58) Ranby, B.; Rabek, J. F. *Photodegradation, Photo-oxidation and Photostabilization of Polymers*; John Wiley & Sons: London, 1975.

(59) Kuzina, S. I.; Mikhailov, A. I. *Eur. Polym. J.* **1998**, *34*, 1157-1162.

(60) For polystyrene, the glass transition temperature (T_g) is 100 ^oC and its melting point (T_m) is 240-250 ^oC.

(61) Schrader, D. *Physical Constants of Poly(styrene)*; Fourth Ed. ed.; Brandrup, J., Immergut, E. H. and Grulk, E. A., Ed.; John Wiley & Sons, Inc.: New York, 1999, pp V91-V94.

(62) Hadd, A. G.; Raymond, D. E.; Halliwell, J. W.; Jacobson, S. C.; Ramsey, J. M. *Anal. Chem.* **1997**, *69*, 3407-3412.

(63) McElroy, K. E.; Bouchard, P. J.; Harpel, M. R.; Horiuchi, K. Y.; Rogers, K. C.; Murphy, D. J.; Chung, T. D. Y.; Copeland, R. A. *Anal. Biochem.* **2000**, *284*, 382-387.

(64) Schilling, E. A.; Kamholz, A. E.; Yager, P. *Anal. Chem.* **2002**, *74*, 1798-1804.

(65) Molecular Probes **2001**, *MP12213*.

(66) Diamandis, E. P.; Christopoulos, T. K. *Immunoassay*; Academic Press: San Diego, 1996.

(67) The walls of the microwells within these fluorescent images (Figure 4, 5, and 6) cannot be visualized as in Figure 2 due to the decrease in integration times as noted in the Experimental section.

Figure Captions

Figure 1: AFM image (50 x 50 μm) and topographic cross-section of a well array prepared with a five-layer coating of nanoparticles (AMPN / CMLN / AMPN / CMLN / AMPN), thermal processing, and a micromesh type photomask.

Figure 2: Deprotonation of resorufin. Bright field (A) and fluorescent (B) images of the microwell array containing 0.05 M NaOH in the two rows on the right and 10 ppm resorufin (pH 5.5) in the two rows on the left. Bright field (C) and fluorescent (D) images of the same microwell array after addition of 0.05 M NaOH to the top row (four elements) on the left.

Figure 3: Immunoassay scheme for a single volume element: pristine volume element (A); volume element addressed with antigen adsorption solution (B); antigen adsorbed to polystyrene of volume element (C); immunological blocking of microwell (D); successful biorecognition and subsequent fluorescent labeling of microwell (E). See text for details.

Figure 4: Bright field (A) and fluorescent (B) image of the initial deposition of the rabbit IgG antigen solution as an "R" and part of a "3" and the bright field (C) and fluorescent (D) image after the completion of the "3" and formation of an "M" with the mouse IgG antigen solution.

Figure 5: Bright field (A) and fluorescent (B) images of labeled microwells.

Figure 6: Higher magnification fluorescent images of labeled microwells.

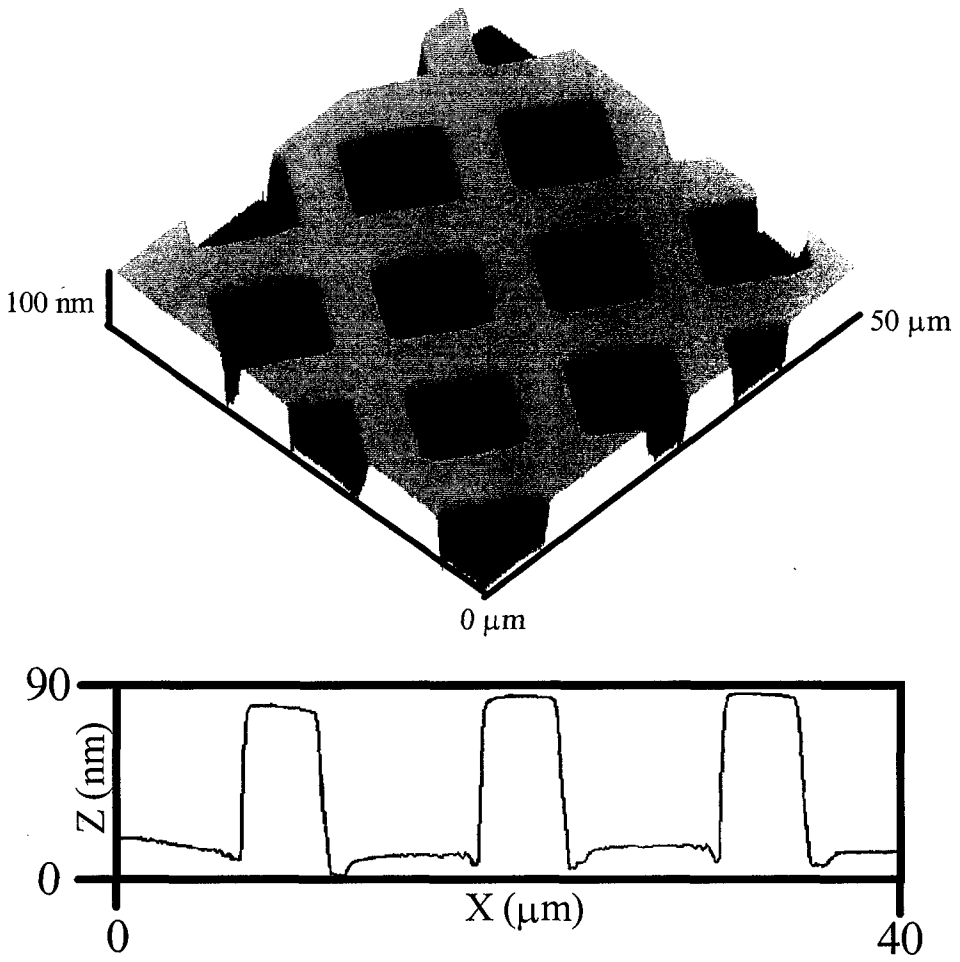

Figure 1

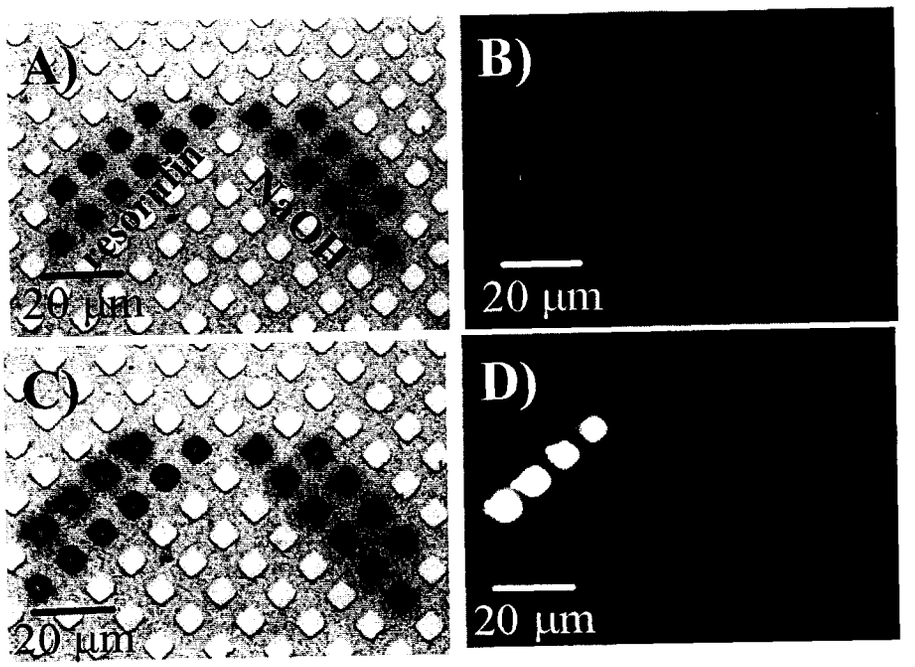

Figure 2

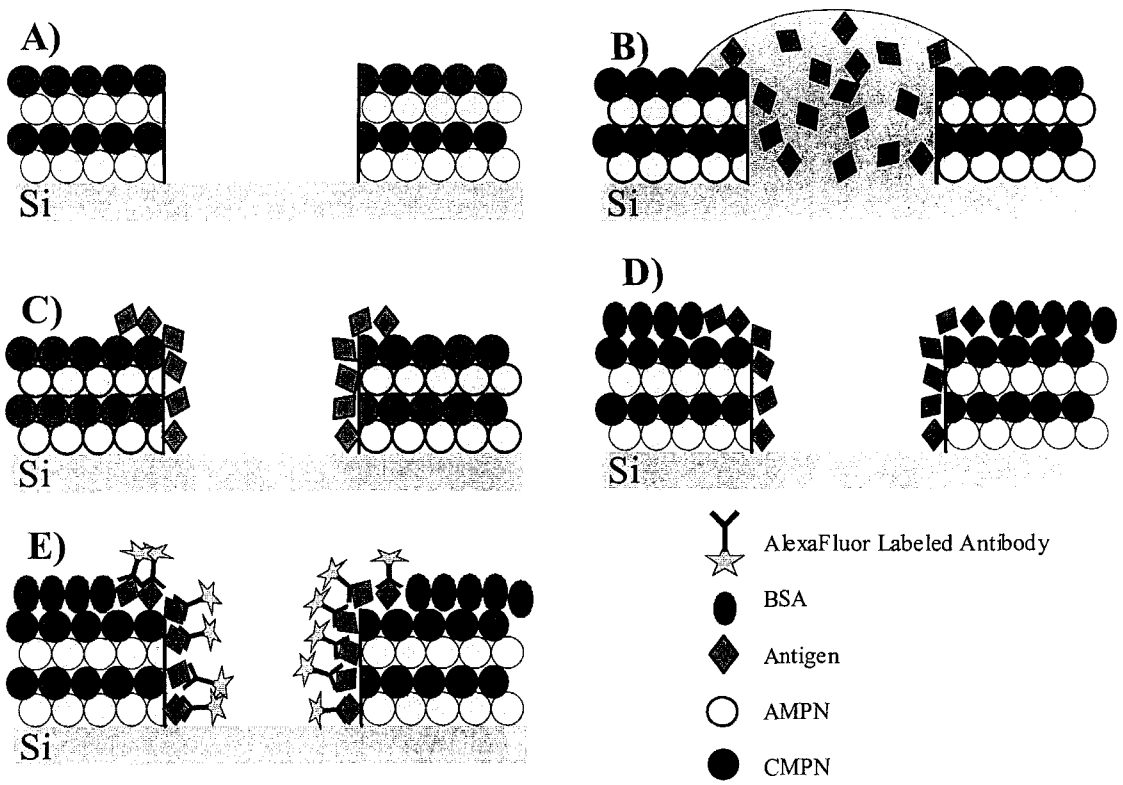
A)
Si
B)
Si
C)
Si
D)
Si
E)
Si
AlexaFluor Labeled Antibody
BSA
Antigen
AMPN
CMPN

Figure 3

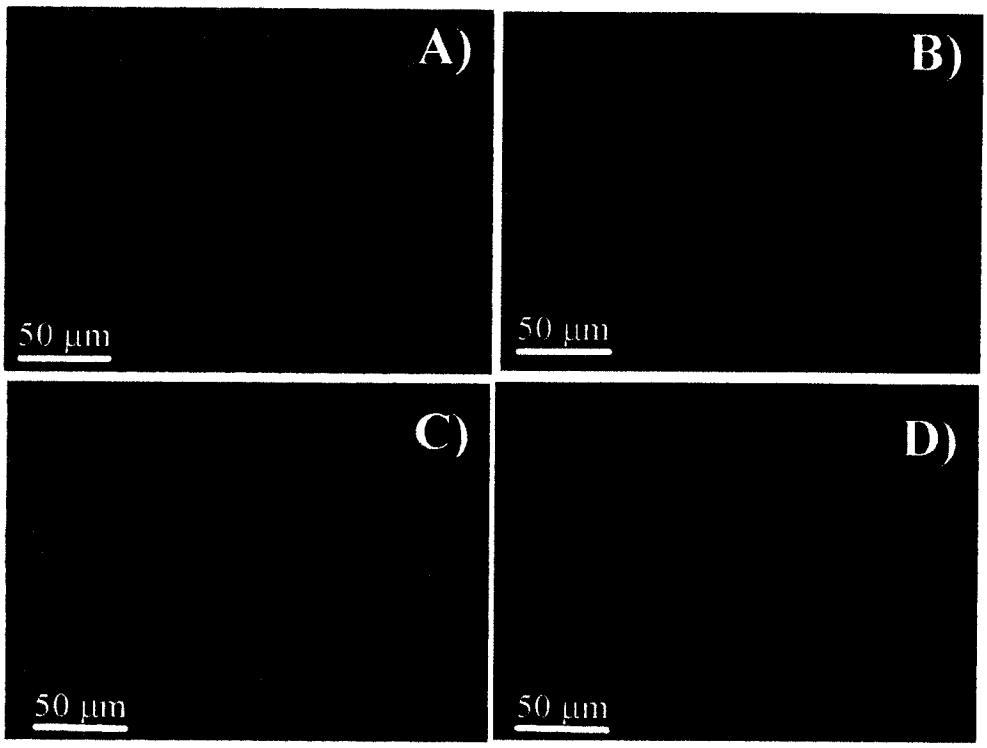

Figure 4

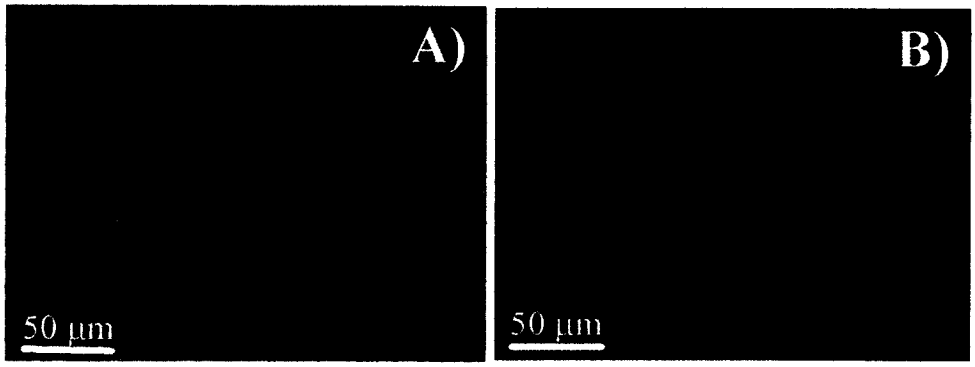

Figure 5

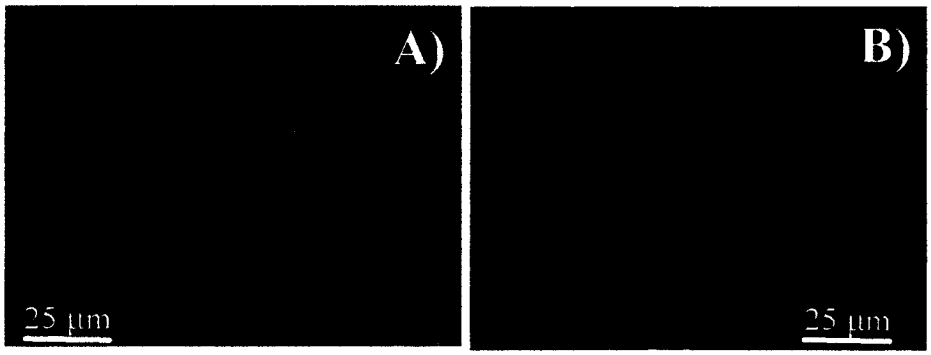

Figure 6

CHAPTER 4: TOWARDS A MULTIPLEXED SIZE-BASED, NANOPARTICLE "BAR-CODE" DIAGNOSTIC PLATFORM

Andrew D. Pris[1] and Marc D. Porter[1,2]

Abstract

Described herein are efforts toward creating a miniaturized, multiplexed assay platform. Through the unique combination of atomic force microscopy (AFM) size-based identification and the coupling of different sized substrate and labeling nanoparticles, a miniaturized "bar-code" diagnostic platform is developed. The choice of substrate nanoparticle, labeling nanoparticle, modification protocol, and read-out instrumentation is described along with the feasibility of the methodology. In a proof-of-concept experiment, the applicability of this scheme is demonstrated by exploiting the well-studied streptavidin-biotin interaction. In this case, AFM is capable of imaging 300-nm biotin modified silica substrate nanoparticles labeled with 10-nm streptavidin modified gold nanoparticles in the presence of 160-nm silica nanoparticles. With this successful demonstration, numerous potential applications of this concept are discussed.

Introduction

The quest to create versatile, high-density assay platforms is central to advances in a wide range of areas (e.g., disease detection, warfare agent monitoring, and combinatorial discovery). Through employment of an assortment of substrate preparation techniques (e.g.,

---

[1] Microanalytical Instrumentation Center, Ames Laboratory-USDOE, and Department of Chemistry, Iowa State University, Ames, IA 50011
[2] Corresponding Author

patterning of self assembled monolayers via photopatterning,[1-5] microfluidics,[6-9] microcontact printing,[10-12] jet ink printing,[13] or scanning probe microscopy [14-18]), arrays with address sizes ranging from a few hundred micrometers down to tens of nanometers have been created. These arrays are then coupled and interrogated by an equally diverse collection of read-out methodologies (e.g., fluorescence,[19,20] surface plasmon resonance,[21] optical microscopy,[20,22,23] and atomic force microscopy (AFM)[1-4,15]) for quantification of the presence of target analytes. One means to further reduce the required platform size for an assay is to consider the removal of the engineered substrate-patterning step. An alternative, yet elegant, route to obtain specific analyte responsive regions upon a substrate is to employ the self-assembly of nanometer-sized components.

A platform created from mixed thiol-monolayers on gold represents such an example of a self-assembled, multi-target, substrate.[24,25] However, the size and number of analyte-specific monolayer domains cannot necessarily be determined by the deposition solution concentration of the thiol. This situation complicates the ability to create a substrate with a known number and size of analyte active areas on the sensor platform, which is crucial to sample reproducibility and relating the read-out signal to absolute target analyte concentration.[24,25] As a means to control the quantity of nanometer-sized, analyte specific active regions on the analysis substrate, functionalized micro- and nanometer-sized particles, which still draw on the self-assembly process, have been used as operational bio-specific substrates.[26-38] The size of the active area against a specific analyte can be established by considering the size and number of nanoparticles admitted to the system. Moreover, the number of analytes that can be tested for is not limited by the particulate substrate but rather by the number of distinct read-out signals available since nanoparticles can be chemically

modified to be active against a near infinite number of analytes. One approach to increase the number of analyte specific transducer signals is to employ a combination of signals. This "bar-code" tactic has been demonstrated with fluorescent tags[27,31,39] as well as with distinctive patterns of gold and silver in a nanometer-sized rod.[22,23]

Our group has investigated the often-overlooked scheme of analyte identification, or coding, through labeling analytes with different sized nanoparticles and visualized them with AFM.[40] Particulate size-based identification can be extended towards increased number of analyte detection through application of the bar-coding principle. This multiplexed, biorecognition platform can be realized through employment of two nanoparticles: one larger particle, with dimensions of hundreds of nanometers, acts as an antigen-specific, biologically active substrate that can be self-assembled on a platform; and a second smaller particle (tens of nanometers) that operates as a tag whose presence indicates a positive assay. Likewise, as shown previously,[40] the number of smaller nanoparticle tags present determines the quantity of an antigen. The identity of the antigen is determined in this multiplexed system through the size of both the larger substrate nanoparticle and smaller labeling nanoparticle. Through careful design of the system, such that the presence of a smaller tag represents the presence of an analyte and the size combinations between the two nanoparticles identify the analyte, vast increases in the number of analytes that a single platform can detect is feasible. Demonstrated within this work are initial preparative and characterization protocols geared towards the creation of this multiplexed, size-readout "bar-code" assay. A proof-of-concept biotin-streptavidin, biorecognition scheme is also shown using the developed protocols.

Experimental Section

Silica nanoparticle dispersions were either purchased or synthesized. The purchased dispersions consisted of non-porous, primary amine modified silica particles (300 nm) and were obtained from MicroMod (MM, Rostcok, Germany). These particles (5.0% (w/w) aqueous dispersion, ~1.8 x 10^{12} particles/mL) were used as received. Molar concentrations of reactants for subsequent reaction schemes of all particles were calculated based upon the company provided amine surface concentration value for the MM particles, leading to an approximate value of 2.1 x 10^5 amine groups/particle. Nonporous silica particles (330 nm) were also amine derivatized in-house using dried products from Bangs Laboratories (Si, Fischer, IN). Amine functionalization of these nanoparticle surfaces was accomplished with an assortment of siloxane chemistries described below.

Amine Modification of Silica Nanoparticles

Acetic-Acid Modification

Using a method closely related to that of Tan and co-workers,[41] silanation of 1.0 mL of a 5.0% (w/w) aqueous dispersion of Si nanoparticles (~1.8 x 10^{12} particles/mL) with 5.0% (w/w) aminopropyl triethoxysilane (APTES, Aldrich) in 95% ethanol:water (Quantum) and 16 mM acetic acid (Fisher) was completed in a 1.5 mL polypropylene micro-centrifuge tube containing a micro-stir bar. This solution was vigorously stirred for 15 h. The stir bar was then removed and the suspension washed. Washing was achieved though centrifugation of the solution at 4000 rpm for 7 min, resulting in particle sedimentation. After removal of the supernatant, 1.0 mL of 16 mM acetic acid in ethanol was added to the centrifuge tube, and the nanoparticles were re-suspended via vortex mixing. This washing step was repeated

twice more and then the dispersed sample was divided into two aliquots to test the effects of a heat cure. The first fraction, designated AA1, was solvent exchanged to de-ionized water (18 mΩ, Millipore). This solvent exchange, or washing step, was achieved by centrifuging the suspended particles into a pellet, removing the supernatant, replacing the removed volume with de-ionized water, and re-suspending the particles with vortex mixing. The washing step was completed twice more. The second fraction, AA2, was cured for 3 h at 130°C in an atmospheric convection oven and then solvent exchanged, as with AA1, three times to de-ionized water. Both aliquots were stored at 4 °C until use.

Toluene Reflux

Following earlier reports,[42-45] approximately 200 mg of the as-received 330-nm silica nanoparticles were placed into a scrupulously clean, round bottomed flask. To this flask was added a stir bar and water condenser and the entire system was purged with dry N_2 for ~30 min. Next 2 mL of toluene (Fisher), dried over 4-Å molecular sieves (Fisher), was added to the N_2 purged system. The particles were dispersed within the toluene and 0.5 mL of APTES was added to the system. The mixture was then stirred for 2 h and refluxed for an additional hour. After cooling to room temperature, the contents of the flask were placed into a polypropylene centrifuge tube and the solvent exchanged as before to de-ionized water. The final dispersion, designated as TR, was stored at 4 °C until used.

Stöber Modification

Following the work of Halas et al.,[46] the classic silica particle formation protocol[47] was altered to act as a seeded growth functionalization. Approximately 200 mg of the 330-

nm silica particles were placed into a polypropylene centrifuge tube. To this, 1 mL of ethanol, dried over 4-Å molecular sieves, 60 mL of 30% ammonium hydroxide (Fisher), and a micro-stir bar was added. The particles were dispersed by the stir bar and 300 μL of APTES added to the dispersion. The dispersion was allowed to stir overnight and then the suspension matrix was volume exchanged to de-ionized water in a similar fashion to that above. The particles were dispersed in de-ionized water and stored at 4°C.

Characterization of the Primary Amine on the Functionalized Silica

2,3-napthalene dicarboxyaldehyde (NDA)

Employing a modified procedure used for the characterization of primary amines in amino acids,[48,49] a 1.0% (w/w) dispersion of the particles of interest was created in a 0.05 M borate buffer (pH 9.1). To this was added a 100x stoichiometric excess of aqueous KCN (Fisher) and a 100x stoichiometric excess of 2,3-napthalene dicarboxyaldehyde (NDA, Aldrich) dissolved in methanol. This solution was allowed to react for 30 min in order for the fluorophore to covalently attach to the amine groups on the particle surface. Following fluorophore attachment, the sample was washed three times through solvent exchange to de-ionized water. The fluorescence spectrum of the dispersion was collected on a SPEX Fluorolog 2-F112AI double monochromator Spectrofluorometer (Metuchen, NJ) equipped with a 450 W Xenon lamp. The excitation wavelength was set to 420 nm and the fluorescent emission was monitored between 440 and 600 nm.

The particles were further characterized by filtering the dispersions onto quantatative filter paper (Fisher, grade Q2) through a modified in house procedure.[50] Briefly, the particles were captured by cutting the filter paper into 13-mm disks that were subsequently mounted

into a plastic filter holder (Fisher, Sweinnex Filter Holder) and held in place by a 1.5-mm ring of two-sided tape affixed to the lower portion of the filter holder. The dispersion was passed through the filter via a Luer-locked syringe. The filter paper with the captured nanoparticles was air-dried and interrogated with a BYK-Gardner color-guide sphere d/8° spin diffuse reflection spectrometer (model PCB-6830). The diffuse reflectance spectrum of the sample was collected employing the integrated software of the spectrometer. The L*, a*, b* chromaticity characteristics, as defined by the Commission Internationale de l'Éclairage (CIE) for an observer at a 10° angle under a fluorescent light (F2), were obtained through manipulation of the diffuse reflectance spectra by the spectrometer software.

Fluorescamine

Using a procedure modified from Schroedter et al.,[51] a 1.0% (w/w) dispersion of the particles was formed in 900 μL of a 50 mM borate buffer (pH 9.1) which had been added to a 1.5 mL polypropylene centrifuge tube. A solution containing a 100x stoichiometric excess of fluorescamine (Aldrich) was prepared with acetone (Fisher) and a 100 μL aliquot was added to the dispersion. The components were allowed to react for 2 h, after which the particles were washed through a 3x volume exchange to de-ionized water. The fluorescence spectrum was acquired with an excitation wavelength of 380 nm and an emission wavelength scan between 390 and 600 nm.

Bio-modification of the Amine-modified Silica Nanoparticles

Biotinylation

Biotinylation was accomplished by conjugation of the amine groups on the silica surface through succinimidyl chemistry. A 50x stoichiometric excess of sulfo-succinimidyl-6'-(biotinamido)-6-hexanamido hexanoate (Pierce, EZ-link Sulfo-NHS-LC-LC-Biotin) was dissolved in 200 μL of dimethyl sulfoxide (DMSO, Fisher) in a polypropylene centrifuge tube. Subsequently, a stir bar, 600 μL of a 50 mM sodium bicarbonate buffer (pH 8.5), and 200 μL of the 5.0% dispersion of the MM amine-modified particles were added to the tube. The contents were stirred and allowed to react overnight at room temperature. The particles were then washed through a three-time volume exchange to de-ionized water. The final dispersion was stored at 4°C.

The presence of immobilized biotin was directly confirmed through fluorescence spectroscopy. A 0.1 mg/mL of streptavidin-Alexa Fluor 488 (Molecular Probes) was added to a 0.10% (w/w) dispersion of the biotinylated particles in a 10 mM sodium phosphate buffer (pH 7.5) that also contained 150 mM NaCl, 1.0% (w/w) bovine serum albumin (BSA, Aldrich), and 0.10% (w/w) Tween-80 (Aldrich). The components were allowed to interact for 4 h, after which the samples were solvent exchanged three times to de-ionized water. The fluorescent spectrum was examined using excitation at 495 nm and monitoring the fluorescent emission between 505 to 600 nm.

The amount of biotin upon the silica particle surface can also be estimated through the completion of any of the above amine-surface concentration determination methods. In this analysis, the signal of the amine-terminated silica particle prior to biotin modification is compared to the signal of the biotin-modified silica particle. The biotin-modified surface

should display smaller amount of signal as compared the amine-modified particle. This is a result of the biotin being covalently linked to the silica surface through the amine functionality and thus reducing the amount of amine groups present upon the silica surface to react to the amine sensitive dyes.

Bio-Conjugation Between Silica-Biotin and Gold-Streptavidin Nanoparticles

A 0.10% (w/w) dispersion of the biotinylated silica nanoparticles was created in a 10 mM phosphate buffer (pH 7.5) with 150 mM NaCl, 1.0% (w/w) BSA, and 0.10% (w/w) Tween-80. Using a micropipette, 200 μL (~3.4 x 10^{12} particles) of the as-received 10-nm streptavidin conjugated gold nanoparticles (Sigma-Aldrich) were added to the dispersion and stirred overnight. This volume represent a 47:1 ratio between the numbers of gold nanoparticles added to the system and estimated amine groups upon the MM surface. The silica-gold conjugated nanoparticles were separated from the excess streptavidin-gold nanoparticles and buffer through a three-time volume exchange to de-ionized water via centrifuging at 3000 rpm for 4 min. Upon solvent exchange to de-ionized water, the conjugated particles were re-suspended via vortexing and stored at 4°C. An aliquot of these particles were reacted with streptavidin-Alexa Fluor 488 and the fluorescence spectra acquired in accordance with the above procedures to determine the degree of biotin groups occupied with the streptavidin-Au label.

Assay Substrate Preparation

A 1 x 1 cm chip of silicon (<111>, Montco Silicon) was cleaned via a five min immersion in a freshly made solution of 3:1 concentrated sulfuric acid (Fisher) and 30%

hydrogen peroxide (Fisher). **(Caution: "Piranha" is a strongly oxidizing solution and should be handled with care and immediately neutralized and disposed of properly following use.)** Immediately upon removing of the Si substrate from the Piranha bath, the substrate was rinsed with copious amounts of de-ionized water. A thin layer of rinse water was retained upon the chip to protecting the pristinely clean surface from adsorption of adventitious materials. This chip, with associated water layer, was then placed at a 10^{o} angle in a humidity-controlled chamber. More specifically, a piece of clean Plexiglas was covered in Parafilm and inclined to a 10^{o} angle in a desiccator vessel.[52-62] This vessel also contained a saturated potassium sulfate (Fisher) aqueous solution that allowed the interior of the sealed chamber to maintain a relative humidity of 53%.[63] To the retained layer of water upon the substrate, 50 μL of a 1.0% particle dispersion, or 100 μL of a 0.10% particle dispersion (i.e., 3.6×10^{11} particles / mL), was added to the retained water layer. The dispersion was allowed to dry upon the substrate within the as described inclined / humidity-controlled system.

Substrate Interrogation and Characterization

The assay platforms were interrogated by AFM with a MultiMode NanoScope IIIa SFM (Digital Instruments) equipped with a recently calibrated 150-μm tube scanner. All topographic images were collected under ambient laboratory conditions in tapping mode with a 125-μm TESP silicon cantilever/tip (Nanosensors). The set-point amplitude of the cantilever was adjusted, and maintained by the feedback circuitry, to 80% of the free oscillation amplitude of the cantilever ($F_N \sim 10^{-9}$ N).

Results and Discussion

Nanoparticle Composition Characterization

The desired attributes of the substrate nanoparticle include a well-defined surface modification chemistry, low affinity for non-specific adsorption, density condusive to centrifugation / re-dispersal washing, and stability in a variety of solvents. In view of these desired characteristics, as well as future detection and sample interrogation techniques, silica was chosen as the substrate particulate material. Silica is naturally resistant to non-specific adsorption due to its extreme hydrophilicity that results from surface silanol groups which form from the hydrolysis of siloxane linkages.[64] Although blocking proteins (i.e., BSA) and surfactants are used within these protocols, non-specific interactions represent a limiting factor in nearly all bio-conjugation assays,[65] thus every precaution was taken within the system design to reduce the potential for false signals. Moreover, silica nanoparticles posses a density of 2 g/mL, and can therefore be separated from an aqueous solution via centrifugation. This ability facilitates the many washing steps that are used in the procedure for reduction of non-specific interactions. Furthermore, the modification chemistry of silicon and silica surfaces has been extensively studied, providing for multiple routes to achieve the desired surface functionality.[66,67] Lastly, silica is stable as a nanoparticle dispersion in a variety of aqueous and organic solvents extending the number of modification and cleaning protocols that can potentially be exploited.

Other potential material candidates examined for use as the substrate nanoparticle include organic polymers, inorganic oxides, and gold. Organic polymeric nanoparticles, while having a well characterized surface chemistry,[65] lack several of the other desired features listed above. Polymeric nanoparticles generally posses a highly hydrophobic

surface, which allows for efficient non-covalent, adsorption based modification, but also favors non-specific adsorption. Furthermore, this hydrophobicity results in low particle repulsion interaction potentials, as predicted through the DLVO theory,[68-70] and at the nanometer size scales of interest, leads to the inability to re-disperse the colloidal particles after sedimentation.[71] Preclusion of efficient centrifugation/solvent exchange washing step increases the probability of non-specific adsorption. Another implication of the low interaction potential is that stable dispersions can only be formed in solutions with lower ionic strengths and/or higher dielectric constants. This solvent constraint is furthered by the instability of organic polymers to standard organic solvents used in several modification protocols (e.g., methylene chloride and toluene).

Inorganic sources of substrate nanoparticulate materials also exist. In these cases, the stability of the colloids is increased due not only to higher interaction potentials, but also increased solvent stability, allowing for more rigorous cleaning procedures to reduce non-specific adsorption and increased modification flexibility. In terms of inorganic oxide nanoparticles (i.e., titanium oxide), the amount of modification chemistry is unfortunately limited. Gold, on the other hand, has a plethora of well-characterized modification chemistries available.[67,72] However, this material was reserved for the labeling nanoparticle. A further constraint of the experimental design existed in that the labeling and substrate nanoparticle were desired to be composed of different materials. This limitation was imposed for two reasons. The first is that distinctive modification/functionalization chemistries can be employed to reduce the chance of non-specific modifications (e.g., thiol exchange between the gold substrate and gold labeling nanoparticles). Secondly, differing

nanoparticle "bulk" materials may enhance the contrast between the labeling and substrate nanoparticle assisting substrate interrogation.

Substrate Nanoparticle Amine-Derivatization and Characterization

Upon identifying silica as the substrate nanoparticle, an optimum modification protocol to functionalize the surface with a primary amine was investigated. First and foremost, an amine-functionalized surface was desired due to the vast availability of bio-conjugate chemistry based upon amine derivatization.[73] As a consequence, an array of aminiation procedures were explored and characterized to ascertain the extent of modification of the silica nanoparticle surface, recognizing that the eventual attachment and activity of the biorecognition moiety depends upon the success of this amine modification step.

Although amine-modified silica particles are available commercially, only a limited range of sizes are offered, thus reducing the potential numbers of analytes that can be investigated within this "bar-code" assay. Un-modified silica nanoparticles, on the other hand, can be controllably synthesized or purchased in many sizes. Therefore, several amine modification methods, including procedures based upon acid catalysis (i.e., acetic acid), base catalysis (i.e., Stöber modification) and solvent reflux were examined to increase the number of distinct substrate nanoparticles available.

The colorimetric and fluorescent tests used for the determination of amine functionalization were chosen due to constraints created by the silica nanoparticles. Although an assortment of UV-Vis colorimetric tests exist for the determination of primary amines, these techniques directly derivatize the surface amine groups, thus resulting in a

surface bound UV-Vis dye. These dye-modified nanoparticle dispersions, when present at concentrations necessary to provide adequate signal, result in a significant amount of Mie scattering from the nanoparticles themselves.[74] This scattering veils the adsorption by the surface bound dye and reduces the utility of the UV-Vis spectrometeric detector.

To circumvent this issue, two different amine sensitive dyes were coupled to differing detection techniques to assess the degree of nanoparticle surface modification. Like many of the traditional amine sensitive dyes, NDA forms a surface-bound fluorophore, having an excitation maximum at ~420 nm and emission maximum at ~480 nm. Furthermore, the NDA modification results in a visible yellowing of the particles, depending on the degree of fluorophore modification (i.e., amine surface concentration). Due to poorly shaped and inadequately reproducible fluorescent spectra, the magnitude of the yellow hue was established by diffuse reflectance spectrometry. The BYK-Gardner spectrometer and integrated software used in this study was developed to quantitate the level of primary colors present within a substrate of a particular hue as defined by the CIE. According to this protocol, the b* values provide the degree of yellowness for a sample. By ranking the b* values as provided by the spectrophotometer for the varied amine-modification protocols, the trend of the degree of modification was determined to be: MM > TR > AA2 > Stöber > AA1 > unmodified Si.

The fluorescamine modification of the primary amine on the functionalized silica nanoparticle surfaces also resulted in a fluorophore bound to the particle surface. The fluorescence spectra in this case, when excited at 380-nm and the resulting emission collected at 90-degrees with respect to the angle of excitation, provided the spectra depicted in Figure 1. As discerned from the spectra, the order of decreasing extent of amine

modification is as follows: MM > AA2 > Stöber > AA1 > TR > unmodified Si. It should be noted that the TR sample within this initial study appeared to be extremely dilute with respect to the vendor specifications and further experiments are needed to confirm this suspected problem. Despite this issue, both dyes indicated that the MM particles possessed the highest amine surface concentration of the dispersions studied, thus the MM nanoparticle was chosen as the substrate particle in the biotin-streptavidin assay.

Proof-of-Concept Biotin-Streptavidin "Bar-Code" Assay

Biotinylation and Characterization

A proof-of-concept experiment to demonstrate the applicability of our AFM topographic bar-code assay was conducted. The biotin-streptavidin biorecognition was chosen for this concept assessment due to the high affinity ($K_a \sim 10^{15}\ M^{-1}$) between these two biomolecules in a variety of aqueous environments.[65,73] The substrate nanoparticle employed was the commercially purchased 300-nm MicroMod particles. In order to biochemically "activate" the amine functionalized silica particle, biotin was conjugated to the particle surface using standard succinimidyl chemistry.[73] Two approaches were taken to determine the level of biotin modification on the particle surface. The first tactic monitored the loss of primary amines, while the second involved direct testing for the presence of biotin.

The degree of biotinylation upon the MM particles was estimated through examining the loss of signal for the amine-directed dyes. Figure 2 depicts the fluorescent spectra of the 0.10% dispersion of the fluorescamine tailored MM and MM-biotin particles. This figure

displays the expected decrease of signal for the MM-biotin, as compared to the MM particles, due to the loss of surface bound amine moieties from biotin modification.

In a similar fashion, the NDA/diffuse reflectance experiment also depicted a decrease in signal upon biotin modification. In this case, a CIE b* value of 6.62 and 4.71 was obtained from the BYK-Gardner spectrometer for the MM and MM-biotin samples respectively. The experiment employing amine reactive fluorescamine as well as the NDA indicate an average signal loss of approximately 26% after biotinylating the particles. This signal change roughly translates to 5.5×10^4 biotin moieties per particle.

The biotinylation of the particle surface was directly confirmed through the specific interaction of the biotin to the Alexa Fluor 488-modified streptavidin. This fluorescent probe can be monitored on the particle surface to not only determine successful biotinylation, but also to probe the activity of the biotin towards streptavidin as well as observe the amount of non-specific interactions with non-biotin modified surfaces. Representative fluorescent spectra of biotin-MM, MM, and unmodified Si particles exposed to Alexa Fluor 488-streptavidin are shown in Figure 3. This figure displays the positive interaction between the biotin particles and the fluorophore, a small amount of non-specific interaction with the MM particle, and almost no interaction with the un-modified Si particles.

Streptavidin-Au (10-nm) bio-conjugated to Biotin-MM (300-nm)

The bioconjugation between the streptavidin modified gold nanoparticles and biotin modified silica nanoparticles was monitored in several ways. The conjugated particles were first analyzed through determining the degree of fluorescent signal reduction of the streptavidin-Alexa Fluor 488 between the conjugated particles and the unexposed biotin-

MM. As shown in Figure 3, the loss of biotin binding sites due to conjugation to streptavidin labeled gold nanoparticles is negligible, indicating little to no Au particle decoration upon the biotin-MM substrate nanoparticles surfaces. However, it should be kept in mind that a successful binding of the streptavidin-Au nanoparticle to the surface of the substrate nanoparticle should not lead to a drastic loss of biotin binding sites. Upon interaction between a Au-bound streptavidin and a biotin functionality, the gold nanoparticle now shadows or sterically hinders the adjacent biotin sites from other Au-bound streptavidin moieties. The Alexa Fluor dye labeled streptavidin is not sterically hindered to the same degree as the dye molecule is significantly smaller than 10-nm particles. Therefore, a significant decrease in available biotin sites after reacting with the avidin-Au nanoparticles, and subsequent decrease in Alexa Fluor dye labeling, is not expected. AFM on the other hand is expected to be able to depict the labeling of the biotin-MM surface with the streptavidin-Au particles.

Imaging the substrate nanoparticle via AFM is possible due to the manner in which they are deposited upon the imaging substrate. The slow evaporation of the particle dispersion on the silicon substrate in the controlled atmosphere environment results in a near closed pack layer of the particles.[52-62] This close pack organization facilitates the examination of the surface morphology of the larger substrate nanoparticles by the AFM.[75] More specifically, the close pack arrangement of nanoparticles requires the AFM electro/mechanical feedback mechanism to respond to decreased amounts of height as the AFM probe is no longer required to traverse the entire height of the particle but only the height between adjacent particles that is at most, roughly half the height of the particle. This

allows the AFM to respond to increasingly fine surface features, thus obtaining an image with greater resolution.

Figure 4A and 4B present an AFM height (A) and phase (B) image of a sample of 300-nm biotin-MM particles prior to exposure to the streptavidin-Au while Figure 4C and 4D display the height (C) and phase (D) image of the 160-nm silica nanoparticles. These combined images illustrate several accomplishments. The evaporation of these dispersions resulted in the intended near close pack organization of the nanoparticle facilitating further examination of the particle characteristics. Cross-sectional analysis of the height images reveals that the particles are, as expected, spherical in shape and are approximately 300 nm and 160 nm for the MM particles the silica particles respectively. The cross-sections also estimate the peak-to-peak surface roughness of an individual particle to be below 1 nm. The phase images (B and D) both display a non-distinctive, aggregated surface morphology for individual nanoparticles. Collectively these images indicate that the silica nanoparticles do not have any surface features on them, and if any surface asperities arise after the assay, it can be ascribed to the labeling gold nanoparticles. Furthermore, the roughness of the silica surface indicate that labeling particles above ~3 nm should be used, as smaller labeling particles would be convoluted within the roughness of the silica particles.

Figure 5 shows a height (A) and phase (B) image of the biotin-MM particles after exposure to the streptavidin-Au labeling nanoparticles. Unlike Figure 4, the topographic (A) and phase (B) images in Figure 5 depict surface asperities upon the substrate nanoparticles. Figure 6 similarly illustrates the height (A) and phase (B) image of a single biotin-MM particle that had been exposed to the streptavidin-Au labeling nanoparticles. As can be seen from the cross-section in Figure 6, the substrate nanoparticles are approximately 300 nm in

diameter. Figure 7 is a magnification of one area of height asperities upon the 300-nm biotin-MM particle. The accompanying cross-section in Figure 7 indicate that the asperities possess a height of ~10 nm. We therefore assign these asperities to the 10-nm streptavidin-Au nanoparticles admitted to the system and bound to the biotin-MM particle surface. These images confirm the low streptavidin-Au particle decoration upon the biotin-MM particles as shown by the earlier fluorescent data (Figure 3).

AFM was also employed to investigate the issue of non-specific adsorption of the streptavidin on the unmodified silica nanoparticles. If unmodified 330-nm silica nanoparticles are exposed to the 10-nm streptavidin-Au dispersion, AFM is unable to find any 10-nm asperities upon the surface and the images are identical to that presented in Figure 4A, marking the lack of non-specific adsorption within this assay. Again, this AFM data corresponds to the fluorescence data (Figure 3), where non-specific adsorption of the streptavidin-Alexa Fluor 488 dye upon the silica particles is limited.

This clear definition of size for both the 300-nm substrate and 10-nm labeling nanoparticles displays not only the success of the biorecognition assay, but that of the created protocol and AFM imaging to visualize a positive "bar-coded" assay. As a means to stress the applicability of this scheme toward a multiplexed immunoassay platform, 160-nm silica nanoparticle, as imaged individually in Figure 4B, were added to the reaction mixture containing the 300-nm biotin-MM particles and the 10-nm streptavidin-Au particles. As these 160-nm nanoparticle do not posses any antigen, they should not specifically bind any of the streptavidin-Au labeling nanoparticles. Figure 8 presents an AFM tapping mode height (A) and phase (B) image illustrating the specific interaction between the 300-nm biotin-MM particles and the 10-nm streptavidin-Au in the presence of the 160-nm silica nanoparticles.

Again, there is no evidence for interaction between the 160-nm Si nanoparticle and the streptavidin moieties. This lack of non-specific adsorption and the sizing capabilities of the AFM, potentially enables the use of the same size labeling nanoparticle to probe different antigens, as long as different sized substrate nanoparticles are employed. Furthermore, if different sized labeling nanoparticles are used thus allowing several combinations of substrate and nanoparticle size, the number of antigens that can be tested for is again increased. This proof-of-concept experiment demonstrates the vast potential of this height based, bar-code protocol for use in a multiplexed immunoassay platform.

Conclusion

With the continued reduction in the size of analytical assay platforms more elegant system designs are necessitated. As shown within, through the employment of self-assembly of nanoparticles that have been modified to be active against a desired analyte, nanometer-sized, bio-specific domains can be easily created and controlled through shrewd choice of nanoparticle characteristics. This system can be further advanced through the addition of multiple sizes of both labeling and substrate nanoparticles providing for an easy route toward multiplexing. In addition, the usage of AFM height read-out avoids the restriction provided by the limited number of distinctive light based tags. Overall the protocol, as developed in this paper, draws upon the advantages of using AFM indicated, "bar-code" / size-based nanoparticle analyte labeling with those of performing immunoassay in solution (i.e., enhanced kinetics as compared to macroscopic substrates).

Future advancements of the platform add an additional level to this high-throughput analysis technique through usage of other AFM modes, such as Kelvin probe or electric force

microscopy. These techniques are not only sensitive to the size of the particle, but also to other chemical characteristics of both the substrate and labeling nanoparticles. This provides a means to differentiate sized based "bar-codes" with identical size, but different compositions. These and other advancements, such as instrumentation automation, are being pursued.

Acknowledgements

A.D.P. expresses appreciation for a Phillips Petroleum Company Research Fellowship and a Mary K. and Velmer A. Fassel Fellowship. This work also was supported by the Office of Basic Energy Research, Chemical Sciences Division, U. S. Department of Energy and by the Microanalytical Instrumentation Center of Iowa State University through the W. M. Keck Laboratory for the Fabrication of Microminiaturized Analytical Instrumentation. The Ames Laboratory is operated for the U.S. Department of Energy by Iowa State University under Contract W-7405-Eng-82.

References

(1) Jones, V. W.; Kenseth, J. R.; Porter, M. D.; Mosher, C. L.; Henderson, E. *Anal. Chem.* **1998**, *70*, 1233-1241.

(2) O'Brien, J. C.; Jones, V. W.; Porter, M. D.; Mosher, C. L.; Henderson, E. *Anal. Chem.* **2000**, *72*, 703-710.

(3) O'Brien, J. C.; Stickney, J. T.; Porter, M. D. *Langmuir* **2000**, *16*, 9559-9567.

(4) O'Brien, J. C.; Stickney, J. T.; Porter, M. D. *J. Am. Chem. Soc.* **2000**, *122*, 5004-5005.

(5) Pris, A. D.; Porter, M. D. *Nano Lett.* **2002**, *2*, 1087-1091.

(6) Lee, H. J.; Goodrich, T. T.; Corn, R. M. *Anal. Chem.* **2001**, *73*, 5525-5531.

(7) Bernard, A.; Michel, B.; Delamarche, E. *Anal. Chem.* **2001**, *73*, 8-12.

(8) Mao, H.; Yang, T.; Cremer, P. S. *Anal. Chem.* **2002**, *74*, 379-385.

(9) Taitt, C. R.; Anderson, G. P.; Lingerfelt, B. M.; Feldstein, M. J.; Ligler, F. S. *Anal. Chem.* **2002**, *74*, 6114-6120.

(10) Kung, L. A.; Kam, L.; Hovis, J. S.; Boxer, S. G. *Langmuir* **2000**, *16*, 6773-6776.

(11) Bernard, A.; Delamarche, E.; Schmid, H.; Michel, B.; Bosshard, H. R.; Biebuyck, H. *Langmuir* **1998**, *14*, 2225-2229.

(12) Bernard, A.; Renault, J. P.; Michel, B.; Bosshard, H. R.; Delamarche, E. *Adv. Mater.* **2000**, *12*, 1067-1070.

(13) Pardo, L.; Wilson, W. C., Jr.; Boland, T. *Langmuir* **2003**, *19*, 1462-1466.

(14) Ivanisevic, A.; Im, J.-H.; Lee, K.-B.; Park, S.-J.; Demers, L. M.; Watson, K. J.; Mirkin, C. A. *J. Am. Chem. Soc.* **2001**, *123*, 12424-12425.

(15) Hyun, J.; Ahn, S. J.; Lee, W. K.; Chilkoti, A.; Zauscher, S. *Nano Lett.* **2002**, *2*, 1203-1207.

(16) Wadu-Mesthrige, K.; Xu, S.; Amro, N. A.; Liu, G.-y. *Langmuir* **1999**, *15*, 8580-8583.

(17) Kenseth, J. R.; Harnisch, J. A.; Jones, V. W.; Porter, M. D. *Langmuir* **2001**, *17*, 4105-4112.

(18) Zhou, D.; Sinniah, K.; Abell, C.; Rayment, T. *Langmuir* **2002**, *18*, 8278-8281.

(19) Köhler, J. M.; Csáki, A.; Reichert, J.; Möller, R.; Straube, W.; Frizsche, W. *Sens. Actuators, B* **2001**, *76*, 166-172.

(20) Bangs, L. B. *Pure Appl. Chem.* **1996**, *68*, 1873-1879.

(21) Ni, J.; Lipert, R. J.; Dawson, G. B.; Porter, M. D. *Anal. Chem.* **1999**, *71*, 4903-4908.

(22) Mock, J. J.; Oldenburg, S. J.; Smith, D. R.; Schultz, D. A.; Schultz, S. *Nano Lett.* **2002**, *2*, 465-469.

(23) Walton, I. D.; Norton, S. M.; Balasingham, A.; He, L.; Oviso, D. F., Jr.; Gupta, D.; Raju, P. A.; Natan, M. J.; Freeman, R. G. *Anal. Chem.* **2002**, *74*, 2240-2247.

(24) Dong, Y.; Shannon, C. *Anal. Chem.* **2000**, *72*, 2371-2376.

(25) Hobara, D.; Imabayashi, S.-i.; Kakiuchi, T. *Nano Lett.* **2002**, *2*, 1021-1025.

(26) Baker, S. E.; Cai, W.; Lasseter, T. L.; Weidkamp, K. P.; Hamers, R. J. *Nano Lett.* **2002**, *2*, 1413-1417.

(27) Battersby, B. J.; Trau, M. *Trends Biotechnol.* **2002**, *20*, 167-173.

(28) Buranda, T.; Huang, J.; Ramarao, G. V.; Ista, L. K.; Larson, R. S.; Ward, T. L.; Sklar, L. A.; Lopez, G. P. *Langmuir* **2003**, *19*, 1654-1663.

(29) Cölfen, H.; Völkel, A.; Eda, S.; Kobold, U.; Kaufmann, J.; Puhlmann, A.; Göltner, C.; Wachernig, H. *Langmuir* **2002**, *18*, 7623-7628.

(30) Cunningham, E.; Campbell, C. J. *Langmuir* **2003**, *19*, 4509-4511.

(31) Grøndahl, L.; Battersby, B. J.; Bryant, D.; Trau, M. *Langmuir* **2000**, *16*, 9709-9715.

(32) Hirsch, L. R.; Jackson, J. B.; Lee, A.; Halas, N. J.; West, J. L. *Anal. Chem.* **2003**, *75*, 2377-2381.

(33) Ki, C. D.; Oh, C.; Oh, S.-G.; Chang, J. Y. *J. Am. Chem. Soc.* **2002**, *124*, 14838-14839.

(34) Koffas, T. S.; Kim, J.; Lawrence, C. C.; Somorjai, G. A. *Langmuir* **2003**, *19*, 3563-3566.

(35) Mucic, R. C.; Storhoff, J. J.; Mirkin, C. A.; Letsinger, R. L. *J. Am. Chem. Soc.* **1998**, *120*, 12674-12675.

(36) Phadtare, S.; Kumar, A.; Vinod, V. P.; Dash, C.; Palaskar, D. V.; Rao, M.; Shukla, P. G.; Sivaram, S.; Sastry, M. *Chem. Mater.* **2003**, *15*, 1944-1949.

(37) Stevens, P. W.; Wang, C. H. J.; Kelso, D. M. *Anal. Chem.* **2003**, *75*, 1141-1146.

(38) Velev, O. D.; Kaler, E. W. *Langmuir* **1999**, *15*, 3693-3698.

(39) Epstein, J. R.; Lee, M.; Walt, D. R. *Anal. Chem.* **2002**, *74*, 1836-1840.

(40) Kenseth, J. R. *Applications of scanning force microscopy and self-assembled monolayers at gold toward the development of immunosensor platforms*; Iowa State University: Ames, 2000, pp 189.

(41) Hilliard, L. R.; Zhao, X.; Tan, W. *Anal. Chim. Acta* **2002**, *470*, 51-56.

(42) Kallury, K. M. R.; Macdonald, P. M.; Thompson, M. *Langmuir* **1994**, *10*, 492-499.

(43) Kallury, K. M. R.; Krull, U. J.; Thompson, M. *Anal. Chem.* **1988**, *60*, 169-172.

(44) Guo, Z.-X.; Yu, J. *J. Mater. Chem.* **2002**, *12*, 468-472.

(45) Walcarius, A.; Etienne, M.; Bessière, J. *Chem. Mater.* **2002**, *14*, 2757-2766.

(46) Pham, T.; Jackson, J. B.; Halas, N. J.; Lee, T. R. *Langmuir* **2002**, *18*, 4915-4920.

(47) Stöber, W.; Fink, A.; Bohn, E. *J. Colloid Interface Sci.* **1968**, *26*, 62-69.

(48) de Montigny, P.; Stobaugh, J. F.; Givens, R. S.; Carlson, R. G.; Srinivasachar, K.; Sternson, L. A.; Higuchi, T. *Anal. Chem.* **1987**, *59*, 1096-1101.

(49) Roach, M. C.; Harmony, M. D. *Anal. Chem.* **1987**, *59*, 411-415.

(50) Gazda, D. B.; Lipert, R. J.; Fritz, J. S.; Porter, M. D.; Rutz, J.; Mudgett, P.; Schultz, J. *Rapid determination of biocide concentrations using colorimetric solid phase extraction (C-SPE): Results from microgravity testing*; SAE International, 2003.

(51) Schroedter, A.; Weller, H. *Angew. Chem. Int. Ed.* **2002**, *41*, 3218-3221.

(52) Perrin, J. *Annales de Chimie-Physics* **1909**, *18*, 1.

(53) Kralchevsky, P. A.; Nagayama, K. *Particles at Fluids Interfaces and Membranes: Attachment of colloid particles and proteins to interfaces and formation of two-dimensional arrays*; Elsevier: Amsterdam, 2001; Vol. 10.

(54) Denkov, N. D.; Velev, O. D.; Kralchevsky, P. A.; Ivanov, I. B.; Yoshimura, H.; Nagayama, K. *Langmuir* **1992**, *8*, 3183-3190.

(55) Lazarov, G. S.; Denkov, N. D.; Velev, O. D.; Kralchevsky, P. A.; Nagayama, K. *J. Chem. Soc. Faraday Trans.* **1994**, *90*, 2077-2083.

(56) Kralchevsky, P. A.; Nagayama, K. *Langmuir* **1994**, *10*, 23-36.

(57) Dimitrov, A. S.; Dushkin, C. D.; Yoshimura, H.; Nagayama, K. *Langmuir* **1994**, *10*, 432-440.

(58) Dimitrov, A. S.; Nagayama, K. *Chem. Phys. Lett.* **1995**, *243*, 462-468.

(59) Dimitrov, A. S.; Nagayama, K. *Langmuir* **1996**, *12*, 1303-1311.

(60) Dushkin, C. D.; Lazarov, G. S.; Kotsev, S. N.; Yoshimura, H.; Nagayama, K. *Colloid Polym. Sci.* **1999**, *277*, 914-930.

(61) Maenosono, S.; Dushkin, C. D.; Yamaguchi, Y.; Nagayama, K.; Tsuji, Y. *Colloid Polym. Sci.* **1999**, *277*, 1152-1161.

(62) Thill, A.; Spalla, O. *Langmuir* **2002**, *18*, 4783-4789.

(63) Wexler, A. *Constant Humidity Solutions*; 76 ed.; Linde, D. R., Ed.; CRC: Boca Rata, 1995, pp **15**-23.

(64) Bangs Laboratories *TechNote #104: Silica Microspheres*; First ed.; Bangs Laboratories, 1997; Vol. 2003.

(65) Diamandis, E. P.; Christopoulos, T. K. *Immunoassay*; Academic Press: San Diego, 1996.

(66) Iler, R. K. *The Chemistry of Silica: Solubility, Polymerization, Colloid and Surface Properties, and Biochemistry*; John Wiley & Sons: New York, 1979.

(67) Ulman, A. *Chem. Rev.* **1996**, *96*, 1533-1554.

(68) Verwey, E. J. W.; Overbeek, J. T. G. *Theory of the Stability of Lyophobic Colloids*; Elsevier Publishing Company, Inc.: Amsterdam, 1948.

(69) Derjaguin, B. V.; Landau, L. *Acta Physicochim. URSS* **1941**, *14*, 633-662.

(70) Israelachvili, J. N. *Intermolecular and Surface Forces*; Second ed.; Academic Press: San Diego, 1992.

(71) Bangs Laboratories *TechNote #204: Adsorption to Microspheres*; Bangs Laboratories, 1999; Vol. 2003.

(72) Ulman, A. *An Introduction to Ultrathin Organic Films: From Langmuir-Blodgett to Self-Assembly*; Academic Press, Inc.: Boston, 1991.

(73) Hermanson, G. T. *Bioconjugate Techniques*; Academic Press: San Diego, 1996.

(74) Ingle, J. D., Jr.; Crouch, S. R. *Spectrochemical Analysis*; Prentice Hall: Englewood Cliffs, 1988.

(75) Maeda, H.; Maeda, Y. *Nano Lett.* **2002**, *2*, 1073-1077.

Figure Captions

Figure 1: Fluorescent spectra of 1.0% dispersions of fluorescamine dyed amine-modified silica nanoparticles

Figure 2: Fluorescent spectra of 0.1% dispersion of the fluorescamine tailored MM and biotin-MM nanoparticles

Figure 3: Fluorescent spectra of 0.1% dispersion of modified silica nanoparticles exposed to streptavidin-Au and/or streptavidin-Alexa Fluor 488

Figure 4: Tapping mode height (A) and phase (B) images of 300-nm biotin-MM nanoparticles; Tapping mode height (C) and phase (D) images of 160-nm silica nanoparticles

Figure 5: Tapping mode height (A) and phase (B) images of 300-nm biotin-MM nanoparticles labeled with 10-nm streptavidin-gold nanoparticles

Figure 6: Tapping mode height (A) and phase (B) images of a single 300-nm biotin-MM nanoparticle labeled with 10-nm streptavidin-gold nanoparticles and associated cross-section of 300-nm nanoparticle

Figure 7: Tapping mode height image of 10-nm streptavidin-gold nanoparticles upon a 300-nm biotin-MM particle, magnified from Figure 6, and associated cross-section of the 10-nm nanoparticles

Figure 8: Tapping mode height (A) and phase (B) images of 300-nm biotin-MM nanoparticles specifically labeled with 10-nm streptavidin-gold nanoparticles in the presence of 160-nm silica nanoparticles

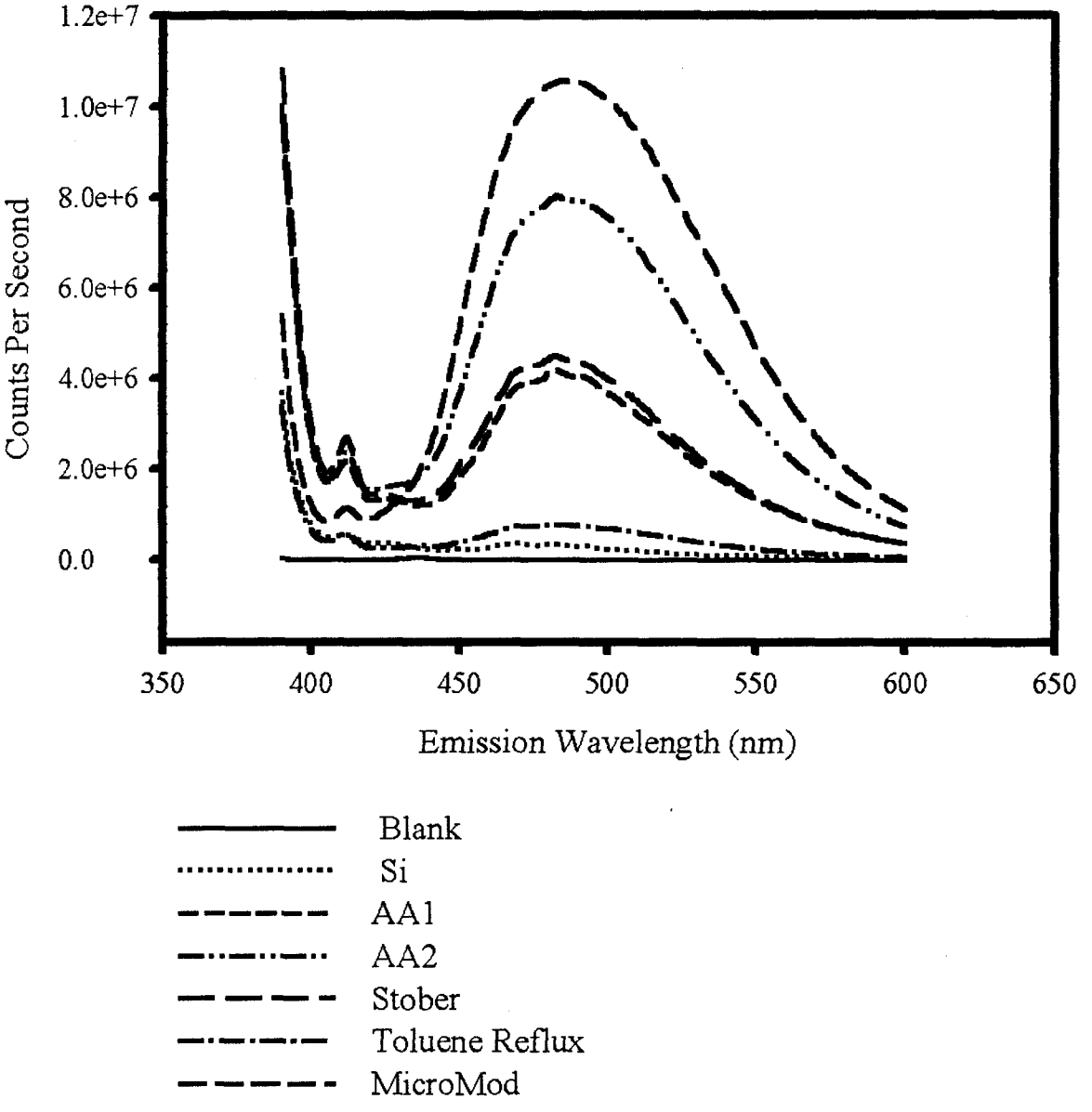
1.2e+7
1.0e+7
8.0e+6
6.0e+6
4.0e+6
2.0e+6
0.0
Counts Per Second
350
400
450
500
550
600
650
Emission Wavelength (nm)
Blank
Si
AA1
AA2
Stober
Toluene Reflux
MicroMod

Figure 1

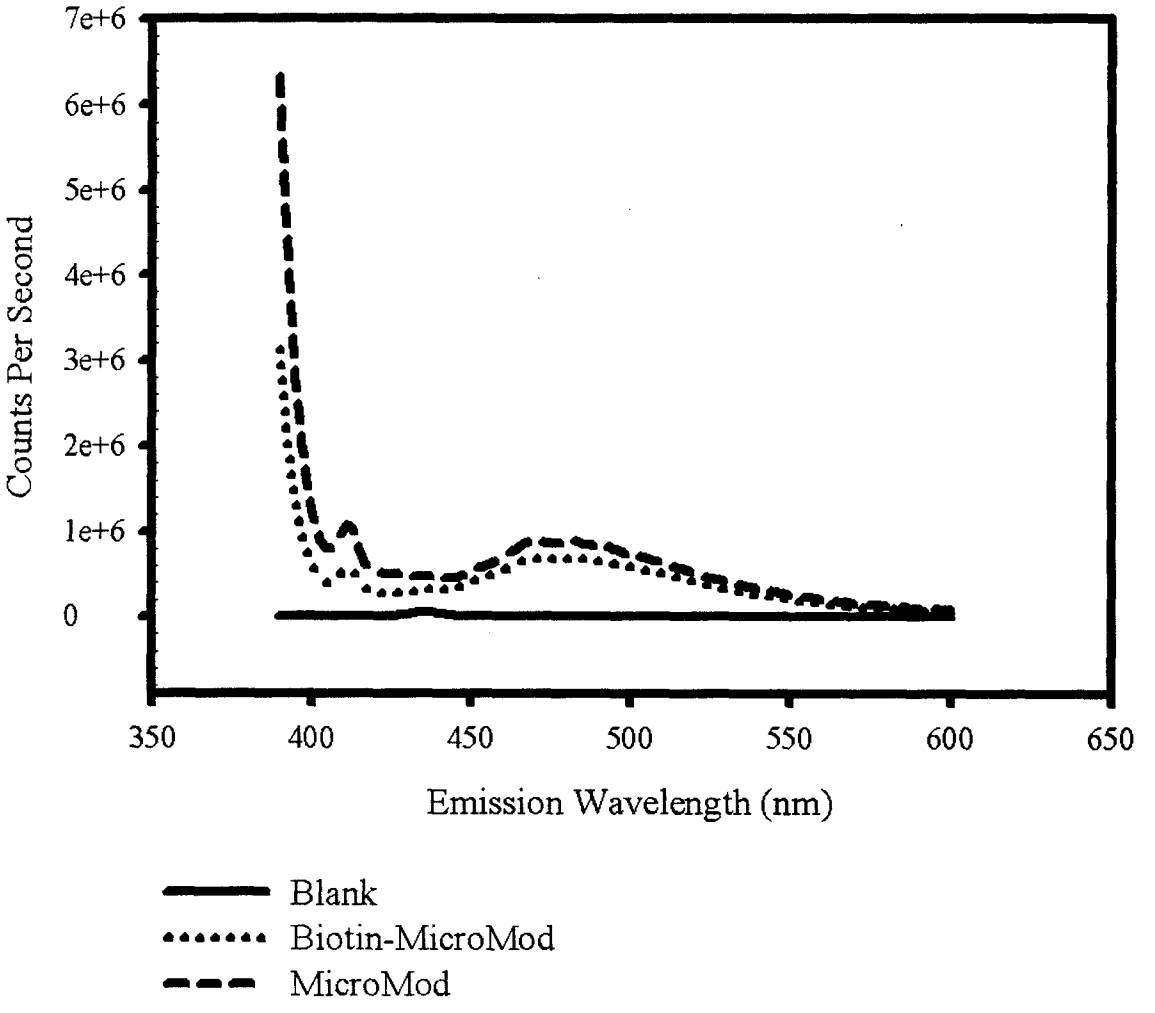
7e+6
6e+6
5e+6
4e+6
3e+6
2e+6
1e+6
0
Counts Per Second
350
400
450
500
550
600
650
Emission Wavelength (nm)
Blank
Biotin-MicroMod
MicroMod

Figure 2

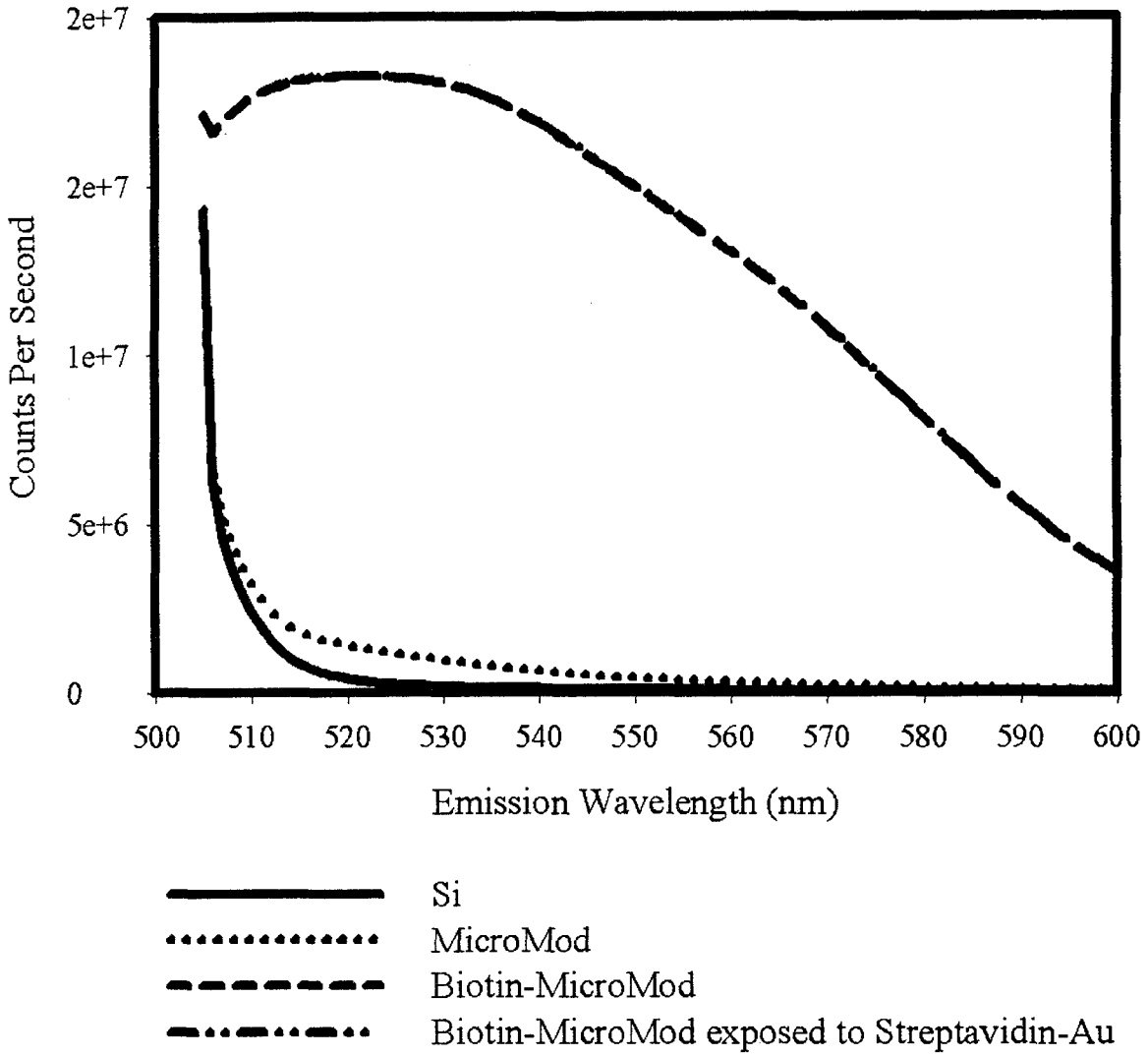
2e+7
2e+7
1e+7
5e+6
0
Counts Per Second
500
510
520
530
540
550
560
570
580
590
600
Emission Wavelength (nm)
Si
MicroMod
Biotin-MicroMod
Biotin-MicroMod exposed to Streptavidin-Au

Figure 3

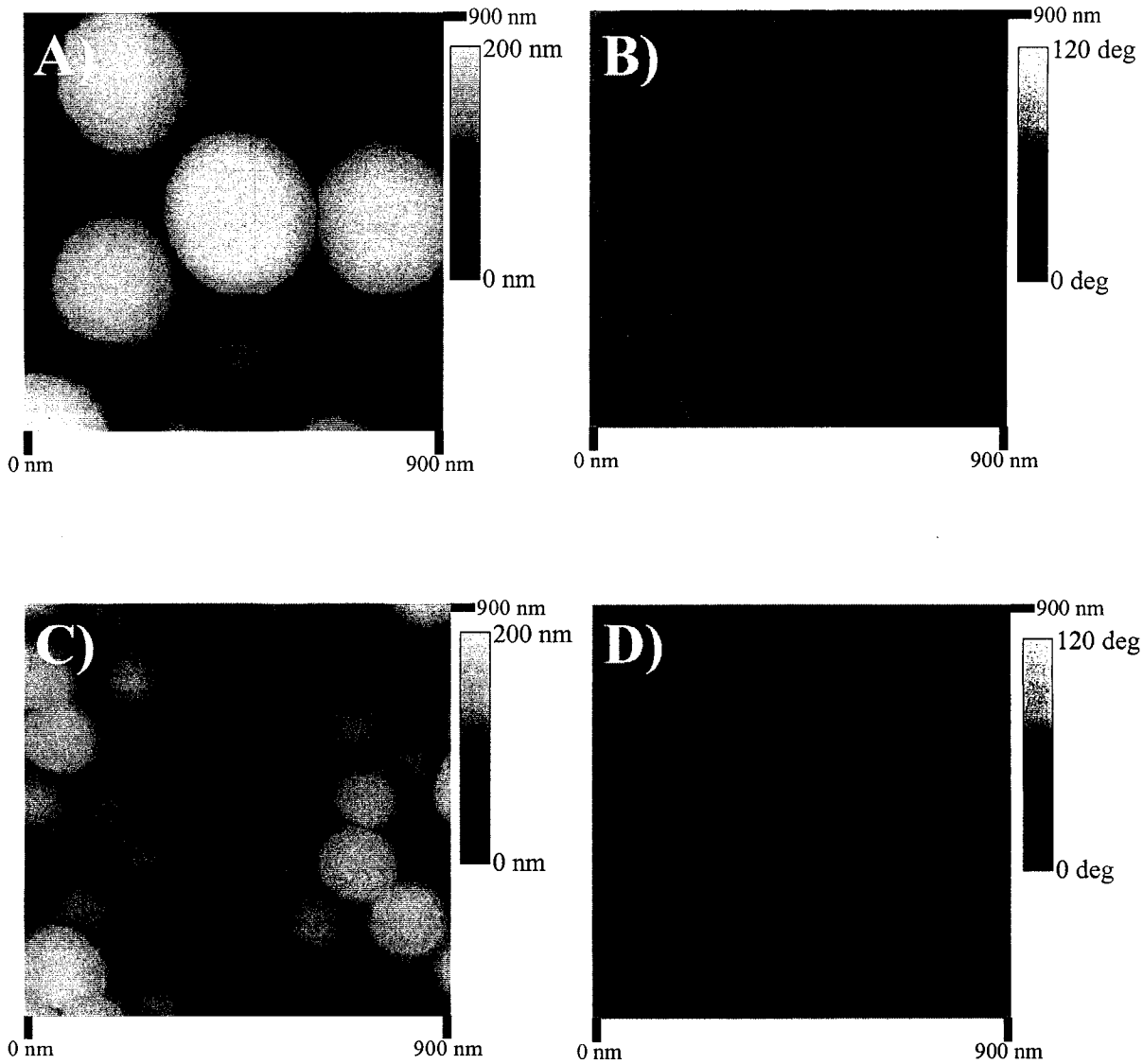
A)
900 nm
200 nm
0 nm
0 nm
900 nm
B)
900 nm
120 deg
0 deg
0 nm
900 nm
C)
900 nm
200 nm
0 nm
0 nm
900 nm
D)
900 nm
120 deg
0 deg
0 nm
900 nm

Figure 4

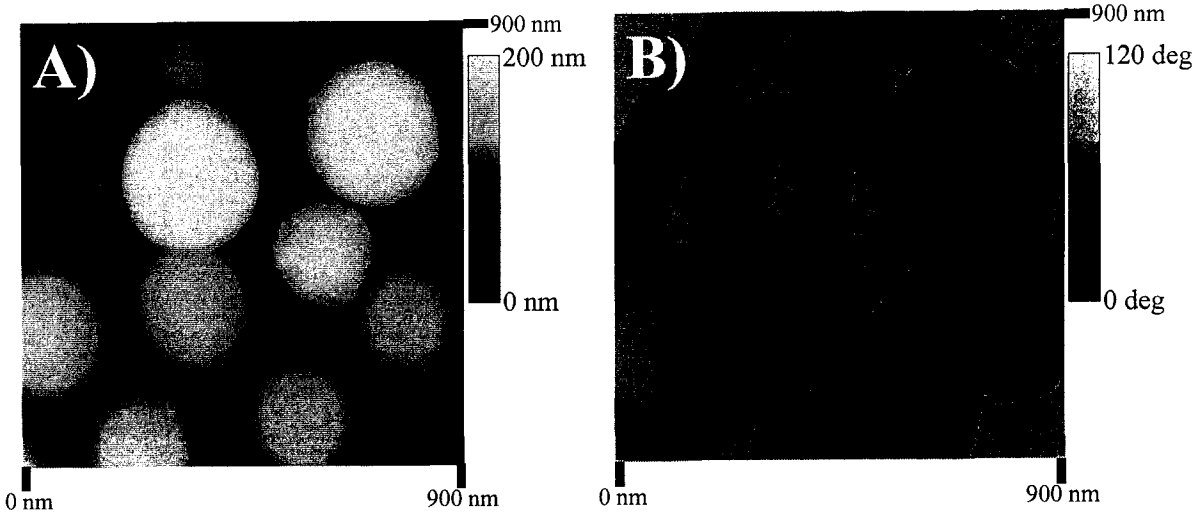

Figure 5

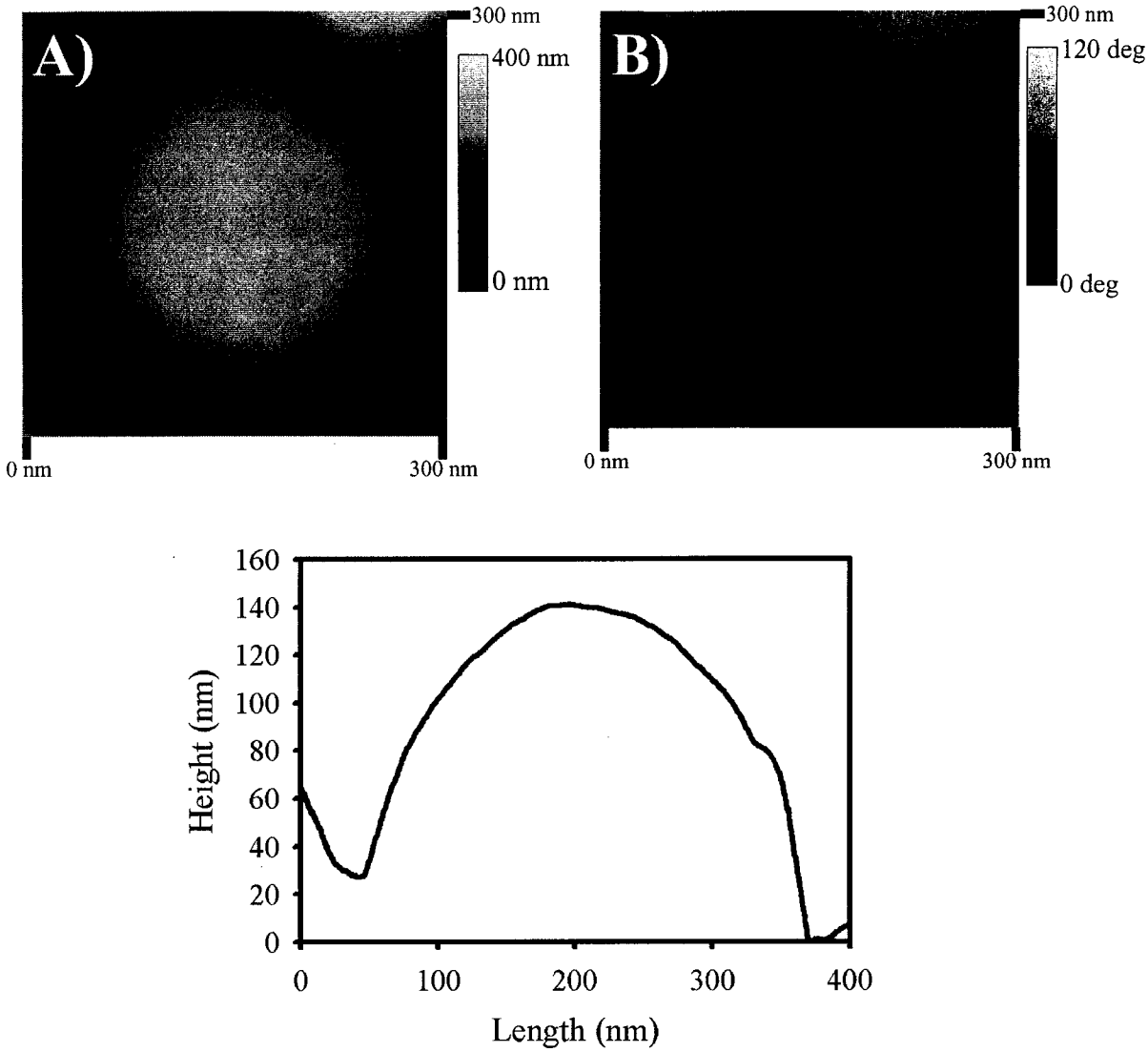
A)
300 nm
400 nm
0 nm
0 nm
300 nm
B)
300 nm
120 deg
0 deg
0 nm
300 nm
Height (nm)
160
140
120
100
80
60
40
20
0
0
100
200
300
400
Length (nm)

Figure 6

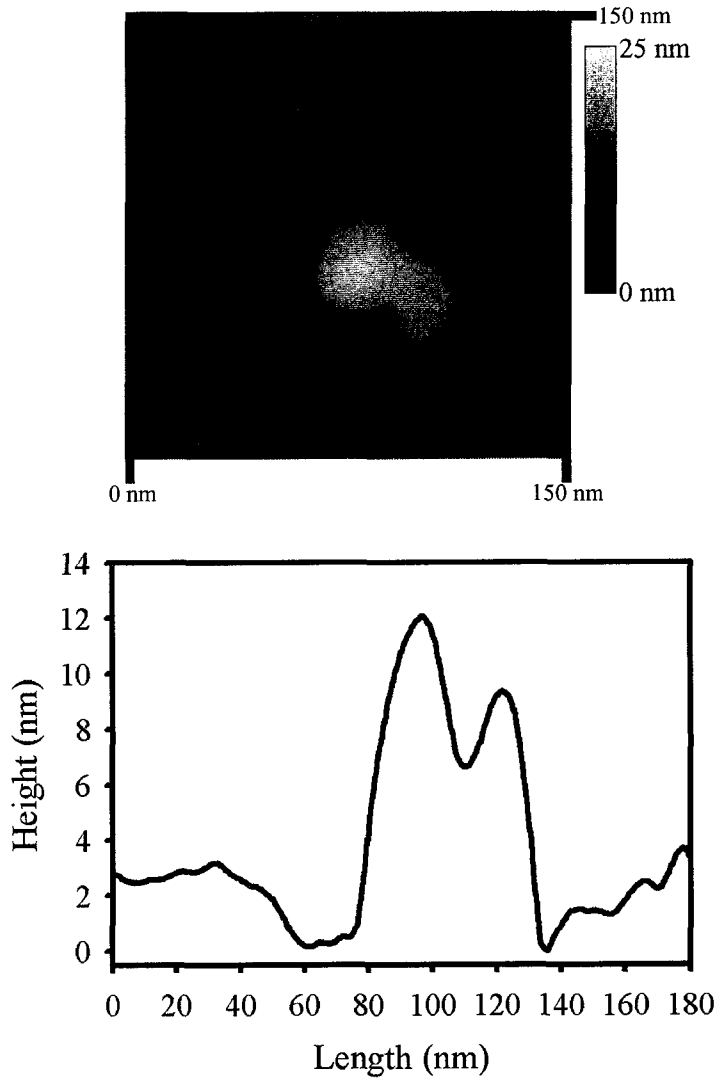
150 nm
25 nm
0 nm
0 nm
150 nm
Height (nm)
14
12
10
8
6
4
2
0
0 20 40 60 80 100 120 140 160 180
Length (nm)

Figure 7

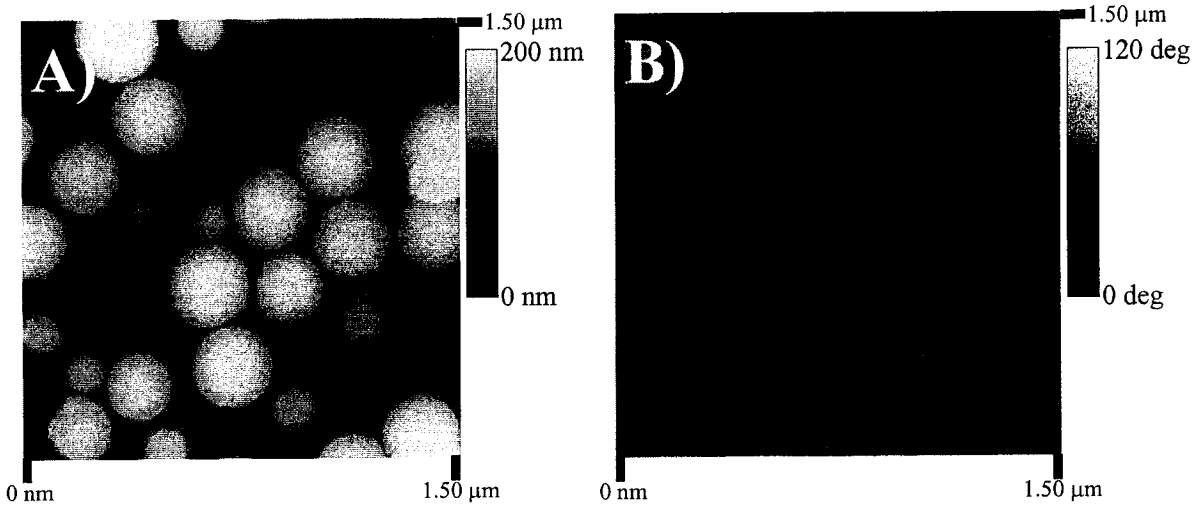

Figure 8

GENERAL CONCLUSIONS AND FUTURE PROSPECTUS

The underlying theme throughout this thesis has been an investigation into exploiting the self-assembly of nanoparticles for the creation of analytically useful architectures and platforms. Chapter 1 depicts one such effort through the deposition of polymeric nanoparticles on a pattern consisting of chemically distinct monolayers. A set of rules associated with controlling the patterning of polymeric nanoparticles on a surface were established by observing the interaction between differing combinations of monolayer surface chemistry, nanoparticle characteristics (i.e., covalently attached functional groups), and dispersing solvent composition (i.e., surfactant concentration). These rules were then employed to create miniaturized architectures through solution deposition.

This theme is continued in Chapter 2, where polymeric nanoparticles are again allowed to self-assembly upon a substrate and create structures, but now with additional control over the third structural dimension, height. The layer-by-layer process and associated scheme presented in this Chapter yield an elegant pathway for precisely defining the height of the structures by controlling the number of particle layers, size of the nanoparticles, and by post-thermal processing. In addition, the choice of photomask design bestows the procedure a facile means to control the lateral dimensions of the produced structure. Furthermore, this unique process is shown to be capable of isolating vast numbers of chemical species, with picoliter volumes, in a massively dense format. These capabilities provide for the prospect of employing this platform in a high-throughput, combinatorial chemistry approach.

Chapter 3 then explores the application of this three-dimensional structure, which was created and characterized in Chapter 2, as an analytical platform. Through coupling this

massively dense array of picoliter volume wells (e.g., 650,000 wells / cm^2) to standard immunodiagnostic assay protocols; functional, fluorescence-based, immunoassays were performed. Other interferences (i.e., non-specific adsorption and label cross-talk) were controlled on this platform by following existing protocols for macroscopic titer plate immunoassays.

Chapter 4 extends the theme of nanoparticle self-assembly towards high-throughput screening (HTS) by depicting a proof-of-concept experiment. In this case, the surface of nanoparticles, specifically silica and gold, are chemically designed to self-assemble in a predetermined pattern in response to the presence of an antigen. This "bar-code" pattern is then analyzed with the atomic force microscope (AFM) not only detecting the presence of an antigen, but also identifying the antigen. This concept is demonstrated by utilizing established specificity of the biotin-streptavidin binding.

The most exciting prospects of these presented methods rest in coupling them to already developed assay protocols to expand their utility. The microwells created and characterized in Chapter 2 provide a unique opportunity to isolate, on the micrometer size-scale, compounds of interest. With many compounds now present within the scan size of an AFM, unique opportunities are presented to study several phenomena. AFM is capable of contrasting several minutely different physical and chemical properties that are represented in the same scan area. However, if this contrasting capability is to be applied to samples present in different scan areas much care and consideration must be taken to properly calibrate the system to ensure accuracy. This situation can be avoided by placing all of the compounds to be compared within the same scan region. The microwell array affords this capability by allowing for the specific isolation of differing compound in an organized,

dense, and miniaturized fashion. Systems that can be analyzed with this coupling of technologies include the properties of monolayers (e.g., surface free energy and surface pK_a) as well as traditional height based immunoassays.

In this second application, each well can be specifically activated, through bio-conjugate techniques, against a pre-determined analyte. If a change in height is detected by AFM between the well wall and modified floor after exposure to a sample, the analyte of interest is therefore present in the sample. Each well on the miniaturized platform can essentially act against a differing antigen and thus probe ~650,000 antigen/cm^2.

Chapter 4 presents the concept with perhaps the greatest potential for future advancement. The number of analytes in a sample that can be tested for with the multiplexed design of nanoparticle binding on nanoparticle coatings is staggering. This number can be further increased if used in conjunction with the microwells. When coupled, the location of the microwell, the size of the substrate nanoparticle, and the size of the labeling nanoparticle are all essential to identifying the analyte. This capability results in the opportunity to use the same "bar-code" for different analytes, as long as they reside in different microwells. Again, this increases the number of analytes that can be analyzed with this miniaturized immunodiagnostic platform in a high-throughput fashion.

There are, of course, several fundamental challenges associated with these unions, the first and foremost being the ability to specifically address an individual well, and then locate and interrogate that same well with the AFM. Currently, the microwells are addressed with an optical microscopy / micromanipulator apparatus and the difficulty arises when attempting to arrange the substrate beneath the AFM probe such that a specific well is interrogated. This inherent obstacle can be overcome by addressing the well after it is positioned beneath the

AFM probe. A more realistic means (due to the engineering / design of the AFM) is to fashion a unique pattern upon the surface that can be visualized by both the optical microscope and the AFM. This unique pattern would assist in properly identifying the location of an addressed well.

Other challenges include arresting the rate of evaporation of the liquids from the addressed wells. Currently, a Peltier cooler is exploited to decrease the temperature of the substrate; however, this approach is also problematic. That is, the kinetics of several surface reactions are severely attenuated at the decreased temperatures used, increasing the time required for equilibration. One probably strategy to reduce the volatility of the compounds and allow them to be maintained as liquids in the well entails raising the partial pressure of the liquid in the environment surrounding the well. In this scenario, a closed system must be fabricated (i.e., a lid for each well). The hurdle associated with this circumstance resides in accessing to the wells for addressing. Practical close system designs must either include the use of micropipettes / micromanipulators, or some means to address wells via microfluidic channels. These and other impediments are currently being pursued in our laboratory.